Précession de l'aimantation en géométrie confinée: aspects physiques et numériques

Gonçalo Albuquerque

N° D'ORDRE : 6948

UNIVERSITÉ PARIS XI
UFR SCIENTIFIQUE D'ORSAY

THÈSE

présentée pour obtenir

le GRADE de DOCTEUR EN SCIENCES
DE L'UNIVERSITÉ PARIS XI ORSAY

par

Gonçalo Marcos Baião de Albuquerque

Sujet

PRÉCESSION DE L'AIMANTATION EN GÉOMÉTRIE CONFINÉE : ASPECTS PHYSIQUES ET NUMÉRIQUES

Soutenue le 15 juillet 2002 devant la Commission d'examen

Président :	M.	Claude Chappert
Rapporteurs :	MM.	Russell Cowburn
		Thomas Schrefl
Directeur de thèse :	M.	Jacques Miltat
Examinateurs :	MM.	François Alouges
		Jean-Christophe Toussaint
Invité :	M.	André Thiaville

Magnetisation Precession in Confined Geometry: Physical and Numerical Aspects

by

Gonçalo Marcos Baião de Albuquerque

A dissertation submitted in partial fulfillment
of the requirements for the degree of

Docteur en Sciences

Université Paris XI Orsay
July 2002

Retrato de uma princesa desconhecida

Para que ela tivesse um pescoço tão fino
Para que os seus pulsos tivessem um quebrar de caule
Para que os seus olhos fossem tão frontais e limpos
Para que a sua espinha fosse tão direita
E ela usasse a cabeça tão erguida
Com uma tão simples claridade sobre a testa
Foram necessárias sucessivas gerações de escravos
De corpo dobrado e grossas mãos pacientes
Servindo sucessivas gerações de príncipes
Ainda um pouco toscos e grosseiros
Ávidos cruéis e fraudulentos

Foi um imenso desperdiçar de gente
Para que ela fosse aquela perfeição
Solitária exilada sem destino.

Sophia de Mello Breyner Andresen

Publication List

- "*Quasi-coherent rotation switching mode in meso-scale patterned structures*", J. Miltat, G. Albuquerque, and A. Thiaville, in *Frontiers in Magnetism Proceedings*, K. V. Rao, A. M. Grishin, and T. H. Johansen, eds., (The Royal Institute of Sweden, Stockholm, 1999), ISBN 91-7170-438-8.

- "*Coherent spin structures dynamics: Numerics and application to high density magnetic random access memories (MRAM's)*", G. Albuquerque, J. Miltat, and A. Thiaville, in *16th IMACS World Congress*, M. Deville and R. Owens, eds., (IMACS, New York, 2000), ISBN 3-9522075-1-9.

- "*An Introduction to Micromagnetics in the Dynamical Regime*", J. Miltat, G. Albuquerque, and A. Thiaville, in "*Spin Dynamics in Confined Magnetic Structures*", B. Hillebrands and K. Ounadjela, eds., (Springer-Verlag, Heidelberg, 2001).

- "*Micromagnetics: Dynamical Aspects*", J. Miltat, G. Albuquerque, and A. Thiaville, in *Magnetism and Synchroton Radiation*, E. Beaurepaire, F. Scheurer, G. Krill, and J. P. Kappler, eds., (Springer-Verlag, Berlin, 2001).

- "*Self-consistency based control scheme for magnetization dynamics*", G. Albuquerque, J. Miltat, and A. Thiaville, J. Appl. Phys., **89**, 6719–6721 (2001).

- "*Spin transfer into an inhomogeneous magnetization distribution*", J. Miltat, G. Albuquerque, A. Thiaville, and C. Vouille, J. Appl. Phys., **89**, 6982–6984 (2001).

Contents

Introduction

Magnetism owes much to the conceptual breakthrough offered by quantum mechanics (for a modern approach see [1]): The notion of spin and spin dynamics. In the classical limit, the 1935 paper of Landau and Lifshitz [2] constitutes an unavoidable reference. Gilbert [3] produced a complementary view to spin motion based on the interplay between conservative "gyrotropic" precession around the spins' effective field and a dissipative (viscous) damping associated with this movement. This theoretical approach is still widely used today [4]. In the continuation of these pioneering theoretical works, Kikuchi [5] was the first to address the question of the minimum switching time when magnetisation motion is essentially governed by precession.

If the development of thin (and very thin) films provided a propitious ground for the development of the theory of domain wall dynamics (see, for instance, [6]), the magnetic systems under study could still be considered as essentially unbounded and the relevant time scales associated with magnetisation motion were clearly far greater than the nanosecond. Only recently have experimental techniques allowed to probe magnetisation dynamics below the nanosecond [7]. As an immediate consequence, research efforts have concentrated on the achievement of magnetisation switching in thin films using extremely short field pulses [8, 9], with the purpose of fully exploiting the precessional nature of magnetisation motion. The pace was clearly set: Understand magnetisation dynamics on times scales approaching the characteristic precessional frequencies of the system under study and on spatial scales which are those of micromagnetics [10]. Such are also the requirements of future magnetic recording and magnetoelectronic devices [11, 12, 13].

In this respect, numerical micromagnetic simulations have lead the way (see [4]) and have provided for a considerable insight into the mechanisms of magnetisation switching in elements of reduced dimensions. Validating numerical predictions leads us to the limits of available experimental techniques and a huge effort is being dedicated to their development,

with the objective of allowing for a time-resolved monitoring of magnetisation motion in submicron-sized platelets [14, 15, 16, 17, 18].

This is the context of the present work: The understanding, from a numerical point of view, of the magnetisation mechanisms leading to a controlled and coherent fast precessional switching in magnetic elements of ever decreasing lateral dimensions.

Thesis' outline

Chapter 1 starts with a general derivation of the gyromagnetic equation of motion from quantum-mechanical principles. There follows a derivation of Brown's and the Landau-Lifshitz-Gilbert (LLG) equations from a general variational approach, ending with the proposal of a dimensionless system of units and the ensuing rewriting, in an invariant form, of the basic equations of micromagnetism. *Chapter 2* deals with precessional dynamics in the macrospin (or single spin) approximation in a thin film platelet. A thorough analysis of the switching phase diagram is given, a particular emphasis being laid on the determination of ballistic trajectories, corresponding to ringing-free switching events in a minimal time. Complexities arising from considering the magnetisation spatial degrees of freedom are introduced in *Chapter 3*. There, besides establishing the remanent energy state hierarchy in 500×250 nm^2 platelets as a function of thickness, transverse oscillations numerical experiments are performed (no magnetisation switching is yet involved). They aim at quantitatively establish the degree of non-macrospin like behaviour in inhomogeneous magnetisation distributions. This quantitative measure, based on the recalculation of the phenomenological damping parameter, is further discussed in the Appendix A. *Chapter 4* constitutes the backbone of the present work. There, numerical micromagnetic results pertaining to the precessional magnetisation switching of submicron-sized platelets are given. Emphasis is now put on the achievement of a quasi-coherent magnetisation motion, possibly mimicking the macrospin ballistic trajectories, and allowing for minimal post-switching oscillations below the nanosecond time scale. The detailed characteristics of optimised switching events are presented. Finalising the main text, *Chapter 5* proposes a brief description and analysis of the impact of real world parameters in the magnetisation switching mechanisms presented in Chapter 4. We divide our attention between the effects of edge roughness and the influence of stray field coupling originating from an Artificial AntiFerromagnetic (AAF) stack on a soft (free) magnetic layer. In addition, the

effects of structural disorder in both the AAF stack and the free layer are considered. The *Appendix A* proposes a self-contained description of the numerical procedures employed in this work. It focuses on the innovative contributions developed during this thesis, namely the damping parameter recalculation as a means of quantifying time domain errors and the development of an optimised semi-implicit Crank-Nicolson numerical integration scheme for the LLG equation. Finally, *Appendix B* discusses some issues arising from the detailed solution of the μMAG Standard Problem No. 4, in particular the effects of spatial discretisation on the dynamics of small scale magnetisation distributions.

Chapter 1

Equations of Magnetisation Motion

This introductory chapter aims at presenting the ensemble of the equations needed in the following discussions, laying emphasis on the intimate links between quantum-mechanical concepts and the parameters employed in applied magnetism. The apparently irreconcilable views of first principles theoretical developments and the Lagrangian formulation of the equations of magnetisation motion will be discussed, highlighting both their strengths and shortcomings. The analysis starts by considering an *ab initio* formulation in deriving the gyromagnetic equation for a single spin, proceeding next to tackle the questions raised by the introduction of spatial degrees of freedom, which leads us to the development of a unified, and self-contained, three-dimensional variational approach to the derivation of the general form of the equations of motion. It immediately allows for the deduction of the well-known Brown's equations, including en passant general energy surface contributions and the underlying boundary conditions arising from volume exchange interactions. The questions raised by addressing the kinematics of magnetisation motion are analysed in some detail, in particular when considering a fully Lagrangian derivation of the equations of magnetisation motion. Damping is next introduced in a strictly phenomenological way, leading to the well-known Landau-Lifshitz-Gilbert equation of magnetisation motion. In closing this chapter, a tentative working solution to the everlasting question of units in magnetism (and inevitably in micromagnetism) is outlined, leading to the proposal of a set of reduced (dimensionless) units. A common form of the basic equations of motion in both the CGS and SI systems is thus arrived at.

1.1 Quantum-Mechanical Concepts

In the same manner as a magnetic moment $\mathbf{M}^{(a)}$ is associated with the electron's orbital angular momentum $\mathbf{L}$, an intrinsic magnetic moment is assumed to be associated with the electron's spin $\mathbf{S}$ [1]. This relation is expressed as

$$\mathbf{M} = \gamma \mathbf{S} \quad , \tag{1.1}$$

where γ, the gyromagnetic ratio, is given by

$$\gamma = \frac{g\mu_{\mathrm{B}}}{\hbar} < 0 \quad . \tag{1.2}$$

In Eq. (1.2), g is the so-called gyromagnetic splitting factor, or Landé factor, and $\hbar$ is Plank's constant. Owing to the definitions adopted above the Bohr magneton $\mu_{\mathrm{B}} = q_e\hbar/2m_e$ (with q_e and m_e the charge and mass of the electron, respectively) is logically negative.

In the most general case, the electron's total angular momentum $\mathbf{J} = \mathbf{L}+\mathbf{S}$ must be used when determining $\mathbf{M}$, and Eq. (1.1) should be changed accordingly. From the quantum-mechanical theory of angular momentum one may then obtain a general expression for the Landé factor, namely

$$g = \frac{3}{2} + \frac{\mathsf{S}(\mathsf{S}+1) - \mathsf{L}(\mathsf{L}+1)}{2\mathsf{J}(\mathsf{J}+1)} \quad . \tag{1.3}$$

Disregarding all orbital contributions to the total angular momentum ($\mathsf{L} = 0,\ \mathsf{J} = \mathsf{S}$) yields $g = 2$, while for a spinless particle ($\mathsf{S} = 0,\ \mathsf{J} = \mathsf{L}$) the Landé factor is equal to 1. In the most common ferromagnetic metals, orbital contributions to the magnetic moment are found to be actually rather small. Recent X-ray Magnetic Circular Dichroism (XMCD) data have provided for quantitative values of the orbital to spin magnetic moment ratios [19]. For both bcc Fe and hcp Co these values do not exceed 10%. Here, Eq. (1.1), with $g = 2$, will therefore be assumed to be the basic relation connecting magnetic moment to angular momentum.

The link between quantum and classical mechanics is provided by the time evolution of the mean value of quantum-mechanical operators associated with measurable physical quantities. Such operators are called observables. Given an arbitrary observable $\mathbf{A}$, its

[(a)] A quantum-mechanical vector operator shall be represented as $\mathbf{A}$ in contrast with the corresponding classical quantity $\mathbf{A}$ (respectively A and A for scalars).

mean value $\langle \mathbf{A} \rangle$ evolves in time according to the Schrödinger equation

$$\frac{d}{dt}\langle \mathbf{A} \rangle = \frac{1}{\imath\hbar}\langle [\mathbf{A}, \mathsf{H}] \rangle + \left\langle \frac{\partial \mathbf{A}}{\partial t} \right\rangle \quad , \tag{1.4}$$

where H is the Hamiltonian operator.

It is now possible to determine the time evolution of the mean value of a magnetic moment placed in an arbitrary external magnetic field. Since $\mathbf{M}$ does not explicitly depends on time one may write

$$\imath\hbar \frac{d}{dt}\langle \mathbf{M} \rangle = \langle [\mathbf{M}, \mathsf{H}] \rangle \quad , \tag{1.5}$$

with $\mathsf{H} = -\mathbf{M} \cdot \mathbf{B}$. It is worth noting that there is no kinetic term in the Hamiltonian associated with a magnetic moment. This simply reflects the fact that spin, viewed as an angular momentum, has no classical analogue, i.e. it is not derived from any position variable. The implications of this fundamental quantum-mechanical property will be more amply discussed in Sect. 1.2.2.

Explicitly expanding the x component of the commutator above, and taking into account the fact that the magnetic field $\mathbf{B}$ is a classical quantity, yields

$$\begin{aligned} [\mathsf{M}_x,\ \mathsf{H}] &= -\gamma^2 \left[\mathsf{S}_x,\ \mathsf{S}_x B_x + \mathsf{S}_y B_y + \mathsf{S}_z B_z\right] \\ &= -\gamma^2 B_y \left[\mathsf{S}_x,\ \mathsf{S}_y\right] - \gamma^2 B_z \left[\mathsf{S}_x,\ \mathsf{S}_z\right] \quad . \end{aligned} \tag{1.6}$$

Since $\mathbf{S}$ is an angular momentum operator it obeys the usual commutation rules

$$\begin{aligned} [\mathsf{S}_x,\ \mathsf{S}_y] &= \imath\hbar \mathsf{S}_z \quad , \\ [\mathsf{S}_y,\ \mathsf{S}_z] &= \imath\hbar \mathsf{S}_x \quad , \\ [\mathsf{S}_z,\ \mathsf{S}_x] &= \imath\hbar \mathsf{S}_y \quad . \end{aligned} \tag{1.7}$$

By substituting Eq. (1.7) into Eq. (1.6) one obtains

$$[\mathsf{M}_x,\ \mathsf{H}] = \imath\hbar\gamma^2 \left(B_z \mathsf{S}_y - B_y \mathsf{S}_z\right) \quad . \tag{1.8}$$

Cyclic permutation of the equation above allows to write

$$\frac{d}{dt}\langle \mathbf{M} \rangle = \gamma \left(\langle \mathbf{M} \rangle \times \mathbf{B}\right) \quad . \tag{1.9}$$

The classical equivalent of Eq. (1.9) can be immediately written in terms of the magnetisation $\mathbf{M}$, simply defined as being the magnetic moment. Using the SI system of units, with $\mathbf{B} = \mu_0 \mathbf{H}$, yields

$$\frac{d\mathbf{M}}{dt} = \mu_0 \gamma \left(\mathbf{M} \times \mathbf{H}\right) \quad . \tag{1.10}$$

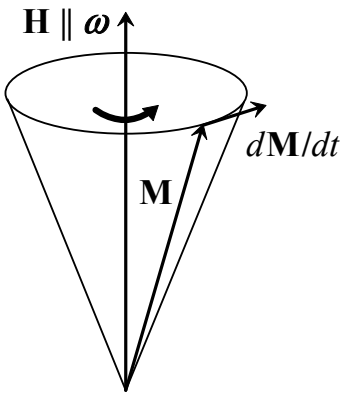

Figure 1.1: Precessional motion of magnetisation.

It proves altogether more convenient to define a gyromagnetic constant γ_0 as

$$\gamma_0 = -\mu_0\gamma > 0 \quad , \tag{1.11}$$

and write the equation governing magnetisation motion as

$$\frac{d\mathbf{M}}{dt} = -\gamma_0 \left(\mathbf{M} \times \mathbf{H}\right) \quad . \tag{1.12}$$

Assuming the applied magnetic field to be time independent, multiplying Eq. (1.12) successively by $\mathbf{M}$ and $\mathbf{H}$ leads to

$$\frac{d}{dt}\left(\mathbf{M}^2\right) = 0 \quad \text{and} \quad \frac{d}{dt}\left(\mathbf{M} \cdot \mathbf{H}\right) = 0 \quad . \tag{1.13}$$

During motion both the modulus of the magnetisation vector and the angle between the magnetic field and the magnetisation remain constant. Consequently the energy $-\mu_0 \left(\mathbf{M} \cdot \mathbf{H}\right)$ remains unchanged. More generally, for a time dependent magnetic field, Eq. (1.12) can always be written as

$$\frac{d\mathbf{M}}{dt} = -\left(\mathbf{M} \times \boldsymbol{\omega}\right) \quad , \tag{1.14}$$

with

$$\boldsymbol{\omega} = \gamma_0 \mathbf{H} \quad , \tag{1.15}$$

the angular velocity vector. Equation (1.14) simply describes an instantaneous precessional motion of the magnetisation vector around $\boldsymbol{\omega}$, as sketched in Fig. 1.1, i.e. $d\mathbf{M}/dt$ lies continuously in a plane perpendicular to $\boldsymbol{\omega}$.

1.2 Micromagnetics

Although the basic precessional nature of magnetisation motion could have been introduced without calling upon quantum mechanics, the analysis of the preceding section has the merit of being a self-contained approach to the derivation of Eq. (1.12), obtaining en passant the definition of the gyromagnetic constant γ_0. Unfortunately, if one's goals extend beyond the (almost) purely academic problem of describing the time evolution of a *single* magnetic moment under the action of an external magnetic field, fully *ab initio* methods soon reveal their limitations. In particular, the description of the intricacies of spatial magnetisation distributions in ferromagnetic materials is clearly unattainable if relying exclusively on such methods. The problem is not so much the inadequacy of first principles theoretical formulations but the huge number of individual magnetic moments to be dealt with in practice. It appears clear that a continuous representation of magnetisation must be sought for.

This is the aim of a classical theory of ferromagnetic materials based on a phenomenological description of magnetisation direction, and ultimately magnetisation motion, called micromagnetics [10]. Magnetisation is here represented, in both space and time, by a continuous vector field $\mathbf{M}(\mathbf{r}, t) = M_s \mathbf{m}(\mathbf{r}, t)$, of constant magnitude M_s, which should now be understood as a magnetic moment per unit volume. This imposed constraint on the norm of $\mathbf{M}$ (or $\mathbf{m}$) holds valid in the zero temperature limit and as long as one avoids the description of micromagnetic structures such as Bloch points.

Spatial distributions of magnetisation introduce a new degree of complexity in the derivation of the equations of magnetisation motion. Useful analogies can be drawn from well-established variational principles in classical mechanics. The importance of such analogies is all the most relevant since the derivation of the equations of motion in terms of variational principles is the route that must be followed when trying to describe non-mechanical systems within the mathematical framework of analytical classical mechanics. This statement provides the basic motivation for the digression which is about to follow.

1.2.1 Variational Principles for Continuous Systems

General expressions for the equations of motion of mechanical systems can be obtained from a variational principle known as Hamilton's principle [20].

The motion of the system from time t_1 to time t_2 is such that the action integral

$$I = \int_{t_1}^{t_2} L\, dt \quad , \tag{1.16}$$

where L is the Lagrangian functional, has a stationary value[(b)].

For *conservative* mechanical systems L can be simply defined as the excess of kinetic over potential energy. The above formulation is such that the explicit functional dependence of L on the system's generalised coordinates, i.e the system's degrees of freedom, need not be specified.

Consider an arbitrary continuous vector field defined in three-dimensional space, say $\mathbf{m}(\mathbf{r}, t)$, and a Lagrangian functional of the form

$$L = \int_\Omega \mathcal{L}\, d\mathbf{r} + \int_\Gamma \mathcal{E}'\, d\mathbf{r} \quad . \tag{1.17}$$

The second integral above accounts for *potential* energy contributions linked to the surface Γ, enclosing the volume Ω, whereas the first contains volume terms of both kinetic and potential origin. In the most general case, $\mathcal{L}$, besides being a function of $\mathbf{m}$ and $\dot{\mathbf{m}}$[(c)], also involves the spatial derivatives of $\mathbf{m}$, namely $\boldsymbol{\nabla}\mathbf{m}$[(d)]. Without loss of generality, $\mathcal{E}'$ will be assumed to be a sole function of $\mathbf{m}$, a restriction compatible with micromagnetics. Of course, both $\mathcal{L}$ and $\mathcal{E}'$ might also well be explicit functions of $\mathbf{r}$ and t. Thus the Lagrangian densities can be formally written as

$$\mathcal{L} = \mathcal{L}(\mathbf{m}, \dot{\mathbf{m}}, \boldsymbol{\nabla}\mathbf{m}, \mathbf{r}, t) \quad \text{and} \quad \mathcal{E}' = \mathcal{E}'(\mathbf{m}, \mathbf{r}, t) \quad . \tag{1.18}$$

Hamilton's principle can be restated by saying that the system's motion is such that the variation of the action integral is zero for fixed t_1 and t_2, i.e.

$$\delta I = \delta \int_{t_1}^{t_2} \left(\int_\Omega \mathcal{L}\, d\mathbf{r} + \int_\Gamma \mathcal{E}'\, d\mathbf{r} \right) dt = \int_{t_1}^{t_2} \left(\int_\Omega \delta\mathcal{L}\, d\mathbf{r} + \int_\Gamma \delta\mathcal{E}'\, d\mathbf{r} \right) dt = 0 \quad , \tag{1.19}$$

$$\delta\mathbf{m}(\mathbf{r}, t_1) = \delta\mathbf{m}(\mathbf{r}, t_2) = 0 \quad . \tag{1.20}$$

It should be stressed that no restrictions are imposed upon $\delta\mathbf{m}$ on the surface Γ, or in the volume Ω itself, for times other than t_1 and t_2. Under this limitation, the variation $\delta\mathbf{m}$ is therefore to be treated as arbitrary.

[(b)] For a comprehensive discussion about the limits of applicability of Hamilton's principle the reader may profitably refer to Lanczos [21].

[(c)] The superscript dot notation stands for a partial time derivative.

[(d)] $\boldsymbol{\nabla}\mathbf{m} \equiv \partial m_i / \partial r_j$ is a second rank tensor.

The calculus of variations [21] provides for the mathematical tools needed to tackle the problem enunciated above. Carrying out the variations $\delta\mathcal{L}$ and $\delta\mathcal{E}'$ yields

$$\delta I = \int_{t_1}^{t_2} \int_{\Omega} \left[\frac{\partial \mathcal{L}}{\partial \mathbf{m}} \cdot \delta\mathbf{m} + \frac{\partial \mathcal{L}}{\partial(\boldsymbol{\nabla}\mathbf{m})} \cdot \delta(\boldsymbol{\nabla}\mathbf{m}) + \frac{\partial \mathcal{L}}{\partial \dot{\mathbf{m}}} \cdot \delta\dot{\mathbf{m}} \right] d\mathbf{r}\, dt + \int_{t_1}^{t_2} \int_{\Gamma} \left(\frac{\partial \mathcal{E}'}{\partial \mathbf{m}} \cdot \delta\mathbf{m} \right) d\mathbf{r}\, dt \quad . \tag{1.21}$$

Since the operator δ commutes with both $\boldsymbol{\nabla}$ and d/dt, the following relations hold

$$\frac{\partial \mathcal{L}}{\partial(\boldsymbol{\nabla}\mathbf{m})} \cdot \delta(\boldsymbol{\nabla}\mathbf{m}) = \boldsymbol{\nabla} \cdot \left[\frac{\partial \mathcal{L}}{\partial(\boldsymbol{\nabla}\mathbf{m})} \cdot \delta\mathbf{m} \right] - \left[\boldsymbol{\nabla} \cdot \frac{\partial \mathcal{L}}{\partial(\boldsymbol{\nabla}\mathbf{m})} \right] \cdot \delta\mathbf{m} \quad , \tag{1.22}$$

$$\frac{\partial \mathcal{L}}{\partial \dot{\mathbf{m}}} \cdot \delta\dot{\mathbf{m}} = \frac{d}{dt} \left(\frac{\partial \mathcal{L}}{\partial \dot{\mathbf{m}}} \cdot \delta\mathbf{m} \right) - \left(\frac{d}{dt} \frac{\partial \mathcal{L}}{\partial \dot{\mathbf{m}}} \right) \cdot \delta\mathbf{m} \quad . \tag{1.23}$$

Because $\delta\mathbf{m}$ vanishes at the integration endpoints t_1 and t_2

$$\int_{t_1}^{t_2} \frac{d}{dt} \left(\frac{\partial \mathcal{L}}{\partial \dot{\mathbf{m}}} \cdot \delta\mathbf{m} \right) dt = 0 \quad . \tag{1.24}$$

Making use of the divergence theorem of vectorial calculus

$$\int_{\Omega} \boldsymbol{\nabla} \cdot \left[\frac{\partial \mathcal{L}}{\partial(\boldsymbol{\nabla}\mathbf{m})} \cdot \delta\mathbf{m} \right] d\mathbf{r} = \int_{\Gamma} \left\{ \left[\frac{\partial \mathcal{L}}{\partial(\boldsymbol{\nabla}\mathbf{m})} \cdot \delta\mathbf{m} \right] \cdot \hat{\mathbf{n}} \right\} d\mathbf{r} \quad , \tag{1.25}$$

where $\hat{\mathbf{n}}$ stands for the unit vector normal to the surface Γ, Eq. (1.21) can be written as

$$\delta I = \int_{t_1}^{t_2} \int_{\Omega} \left\{ \left[\frac{\partial \mathcal{L}}{\partial \mathbf{m}} - \boldsymbol{\nabla} \cdot \frac{\partial \mathcal{L}}{\partial(\boldsymbol{\nabla}\mathbf{m})} - \frac{d}{dt} \frac{\partial \mathcal{L}}{\partial \dot{\mathbf{m}}} \right] \cdot \delta\mathbf{m} \right\} d\mathbf{r}\, dt + \int_{t_1}^{t_2} \int_{\Gamma} \left\{ \left[\frac{\partial \mathcal{E}'}{\partial \mathbf{m}} + \frac{\partial \mathcal{L}}{\partial(\boldsymbol{\nabla}\mathbf{m})} \cdot \hat{\mathbf{n}} \right] \cdot \delta\mathbf{m} \right\} d\mathbf{r}\, dt \quad . \tag{1.26}$$

By the so-called fundamental lemma of the calculus of variations, the arbitrary nature of $\delta\mathbf{m}$ implies the vanishing of the expressions inside square brackets

$$\frac{\partial \mathcal{L}}{\partial \mathbf{m}} - \boldsymbol{\nabla} \cdot \frac{\partial \mathcal{L}}{\partial(\boldsymbol{\nabla}\mathbf{m})} - \frac{d}{dt} \frac{\partial \mathcal{L}}{\partial \dot{\mathbf{m}}} = 0 \quad \text{in the volume} \quad , \tag{1.27}$$

$$\frac{\partial \mathcal{E}'}{\partial \mathbf{m}} + \frac{\partial \mathcal{L}}{\partial(\boldsymbol{\nabla}\mathbf{m})} \cdot \hat{\mathbf{n}} = 0 \quad \text{on the surface} \quad . \tag{1.28}$$

Introducing the notion of functional derivative

$$\frac{\delta}{\delta \mathbf{m}} \equiv \frac{\partial}{\partial \mathbf{m}} - \boldsymbol{\nabla} \cdot \frac{\partial}{\partial(\boldsymbol{\nabla}\mathbf{m})} \quad , \tag{1.29}$$

Eqs. (1.27) and (1.28) can be put in a notation more closely resembling the Euler-Lagrange equations for discrete systems

$$\frac{\delta \mathcal{L}}{\delta \mathbf{m}} - \frac{d}{dt}\frac{\partial \mathcal{L}}{\partial \dot{\mathbf{m}}} = 0 \quad \text{in the volume} \quad , \tag{1.30}$$

$$\frac{\partial \mathcal{E}'}{\partial \mathbf{m}} + \frac{\partial \mathcal{L}}{\partial (\boldsymbol{\nabla} \mathbf{m})} \cdot \hat{\mathbf{n}} = 0 \quad \text{on the surface} \quad . \tag{1.31}$$

A necessary condition for deriving the equations above was the arbitrary nature of the variation $\delta\mathbf{m}$. Generally speaking mechanical as well as non-mechanical systems evolve in time subjected to constraints. As could be hinted from the discussion of Sect. 1.1, and the introductory remarks of Sect. 1.2, one is interested in a particular kinematic constraint, namely that the vector field $\mathbf{m}(\mathbf{r}, t)$ should preserve a constant magnitude. Such a constraint can be conveniently expressed in terms of the variation of $\mathbf{m}$ as

$$\mathbf{m} \cdot \delta\mathbf{m} = 0 \quad . \tag{1.32}$$

The method of Lagrange undetermined multipliers [20] provides for an elegant way of handling kinematic constraints of the form above. The equations of motion (1.30) and (1.31) hold true provided the additional term $\lambda\mathbf{m}$, where λ is an unknown scalar quantity, is added to the left-hand side of Eq. (1.30). Therefore, the equations of motion for a continuous system associated with an arbitrary vector field $\mathbf{m}(\mathbf{r}, t)$ of constant magnitude, and described by the Lagrangian functional defined by Eqs. (1.17) and (1.18), can be written as

$$\frac{\delta \mathcal{L}}{\delta \mathbf{m}} - \frac{d}{dt}\frac{\partial \mathcal{L}}{\partial \dot{\mathbf{m}}} + \lambda\mathbf{m} = 0 \quad \text{in the volume} \quad , \tag{1.33}$$

$$\frac{\partial \mathcal{E}'}{\partial \mathbf{m}} + \frac{\partial \mathcal{L}}{\partial (\boldsymbol{\nabla} \mathbf{m})} \cdot \hat{\mathbf{n}} = 0 \quad \text{on the surface} \quad . \tag{1.34}$$

1.2.2 Brown's and Gyromagnetic Equations

The equations of motion (1.33) and (1.34) clearly hold true in micromagnetics. Further insight can be gained about their nature without the need to explicitly specify the functional dependence of the Lagrangian densities $\mathcal{L}$ and $\mathcal{E}'$. Consider the static equilibrium

limit of such equations, i.e.

$$\frac{\delta \mathcal{E}}{\delta \mathbf{m}} + \lambda \mathbf{m} = 0 \quad \text{in the volume} \quad , \tag{1.35}$$

$$\frac{\partial \mathcal{E}'}{\partial \mathbf{m}} + \frac{\partial \mathcal{E}}{\partial (\boldsymbol{\nabla} \mathbf{m})} \cdot \hat{\mathbf{n}} = 0 \quad \text{on the surface} \quad , \tag{1.36}$$

where $\mathcal{E}$ represents the volume *potential* energy density of the system, henceforth simply called volume energy density. As anticipated, the static equilibrium equations above can be obtained by equating to zero the variation of the total energy, i.e. $\delta E = 0$, with

$$E = \int_{\Omega} \mathcal{E} \, d\mathbf{r} + \int_{\Gamma} \mathcal{E}' \, d\mathbf{r} \quad . \tag{1.37}$$

Multiplying the volume equation (1.35) by $\mathbf{m}\times$ yields

$$\mathbf{m} \times \frac{\delta \mathcal{E}}{\delta \mathbf{m}} = 0 \quad \text{in the volume} \quad . \tag{1.38}$$

Using the SI system of units, a vector quantity having the dimensions of a magnetic field can be defined from the functional derivative of the volume energy density as

$$\mathbf{H}_{\text{eff}} = -\frac{1}{\mu_0 M_s} \frac{\delta \mathcal{E}}{\delta \mathbf{m}} \quad , \tag{1.39}$$

and shall be called the effective field. The static equilibrium equations appear now as a torque condition on $\mathbf{M}$ plus a boundary condition, namely

$$\mathbf{M} \times \mathbf{H}_{\text{eff}} = 0 \quad \text{in the volume} \quad , \tag{1.40}$$

$$\frac{\partial \mathcal{E}'}{\partial \mathbf{m}} + \frac{\partial \mathcal{E}}{\partial (\boldsymbol{\nabla} \mathbf{m})} \cdot \hat{\mathbf{n}} = 0 \quad \text{on the surface} \quad . \tag{1.41}$$

Within the framework of micromagnetics the equations above are usually called Brown's equations. It ought to be emphasised that these equations were derived without any knowledge of the physical origins of energy terms. In particular, the boundary condition linked to energy contributions explicitly dependent on $\boldsymbol{\nabla} \mathbf{m}$ is seen to ensue directly from general variational principles, without the need for the usual cumbersome variations of explicit energy functionals [10, 22].

The basic precessional nature of magnetisation motion around some instantaneous axis of rotation directed along $\boldsymbol{\omega}$ follows directly from the kinematical constraint $\mathbf{m} \cdot \delta \mathbf{m} = 0$. Efforts made in deriving the general form of the equations of motion from a variational

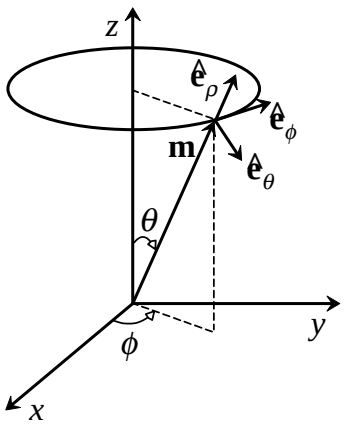

Figure 1.2: Coordinate axes used when representing the precessional motion of **m**.

principle would intuitively be anticipated to lead to the equations of magnetisation motion. Unfortunately such will not be the case since a *kinetic* energy density functional cannot be derived from classical physical principles. Quantum mechanics is of no help either since no kinetic energy is associated with the motion of the magnetic moment **M** (see Eq. (1.5)). When dealing with this problem, the symmetric top is usually taken as the classical analogue to the intrinsic magnetic moment associated with spin. Correct expressions for the kinetic energy term can indeed be obtained by considering the most general movement of a top, arbitrarily imposing, however, that motion other than rotation about its symmetry axis yields no contribution to the kinetic energy. This was the approach followed by Brown in his seminal book [10], but the reader is instantly warned about the *classically impossible* limit of such procedure. On the same question Döring [23] was even more blunt. A suitable expression for this kinetic term was simply presented with no justifications whatsoever. It reads

$$\mathcal{T} = -\frac{\mu_0 M_s}{\gamma_0}\dot{\phi}\cos\theta \quad , \tag{1.42}$$

with the angles ϕ and θ being those in Fig. 1.2.

Between a poor analogy and a sound postulate the choice will be made for the latter. The gyromagnetic equation (1.12) will be assumed to hold valid when the external magnetic field is replaced by the effective magnetic field $\mathbf{H}_{\text{eff}}$, i.e., instantaneously, magnetisation will precess around $\mathbf{H}_{\text{eff}}$ at an angular velocity $\boldsymbol{\omega} = \gamma_0 \mathbf{H}_{\text{eff}}$. Taken in connection with Brown's equations, this axiom foresees that the equations of magnetisation motion

(gyromagnetic equations) should be written as

$$\frac{\partial \mathbf{M}}{\partial t} = -\gamma_0 \left(\mathbf{M} \times \mathbf{H}_{\text{eff}}\right) \quad \text{in the volume} \quad , \tag{1.43}$$

$$\frac{\partial \mathcal{E}'}{\partial \mathbf{m}} + \frac{\partial \mathcal{E}}{\partial (\boldsymbol{\nabla} \mathbf{m})} \cdot \hat{\mathbf{n}} = \mathbf{0} \quad \text{on the surface} \quad . \tag{1.44}$$

The boundary condition above holds true in actual motion just as in equilibrium configurations, a fact all too often disregarded in numerical micromagnetics.

1.2.3 The Landau-Lifshitz-Gilbert Equation

A damping term allows a precessing magnetisation vector to lose energy and approach its static equilibrium direction along $\mathbf{H}_{\text{eff}}$. By far, the simplest way of introducing a damping or dissipation term in the gyromagnetic equation consists in adding to the effective field $\mathbf{H}_{\text{eff}}$ an additional contribution of the form

$$-\frac{\alpha}{\gamma_0 M_s} \frac{\partial \mathbf{M}}{\partial t} \quad , \tag{1.45}$$

where α is a dimensionless constant. This additional term is strictly phenomenological since it is not derived from any energy transfer mechanism or model. Inserting Eq. (1.45) in Eq. (1.43) yields

$$\frac{\partial \mathbf{M}}{\partial t} = -\gamma_0 \left(\mathbf{M} \times \mathbf{H}_{\text{eff}}\right) + \frac{\alpha}{M_s} \left(\mathbf{M} \times \frac{\partial \mathbf{M}}{\partial t} \right) \quad . \tag{1.46}$$

This form of the equation is due to Gilbert [3]. It can be shown to be equivalent to the older formulation due to Landau and Lifshitz [2]. Simply applying $\mathbf{M}\times$ to both sides of Eq. (1.46) yields

$$\mathbf{M} \times \frac{\partial \mathbf{M}}{\partial t} = -\gamma_0 \mathbf{M} \times \left(\mathbf{M} \times \mathbf{H}_{\text{eff}}\right) - \alpha M_s \frac{\partial \mathbf{M}}{\partial t} \quad . \tag{1.47}$$

Substituting the right-hand side of this equation for $\mathbf{M} \times \partial \mathbf{M}/\partial t$ in Eq. (1.46), and rearranging, leads to

$$\frac{\partial \mathbf{M}}{\partial t} = -\gamma_0' \left(\mathbf{M} \times \mathbf{H}_{\text{eff}}\right) - \lambda \left[\mathbf{M} \times \left(\mathbf{M} \times \mathbf{H}_{\text{eff}}\right)\right] \quad , \tag{1.48}$$

with

$$\gamma_0' = \frac{\gamma_0}{1+\alpha^2} \qquad \text{and} \qquad \lambda = \frac{\alpha}{1+\alpha^2} \frac{\gamma_0}{M_s} \quad . \tag{1.49}$$

This is the older form of Landau and Lifshitz [2]. Presenting the set of equations above in the geometrical form of Eq. (1.48), but using the Gilbert damping constant α and the

gyromagnetic constant γ_0, the usually designated Landau-Lifshitz-Gilbert (LLG) equation of magnetisation motion is obtained, namely

$$\left(1+\alpha^2\right)\frac{\partial \mathbf{M}}{\partial t} = -\gamma_0\left(\mathbf{M}\times\mathbf{H}_{\text{eff}}\right) - \frac{\gamma_0\alpha}{M_s}\left[\mathbf{M}\times\left(\mathbf{M}\times\mathbf{H}_{\text{eff}}\right)\right] \quad . \tag{1.50}$$

As mentioned above magnetisation motion towards $\mathbf{H}_{\text{eff}}$ is associated with a change in energy. The variational techniques employed in Sect. 1.2.1 allow for the derivation of a closed form expression of the energy dissipation rate, i.e. the time derivative of the system's total energy

$$\frac{dE}{dt} = \int_\Omega \left[\frac{\partial \mathcal{E}}{\partial \mathbf{m}}\cdot\frac{\partial \mathbf{m}}{\partial t} + \frac{\partial \mathcal{E}}{\partial(\boldsymbol{\nabla}\mathbf{m})}\cdot\frac{\partial}{\partial t}(\boldsymbol{\nabla}\mathbf{m}) + \frac{\partial \mathcal{E}}{\partial t}\right] d\mathbf{r} + \int_\Gamma \left(\frac{\partial \mathcal{E}'}{\partial \mathbf{m}}\cdot\frac{\partial \mathbf{m}}{\partial t} + \frac{\partial \mathcal{E}'}{\partial t}\right) d\mathbf{r} \quad . \tag{1.51}$$

Making use of the boundary condition $(1.44)^{(e)}$, the equation above can be simply written as

$$\begin{aligned}\frac{dE}{dt} &= \int_\Omega \left\{\frac{\partial \mathcal{E}}{\partial \mathbf{m}}\cdot\frac{\partial \mathbf{m}}{\partial t} - \left[\boldsymbol{\nabla}\cdot\frac{\partial \mathcal{E}}{\partial(\boldsymbol{\nabla}\mathbf{m})}\right]\cdot\frac{\partial \mathbf{m}}{\partial t} + \frac{\partial \mathcal{E}}{\partial t}\right\} d\mathbf{r} + \int_\Gamma \frac{\partial \mathcal{E}'}{\partial t}\, d\mathbf{r} \\ &= \int_\Omega \left(\frac{\delta \mathcal{E}}{\delta \mathbf{m}}\cdot\frac{\partial \mathbf{m}}{\partial t} + \frac{\partial \mathcal{E}}{\partial t}\right) d\mathbf{r} + \int_\Gamma \frac{\partial \mathcal{E}'}{\partial t}\, d\mathbf{r} \quad .\end{aligned} \tag{1.52}$$

In the important limiting situation where *none of the energy densities explicitly depend on time*, the equation above reduces to

$$\frac{dE}{dt} = \int_\Omega \frac{\delta \mathcal{E}}{\delta \mathbf{m}}\cdot\frac{\partial \mathbf{m}}{\partial t}\, d\mathbf{r} \quad . \tag{1.53}$$

This equation can be rewritten by using the Gilbert form of the LLG equation. Multiplying Eq. (1.46) respectively by $\mathbf{H}_{\text{eff}}$ and $\partial\mathbf{M}/\partial t$ yields

$$\mathbf{H}_{\text{eff}}\cdot\frac{\partial \mathbf{M}}{\partial t} = -\frac{\alpha}{M_s}\frac{\partial \mathbf{M}}{\partial t}\cdot\left(\mathbf{M}\times\mathbf{H}_{\text{eff}}\right) \quad \text{and} \quad \frac{\partial \mathbf{M}}{\partial t}\cdot\left(\mathbf{M}\times\mathbf{H}_{\text{eff}}\right) = -\frac{1}{\gamma_0}\left(\frac{\partial \mathbf{M}}{\partial t}\right)^2 \quad . \tag{1.54}$$

Combining the expressions above leads to

$$\mathbf{H}_{\text{eff}}\cdot\frac{\partial \mathbf{M}}{\partial t} = \frac{\alpha}{\gamma_0 M_s}\left(\frac{\partial \mathbf{M}}{\partial t}\right)^2 \quad . \tag{1.55}$$

Being derived from the LLG equation the relation above holds valid at every point in space and at every time t. The total energy dissipation rate of the system may now be written as

$$\frac{dE}{dt} = -\frac{\alpha\mu_0}{\gamma_0 M_s}\int_\Omega \left(\frac{\partial \mathbf{M}}{\partial t}\right)^2 d\mathbf{r} \quad . \tag{1.56}$$

$^{(e)}$Note that, in full analogy with Eq. (1.22), the additional relation holds valid $\frac{\partial \mathcal{L}}{\partial(\boldsymbol{\nabla}\mathbf{m})}\cdot\frac{\partial}{\partial t}(\boldsymbol{\nabla}\mathbf{m}) = \boldsymbol{\nabla}\cdot\left[\frac{\partial \mathcal{L}}{\partial(\boldsymbol{\nabla}\mathbf{m})}\cdot\frac{\partial \mathbf{m}}{\partial t}\right] - \left[\boldsymbol{\nabla}\cdot\frac{\partial \mathcal{L}}{\partial(\boldsymbol{\nabla}\mathbf{m})}\right]\cdot\frac{\partial \mathbf{m}}{\partial t}$.

There is, however, no local counterpart to this equation. It holds only valid in the integral form given above. Only in the single magnetic moment approximation is one allowed to write a similar equation involving now the time derivative of the total energy density.

Although the mathematical form of the equation of magnetisation motion depends upon the dissipation models considered, it is interesting to note that from a strictly analytical standpoint the rate of change of the magnetisation vector $\mathbf{M}$ may mathematically be expressed in the three orthogonal vectors $\mathbf{M}$, $\mathbf{M} \times \mathbf{H}_{\text{eff}}$, and $\mathbf{M} \times (\mathbf{M} \times \mathbf{H}_{\text{eff}})$ as

$$\frac{\partial \mathbf{M}}{\partial t} = \eta \mathbf{M} - \zeta \left(\mathbf{M} \times \mathbf{H}_{\text{eff}} \right) - \xi \left[\mathbf{M} \times \left(\mathbf{M} \times \mathbf{H}_{\text{eff}} \right) \right] \quad . \tag{1.57}$$

The three functions η, ζ, and ξ are unknown scalar functions of $\mathbf{M}$, $\mathbf{H}_{\text{eff}}$, and the intrinsic material parameters. The question is now to evaluate the functional dependence of η, ζ, and ξ. If we make the assumption that the magnetic response consists of a pure rotation, as seen above, then η must vanish. In the absence of any further theoretical information, we may just assume that the two remaining functions, ζ and ξ, are constants. We immediately see that the resulting equation is just the Landau-Lifshitz equation of magnetisation motion.

1.2.4 Energy and Effective Field Expressions

At this point only the nature of the energy interactions needs to be specified. The approach to be followed will be strictly phenomenological, although quantum mechanics can be relied upon to provide valuable guidelines in determining suitable mathematical expressions for some energy contributions. For a more comprehensive discussion on the physical nature of energy contributions the reader is directed to Aharoni's book [22] and references therein.

Exchange interactions proceed from the energy penalty associated with non-uniform magnetisation distributions in ferromagnetic materials. The phenomenological expression of this energy density can be written as

$$\mathcal{E}_{\text{exc}} = A \left(\boldsymbol{\nabla} \mathbf{m} \right)^2 \quad , \tag{1.58}$$

where A (J/m) is a material constant at a given temperature, usually called the exchange stiffness constant. The expression above can be shown to proceed from the Heisenberg Hamiltonian in the limit of minute rotations of magnetic moment between localised spins. The associated effective field contribution can be immediately determined by carrying out

the functional derivative of Eq. (1.58)

$$\mathbf{H}_{\text{exc}} = \frac{2A}{\mu_0 M_s}(\nabla^2 \mathbf{m}) \quad . \tag{1.59}$$

In addition, since $\mathcal{E}_{\text{exc}}$ explicitly depends on $\boldsymbol{\nabla}\mathbf{m}$, and is the sole energy density term to do so, in the absence of any surface energy contribution, the boundary condition in Brown's equations now read

$$2A(\boldsymbol{\nabla}\mathbf{m}) \cdot \hat{\mathbf{n}} = \mathbf{0} \Longrightarrow (\boldsymbol{\nabla}\mathbf{m}) \cdot \hat{\mathbf{n}} \equiv \frac{\partial \mathbf{m}}{\partial \hat{\mathbf{n}}} = \mathbf{0} \quad . \tag{1.60}$$

The equivalence in the equation above can be immediately proved by carrying out, componentwise, the scalar product shown.

Expressions for the anisotropy energy density may simply be devised in order to reflect the crystallographic symmetries of the system, i.e. the directions of preferred magnetisation directions. From a physical perspective they result from spin-orbit interactions. Keeping only the lowest order term in a Taylor expansion, the *uniaxial* anisotropy energy density reads

$$\mathcal{E}_{\text{ani}} = K[1 - (\mathbf{m} \cdot \hat{\mathbf{k}})^2] \quad , \tag{1.61}$$

where K (J/m^3), the anisotropy constant, is a material parameter and $\hat{\mathbf{k}}$ defines the easy axis direction.

As already mentioned in Sect. 1.1, an external magnetic field is responsible for a Zeeman type contribution to the energy density

$$\mathcal{E}_a = -\mu_0 \left(\mathbf{M} \cdot \mathbf{H}_a\right) = -\mu_0 M_s \left(\mathbf{m} \cdot \mathbf{H}_a\right) \quad . \tag{1.62}$$

A demagnetising field $\mathbf{H}_d$, arising from the magnetisation distribution $\mathbf{M}(\mathbf{r})$, provides for an additional contribution to the total magnetic field $\mathbf{H}$. From Maxwell's equations, an explicit expression for $\mathbf{H}_d$ can conveniently be expressed by defining two scalar quantities, the volume charge density ρ and the surface charge density λ as

$$\rho = -\boldsymbol{\nabla} \cdot \mathbf{m} \quad , \tag{1.63}$$

$$\lambda = \mathbf{m} \cdot \hat{\mathbf{n}} \quad . \tag{1.64}$$

Using such quantities the scalar potential Φ_d of the stray field is given by

$$\Phi_d(\mathbf{r}) = \frac{M_s}{4\pi}\left[\int_\Omega \frac{\rho(\mathbf{r}')}{|\mathbf{r} - \mathbf{r}'|} d\mathbf{r}' + \int_\Gamma \frac{\lambda(\mathbf{r}')}{|\mathbf{r} - \mathbf{r}'|} d\mathbf{r}'\right] \quad , \tag{1.65}$$

and $\mathbf{H}_d$ can be expressed as $-\boldsymbol{\nabla}\Phi_d$

$$\mathbf{H}_d(\mathbf{r}) = \frac{M_s}{4\pi}\left[\int_\Omega \frac{(\mathbf{r}-\mathbf{r}')\rho(\mathbf{r}')}{|\mathbf{r}-\mathbf{r}'|^3}d\mathbf{r}' + \int_\Gamma \frac{(\mathbf{r}-\mathbf{r}')\lambda(\mathbf{r}')}{|\mathbf{r}-\mathbf{r}'|^3}d\mathbf{r}'\right] \quad . \tag{1.66}$$

The energy density associated with the demagnetising field is given by

$$\mathcal{E}_d = -\frac{1}{2}\mu_0\left(\mathbf{M}\cdot\mathbf{H}_d\right) = -\frac{1}{2}\mu_0 M_s\left(\mathbf{m}\cdot\mathbf{H}_d\right) \quad , \tag{1.67}$$

where the 1/2 prefactor stems from the fact that $\mathbf{M}$ is the source of $\mathbf{H}_d$. Contrary to the Zeeman contribution to the total energy, the stray field energy, obtained through an integration over the volume and the boundary surface, is necessarily positive or nil. It follows that in a ferromagnetic material where the magnetostatic energy becomes the leading contribution, energy may only be minimised by the pole avoidance principle. This means that, whenever possible, the magnetisation will tend to be parallel to the boundary surfaces and adopt configurations satisfying $\boldsymbol{\nabla}\cdot\mathbf{m} = 0$ in the volume. Clearly this may only occur at the expense of both exchange and anisotropy energies.

1.3 Reduced System of Units

All the equations presented in the preceding sections have been written using the International System of Units (SI). However, due to historic reasons, most of the specialised literature in the field of magnetism still employs the CGS system of units. Only in the last decade has the SI system started to creep in. Unfortunately, the problem does not circumscribe to a conversion of physical quantities, for which conversion tables could alleviate one's pain, but implies the rewriting of even the most basic equations of electromagnetism. The fact remains that nowadays a fair knowledge of both systems is almost a prerequisite. In order to avoid possible confusions, an attempt is made below at defining a reduced (dimensionless) system that allows the basic equations of micromagnetics to be written in an invariant form.

From the constitutive relation $\mathbf{B} = \mu_0\left(\mathbf{H}+\mathbf{M}\right)$ it appears highly convenient to define the reduced magnetic field as $\mathbf{h} = \mathbf{H}/M_s$, so as to maintain the unit vector $\mathbf{m}$ as the reduced magnetisation. The expression for the Zeeman energy density, together with the definitions of reduced magnetic field and magnetisation, provides for an appropriate definition of reduced energy densities $w = \mathcal{E}/\mu_0 M_s^2$. On the other hand, the gyromagnetic equation (1.43) suggests the definition of the reduced time $\tau = \gamma_0 M_s t$. The ensemble of the proposed transformations, for both the SI and the CGS systems, and the ensuing

	Reduced	SI	CGS
Magnetisation	$\mathbf{m}$	$\mathbf{M} = M_s\mathbf{m}$	$\mathbf{M} = M_s\mathbf{m}$
Magnetic field	$\mathbf{h}$	$\mathbf{H} = M_s\mathbf{h}$	$\mathbf{H} = 4\pi M_s\mathbf{h}$
	$\mathbf{b}$	$\mathbf{B} = \mu_0 M_s\mathbf{b}$	$\mathbf{B} = 4\pi M_s\mathbf{b}$
Energy density	w	$\mathcal{E} = \mu_0 M_s^2 w$	$\mathcal{E} = 4\pi M_s^2 w$
Time	τ	$t = \tau/(\gamma_0 M_s)$	$t = \tau/(4\pi\gamma M_s)$

Table 1.1: Reduced (dimensionless) variables and conversion rules for both the SI and the CGS systems.

	Reduced
Constitutive relation	$\mathbf{b} = \mathbf{h} + \mathbf{m}$
Effective field definition	$\mathbf{h}_{\text{eff}} = -\delta w/\delta\mathbf{m}$
LLG equation	$\left(1+\alpha^2\right)\partial\mathbf{m}/\partial\tau = -\left(\mathbf{m}\times\mathbf{h}_{\text{eff}}\right) - \alpha\left[\mathbf{m}\times\left(\mathbf{m}\times\mathbf{h}_{\text{eff}}\right)\right]$
	$\partial\mathbf{m}/\partial\tau = -\left(\mathbf{m}\times\mathbf{h}_{\text{eff}}\right) + \alpha\left[\mathbf{m}\times\left(\partial\mathbf{m}/\partial\tau\right)\right]$
Exchange energy density	$w_{\text{exc}} = (\Lambda^2/2)(\boldsymbol{\nabla}\mathbf{m})^2$
Uniaxial anisotropy energy density	$w_{\text{ani}} = (Q/2)[1 - (\mathbf{m}\cdot\hat{\mathbf{k}})^2]$
Zeeman energy density	$w_a = -\left(\mathbf{m}\cdot\mathbf{h}_a\right)$
Demagnetising energy density	$w_d = -(1/2)\left(\mathbf{m}\cdot\mathbf{h}_d\right)$

Table 1.2: Reduced equations of micromagnetics.

dimensionless formulation of the most widely used equations, are summarised in Tables 1.1 and 1.2, respectively.

The exchange stiffness constant A is conveniently replaced by $\Lambda^2/2$, where Λ is the well-known exchange length given by

$$\Lambda = \sqrt{\frac{2A}{\mu_0 M_s^2}} \quad \left(\sqrt{\frac{A}{2\pi M_s^2}} \quad \text{in CGS}\right) \quad . \tag{1.68}$$

Similarly, an anisotropy constant K is replaced by $Q/2$, with Q the so-called quality factor, given by

$$Q = \frac{2K}{\mu_0 M_s^2} \quad \left(\frac{K}{2\pi M_s^2} \quad \text{in CGS}\right) \quad . \tag{1.69}$$

The exchange and anisotropy energy density expressions given in Table 1.2, unfamiliar as they might be, are the exact equivalent of those given by Hubert and Schäfer [24].

It ought to be noticed that the only dimensional parameter left in the equations is the

exchange length Λ. Its dimensions are that of a length and this is linked with the fact that the nabla operator $\boldsymbol{\nabla}$ has the dimensions of the inverse of a length. The decision was made to keep the standard definition of $\boldsymbol{\nabla}$. No one should find very demanding the conversion of lengths between different systems of units. In the definition of the reduced time τ in the CGS system the gyromagnetic ratio γ is used instead of the gyromagnetic constant γ_0. The reader should be aware of the fact that in the CGS system γ is usually defined as a positive quantity, contrary to the definition in Eq. (1.2). Only the dimensionless form of the equations will be used in the following sections. When appropriate, explicit numerical values will be given in both SI and CGS units.

Summary

The gyromagnetic equations of motion have been derived from a purely quantum-mechanical approach. On the other hand, a fully variational approach enables the complete derivation of Brown's equations for general (volume as well as surface) energy contributions, and this without the usual cumbersome variational expressions of explicit energy terms. This viewpoint on the basic equations of micromagnetics additionally provides for a clear insight into the relationship existing between the total rate of energy dissipation and the phenomenological damping parameter in the Landau-Lifshitz-Gilbert equation. Boundary conditions associated with the LLG equation straightforwardly derive from this variational procedure. Finally, a reduced (dimensionless) set of units is introduced, alloying for a unified writing of the basic equations of micromagnetism in both the SI and CGS systems.

Chapter 2

Macrospin (Precessional Dynamics)

The most simple problem in micromagnetics is that of a uniformly magnetised body immersed in an external magnetic field and exhibiting a coherent magnetisation motion. In such situations, the magnetic system under study can be conveniently described by a sole magnetisation vector. The magnetic body is thus treated in the single spin limit, also called a macrospin. The interest in considering such a simplistic model is double. First, a large corpus of data shows that the quasi-static reversal properties of thin films of sizeable dimensions may often accurately be described within the macrospin approximation (see, for instance, [25]). Another case where this approximation is expected to efficiently apply concerns patterned elements with an almost uniform magnetisation distribution due to lateral dimensions not exceeding, say, a few times the exchange length [26]. Second, even when this approximation is clearly expected not to be an adequate description of the magnetic system under study, it is still often essential to characterise the discrepancies between a coherent rotation model and full-scale simulations taking into account the spatial degrees of freedom of the magnetisation. In other words, it allows for establishing quantitative landmarks on which to measure the degree of applicability of a model that remains so attractive due to its simplicity.

2.1 Thin Film Energy Density

In this section we are concerned with the particular case of an infinitely extending thin film, as depicted in Fig. 2.1. In the limit where the sole allowed magnetisation motion is

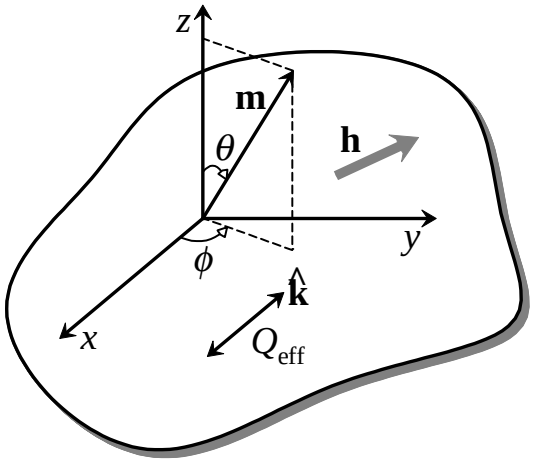

Figure 2.1: Thin film axes and angles.

rotation in unison, the energy density function takes on the simple form

$$\mathcal{E} = K_{\text{eff}} \sin^2\theta \sin^2\phi - \mu_0 M_s \sin\theta \,(H_x \cos\phi + H_y \sin\phi) + \frac{1}{2}\mu_0 M_s^2 \cos^2\theta \quad \text{(in SI)} \quad , \tag{2.1}$$

or, in reduced units (see Chap. 1)

$$w = \frac{Q_{\text{eff}}}{2} \sin^2\theta \sin^2\phi - \sin\theta \,(h_x \cos\phi + h_y \sin\phi) + \frac{1}{2}\cos^2\theta \quad , \tag{2.2}$$

where h_x and h_y are the components of the external magnetic field $\mathbf{h}$[(a)], here restricted to the thin film plane. The first term $(Q_{\text{eff}}/2)m_y^2$, if alone, defines the y axis as the hard magnetisation axis provided Q_{eff} be positive. It may contain contributions from both crystalline and growth-induced anisotropies. In such situations where the magnetisation lies in the thin film plane it defines an effective *uniaxial* anisotropy whose axis is shown in Fig. 2.1. The second term represents the interaction energy between the applied field, confined here to the xy plane, and the magnetisation which may point along any direction in space. It is minimum when $\mathbf{m}$ and $\mathbf{h}$ are parallel. The last term corresponds to the magnetostatic energy of a uniformly magnetised thin film of infinite lateral extension. The demagnetising field simply becomes $\mathbf{h}_d = (0, 0, -m_z)$. The combined effects of both the magnetostatic and anisotropy terms in Eq. (2.2) give rise to an orthorhombic anisotropy whose principal axes are $\hat{\mathbf{k}}$, $\hat{\mathbf{z}}$, and $\hat{\mathbf{k}} \times \hat{\mathbf{z}}$. Lastly, since no spatial variations of magnetisation are allowed for, exchange contributions are nil. It is straightforward to show that in zero applied field the stable magnetisation direction is $\pm x$.

[(a)] When no danger of confusion exists, $\mathbf{h}$ will be used to represent the *applied* magnetic field.

Magnetisation motion is described by the LLG equation (see Sect. 1.2.3)

$$\frac{d\mathbf{m}}{d\tau} = -\left(\mathbf{m}\times\mathbf{h}_{\text{eff}}\right) + \alpha\left(\mathbf{m}\times\frac{d\mathbf{m}}{d\tau}\right) \quad , \tag{2.3}$$

which will now be rewritten in the local frame ($\hat{\mathbf{e}}_\rho$, $\hat{\mathbf{e}}_\theta$, and $\hat{\mathbf{e}}_\phi$) defined in Fig. 1.2. Due to the constraint on the modulus of magnetisation ($m_\rho \equiv 1$), the following transformation holds valid

$$d\mathbf{m} = d\theta\;\hat{\mathbf{e}}_\theta + \sin\theta d\phi\;\hat{\mathbf{e}}_\phi \quad . \tag{2.4}$$

In agreement with previous definitions, and in reduced units, the polar and azimuthal components of the effective field are given by

$$h_\theta = -\frac{\partial w}{\partial\theta} \quad \text{and} \quad h_\phi = -\frac{1}{\sin\theta}\frac{\partial w}{\partial\phi} \quad , \tag{2.5}$$

respectively. Carrying out the vector products in the LLG equation yields

$$\begin{aligned}
\mathbf{m}\times\mathbf{h}_{\text{eff}} &= \left[\begin{array}{l} m_\rho = 1 \\ m_\theta = 0 \\ m_\phi = 0 \end{array}\right] \times \left[\begin{array}{l} h_\rho \\ h_\theta \\ h_\phi \end{array}\right] = \left[\begin{array}{l} 0 \\ -h_\phi \\ +h_\theta \end{array}\right] \quad , \\
\mathbf{m}\times\frac{d\mathbf{m}}{d\tau} &= \left[\begin{array}{l} m_\rho = 1 \\ m_\theta = 0 \\ m_\phi = 0 \end{array}\right] \times \left[\begin{array}{l} 0 \\ d\theta/d\tau \\ \sin\theta\,(d\phi/d\tau) \end{array}\right] = \left[\begin{array}{l} 0 \\ -\sin\theta\,(d\phi/d\tau) \\ +d\theta/d\tau \end{array}\right] \quad .
\end{aligned} \tag{2.6}$$

Therefore one may write

$$\frac{d\theta}{d\tau}\;\hat{\mathbf{e}}_\theta + \sin\theta\frac{d\phi}{d\tau}\;\hat{\mathbf{e}}_\phi = +h_\phi\;\hat{\mathbf{e}}_\theta - h_\theta\;\hat{\mathbf{e}}_\phi + \alpha\left(-\sin\theta\frac{d\phi}{d\tau}\;\hat{\mathbf{e}}_\theta + \frac{d\theta}{d\tau}\;\hat{\mathbf{e}}_\phi\right) \quad , \tag{2.7}$$

which transforms into the pair of equations

$$\begin{aligned}
\frac{d\theta}{d\tau} &= +h_\phi - \alpha\sin\theta\frac{d\phi}{d\tau} \quad , \\
\frac{d\phi}{d\tau} &= \frac{1}{\sin\theta}\left(-h_\theta + \alpha\frac{d\theta}{d\tau}\right) \quad .
\end{aligned} \tag{2.8}$$

In the absence of damping, precessional motion is seen to derive directly from the crossed actions of h_ϕ on θ and h_θ on ϕ, respectively. Similarly to the LLG equation in cartesian coordinates, the equation above transforms straightforwardly into

$$\begin{aligned}
\left(1+\alpha^2\right)\frac{d\theta}{d\tau} &= \alpha h_\theta + h_\phi = -\alpha\frac{\partial w}{\partial\theta} - \frac{1}{\sin\theta}\frac{\partial w}{\partial\phi} \quad , \\
\left(1+\alpha^2\right)\frac{d\phi}{d\tau} &= \frac{1}{\sin\theta}\left(-h_\theta + \alpha h_\phi\right) = \frac{1}{\sin\theta}\frac{\partial w}{\partial\theta} - \frac{\alpha}{\sin^2\theta}\frac{\partial w}{\partial\phi} \quad .
\end{aligned} \tag{2.9}$$

The set of equations above may be preferred to Eq. (1.50) since θ and ϕ are independent variables automatically satisfying $\|\mathbf{m}\| \equiv 1$, as long as the magnetisation trajectory bypasses the poles of the unit sphere.

For the sake of overall text legibility all numerical procedures developed in this work, be it in the framework of the present chapter or the following, are discussed in App. A. This choice allows not only for a more comprehensive reading of the physics developed in this work but also provides the numerically inclined reader with a concise and self-contained discussion on numerical procedures.

2.2 Classical Stoner-Wohlfarth Astroid

Let us first proceed with the analysis of the static equilibrium magnetisation directions. Under the action of an applied field restricted to the thin film plane, and since the magnetostatic contribution always acts as an energy penalty for any out-of-plane magnetisation orientation, static equilibrium directions necessarily belong to the film plane. Using the coordinate system of Fig. 2.1, the energy density function at static equilibrium can now be written as

$$w = \frac{Q_{\text{eff}}}{2} \sin^2 \phi - h_x \cos \phi - h_y \sin \phi \quad , \tag{2.10}$$

where ϕ now simply is the angle between the easy axis and $\mathbf{m}$. A system described by the energy function above is mathematically equivalent to the original Stoner-Wohlfarth model [27] of magnetisation rotation for single domain magnetic particles.

Equilibrium orientations of $\mathbf{m}$ correspond to minima of w and can be found from the equation

$$\frac{\partial w}{\partial \phi} = 0 \quad . \tag{2.11}$$

The stability of minima of w, as found using the equation above, are linked with the sign of the second derivative of w with respect to the angle ϕ. A stable magnetisation direction requires $\partial^2 w / \partial \phi^2$ to be positive. It becomes metastable when the second derivative of w with respect to ϕ changes sign. Therefore, the reversal/non-reversal boundary curve is to satisfy the additional condition

$$\frac{\partial^2 w}{\partial \phi^2} = 0 \quad . \tag{2.12}$$

Using Eq. (2.10) the first derivative of w with respect to ϕ can be written as

$$\frac{1}{\sin\phi\cos\phi}\frac{\partial w}{\partial \phi} = Q_{\text{eff}} + \frac{h_x}{\cos\phi} - \frac{h_y}{\sin\phi} \quad . \tag{2.13}$$

Differentiating the equation above allows one to write a relation involving the second derivative, namely

$$\frac{\partial}{\partial \phi}\left(\frac{1}{\sin\phi\cos\phi}\right)\frac{\partial w}{\partial \phi} + \frac{1}{\sin\phi\cos\phi}\frac{\partial^2 w}{\partial \phi^2} = -\frac{h_x\sin\phi}{\cos^2\phi} - \frac{h_y\cos\phi}{\sin^2\phi} \quad . \tag{2.14}$$

Equation (2.11) is tantamount to the equality

$$\frac{h_y}{\sin\phi} - \frac{h_x}{\cos\phi} = Q_{\text{eff}} \quad , \tag{2.15}$$

while Eq. (2.12) allows to write

$$\frac{h_x}{\cos^3\phi} + \frac{h_y}{\sin^3\phi} = 0 \quad . \tag{2.16}$$

Thus, on the boundary separating reversal and non-reversal regions (I and II, respectively, in Fig. 2.2) the two equations above are satisfied. They can be solved for h_x and h_y yielding

$$h_x = -Q_{\text{eff}}\cos^3\phi \quad \text{and} \quad h_y = Q_{\text{eff}}\sin^3\phi \quad . \tag{2.17}$$

The equation above is just a parametric representation of an astroid in the $h_x h_y$ plane described by the equation

$$h_x^{2/3} + h_y^{2/3} = Q_{\text{eff}}^{2/3} \quad . \tag{2.18}$$

This astroid curve is sketched in Fig. 2.2.

The astroid curve defines not only the stability limit for equilibrium magnetisation directions, but also helps to determine graphically the possible metastable magnetisation directions for any given field **h** and thus the magnetisation curve. Indeed, magnetisation directions can be found by using the following geometric construction, first proposed by Slonczewski [28], and usually known as the astroid method. For a given external magnetic field **h**, as represented in Fig. 2.2, the directions of **m** satisfying Eqs. (2.10) and (2.11) are parallel to those tangent lines to the astroid which pass through the point **h**. It can be shown that equilibrium orientations of **m** correspond to the tangent line with the smallest slope, i.e. those with the smallest angle relative to the easy axis. The magnetisation reversal properties of micron-sized thin films have indeed been fruitfully characterised through the use of such techniques (e.g. [29]). In conclusion, it should be mentioned

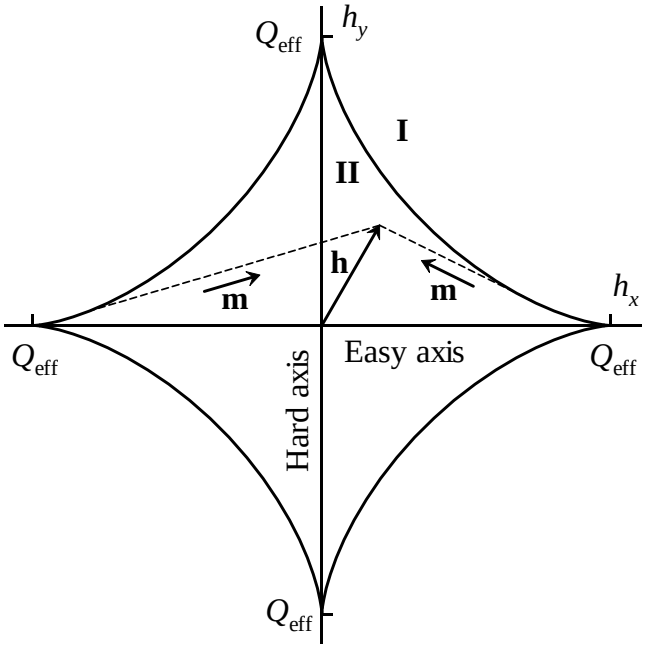

Figure 2.2: Astroid curve and equilibrium orientations of magnetisation.

that these geometrical constructions are amenable to extension to more general situations. Non-trivial solutions to this problem have been proposed by Thiaville in two articles taking into account two-dimensional non-uniaxial anisotropy contributions [30] and the full three-dimensional problem [31], respectively.

2.3 Dynamical Astroid and Ballistic Trajectories

As stated in Sect. 2.1, the full description of magnetisation dynamics within a thin film under the macrospin approximation requires solving the LLG equation with an energy function as defined by Eq. (2.2). Kikuchi was the first to address the question of the dynamics of magnetisation switching [5]. In his widely cited article of 1956, he presented an analytical solution to the particular case of an uniformly magnetised sphere reacting to an external magnetic field forming an angle of about 180° with the initial magnetisation direction. His analysis focused on the determination of the critical value of the damping constant corresponding to the minimum magnetisation switching time. For this particular situation the balance between precession and damping is struck for $\alpha = 1$, a result, however, by no means general. For values of the damping constant greater than 1 the magnetisation simply moves slower towards the applied magnetic field, while for $\alpha < 1$ the

magnetisation moves faster but swiftly rotates around **h** thus increasing the net switching time (see also [32]). Here ends, unfortunately, the scope of a full analytical treatment of macrospin dynamics.

A first numerical analysis of the macrospin switching behaviour, adhering strictly to the original Stoner-Wohlfarth model, was provided by He and coworkers [33]. For external applied fields restricted to a plane containing the easy magnetisation axis, switching was found to occur below the static astroid curve for precessional dominated systems. As expected the static reversal/non-reversal boundary was found to be approached when considering large values of the damping constant. In addition, above the so-determined dynamical astroid, the possibility of multiple switching events can be demonstrated when considering either step like [34] or fixed (finite duration) field pulses [35]. The area above the dynamical astroid curve (the equivalent of region I in Fig. 2.2) then becomes an intricate pattern of switching and non-switching zones, especially marked in the limit of short pulse lengths.

The results to be presented in the following aim at extending the above mentioned works including now, however, an *active* control over field pulse duration. In short this statement means that, given a field orientation and amplitude, the pulse length is a function of the magnetisation trajectory in space. Consider a field pulse with a non-zero y component and an initial magnetisation direction along $-x$. As soon as the field is applied, precession around the y field component forces the magnetisation to leave the film plane. Doing so, a strong demagnetising field builds up, which tends to bring the magnetisation back in the film plane and forces a precessional motion of the magnetisation vector around the z axis. When attempting magnetisation switching, this typical behaviour suggests the adoption of the following field termination strategy: the pulse length value will be set as the time necessary for the magnetisation trajectory to reach the film plane for the first time as shown in Fig. 2.3**a**. Ultimately one aims at defining the switching phase diagram *under such hypotheses* of field pulse cutoff control.

For simplicity field pulses are here considered to have zero rise and fall times. This means that we limit ourselves to situations where energy dissipation during the increase of the Zeeman energy (actually, an increase of its absolute value) may be neglected, i.e. we aim at fully exploiting the basic precessional nature of magnetisation motion. Three regions may be differentiated in the $h_x h_y$ plane, or at least close to the dynamical astroid

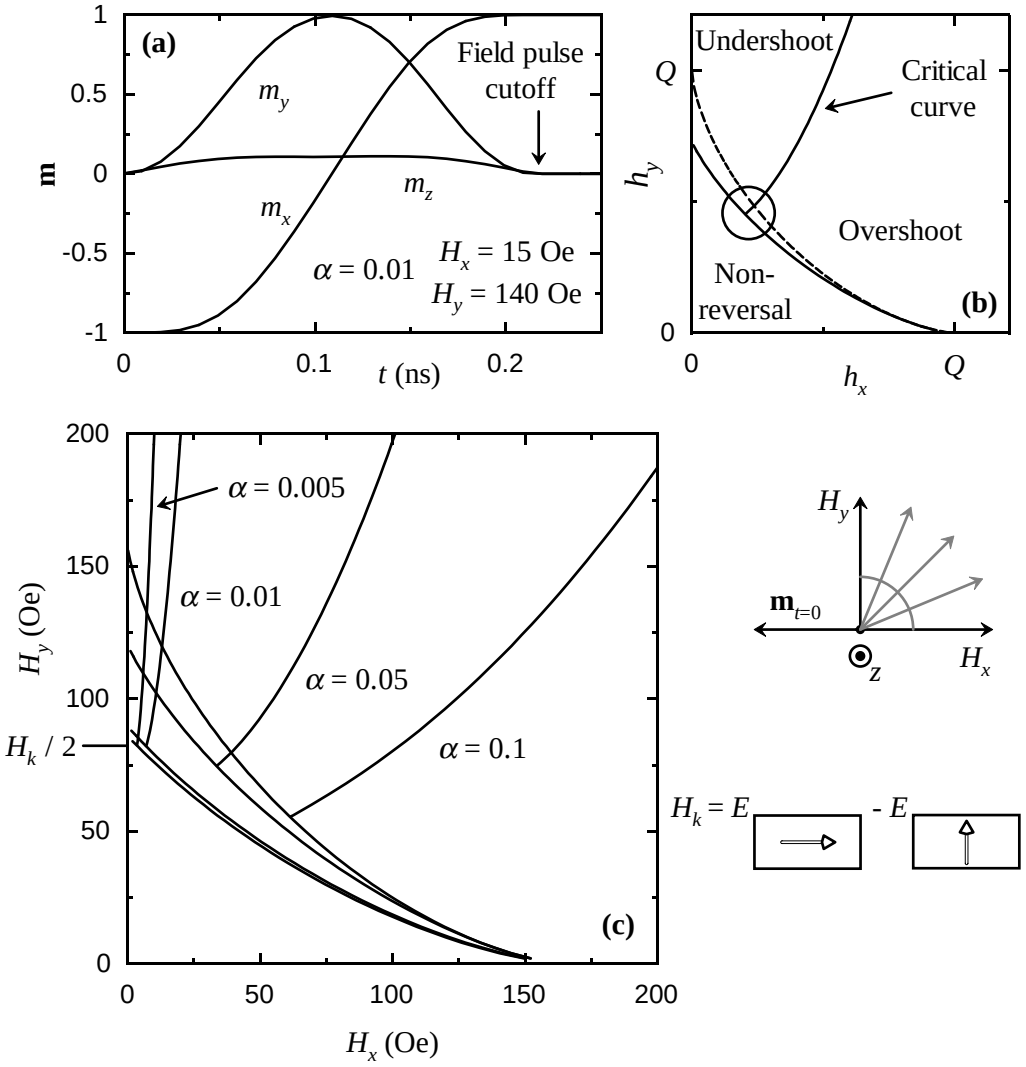

Figure 2.3: The dynamical astroid and critical switching curves. (**a**) Field pulse termination criterion. (**b**) Schematic switching phase diagram. (**c**) Computed dynamical reversal/non-reversal boundaries and critical lines as a function of damping in a Permalloy thin film with shape anisotropy ($H_k \approx 13.13$ kA/m = 165 Oe) corresponding to the energy barrier between fully aligned magnetisation distributions in a $500 \times 250 \times 5$ nm^3 element (right).

curve. Below the lower curve in Fig. 2.3**b**, reversal does not occur, whatever the length of the applied field pulse. The magnetisation reaches its new equilibrium position under field following a trajectory of the kind shown in Fig. 2.4**a**. Above the lower curve, reversal *may* occur, meaning that starting from the $-x$ direction, the stable magnetisation direction after field application becomes the $+x$ direction. The lower curves in Fig. 2.3**c** are therefore the dynamical equivalents to the first quadrant part of Stoner-Wohlfarth's astroid in the static regime. Noteworthy is the fact that the dynamical reversal/non-reversal boundary

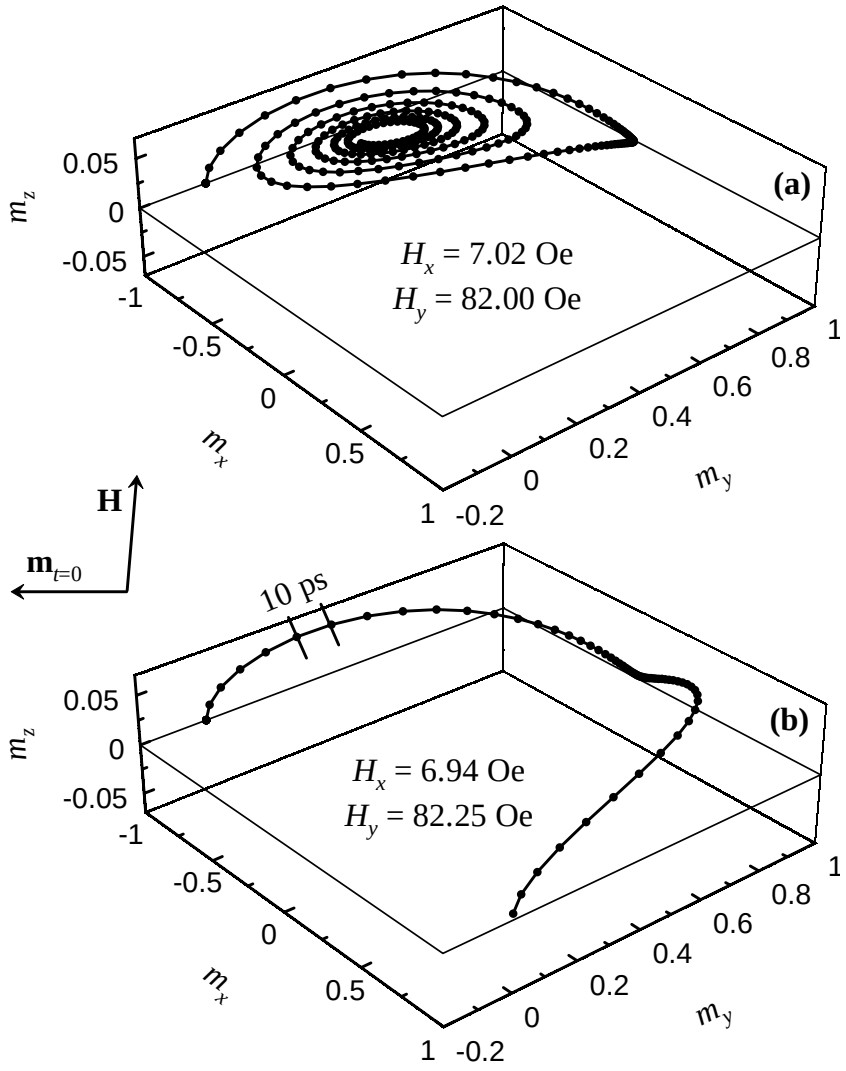

Figure 2.4: Macrospin trajectories connected with the switching phase diagram of Fig. 2.3**b** (encircled region) for $\alpha = 0.01$. (**a**) Non-switching (trajectory displayed up to $t = 2.5$ ns). (**b**) Switching displaying a ballistic trajectory.

curve always falls below the static astroid, except when $h_y = 0$, as has already been pointed out [33]. The lower the damping parameter, the wider the separation between the dynamical and static reversal/non-reversal boundaries. Merging between the dynamical reversal/non-reversal curve and the static astroid is, for the parameters used in Fig. 2.3, virtually achieved for $\alpha = 0.1$.

The region where switching takes place may itself be divided into two subregions, one where the magnetisation trajectory exhibits undershoot (Fig. 2.5**a**) and one where overshoot takes place (Fig. 2.5**c**). Between those two subregions of the phase diagram

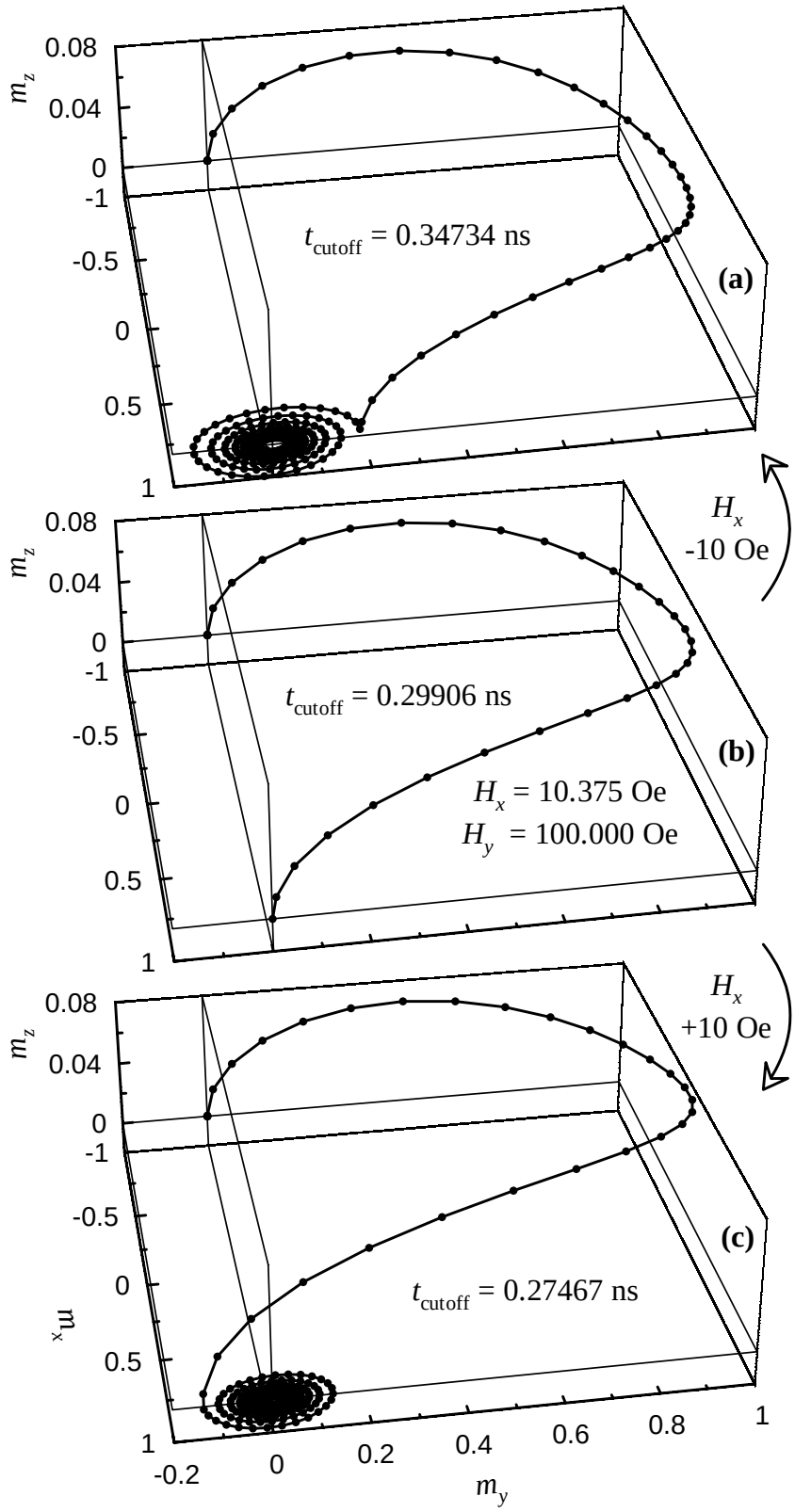

Figure 2.5: Macrospin trajectories connected with the switching phase diagram of Fig. 2.3**b** for $\alpha = 0.01$. (**a**) Switching with undershoot. (**b**) Switching displaying a ballistic trajectory. (**c**) Switching with overshoot

exists a critical line which corresponds to an exact ballistic trajectory, i.e. a trajectory characterised by the absence of ringing (Fig. 2.5**b**), stretching through all the region I in Fig. 2.2, which implies that a small region of undershoot/overshoot (switching) can always be found in such region. Indeed, since a macrospin has no inertia, if the applied field pulse is cutoff exactly when the magnetisation vector points along its stable equilibrium direction under no external field, magnetisation will forever remain static. In the limit of an applied field pointing solely in the y direction, the critical curve becomes that portion of the H_y axis above the dynamic reversal/non-reversal boundary satisfying $H_y > H_k/2$ in the zero damping ($\alpha = 0$) limit.

As already stated, switching can occur below the static reversal/non-reversal threshold, and this despite the energy barrier existing between energy minima. Displaying the macrospin trajectories on top of the energy landscape (restricted for simplicity to two quadrants) allows to visually grasp the nature of such phenomenon. Figure 2.6 displays three such graphics, corresponding to a ballistic switching event (Fig. 2.6**a**), to switching below the static astroid curve (Fig. 2.6**b**), and to the non-switching case (Fig. 2.6**c**) for a longitudinal field value of 16 Oe. Due to gyromagnetic effects (the out-of-plane initial magnetisation motion, especially), the magnetisation vector effectively gets around the energy pits eventually ending up in the switching quadrant. Focusing our attention on Fig. 2.6**a**, we immediately see that dynamical trajectories instead of following the steepest energy slope prefer to more closely follow "equienergy" lines. This is a direct consequence of the small damping parameter values used ($\alpha = 0.01$), giving preeminence to precessional motion.

In fact, as also seen in Fig. 2.5**b**, critical trajectories may intuitively be understood as a half precessional motion of magnetisation around the strongest component of the effective magnetic field acting on the system, i.e. the demagnetising field, directed along z, arising from out-of-plane components of magnetisation. This is all the more true as large applied field values are used, since they determine the amount of initial out-of-plane movement. In addition, since magnetisation motion immediately stops upon field termination, such trajectories also correspond to minimal switching times, considering a macrospin model. Figure 2.7**a** plots the switching time dependence along the critical curve corresponding to $\alpha = 0.01$ as a function of the applied magnetic field. A monotonically decrease can be immediately perceived as a function of increasing applied field magnitude. As stated above, ballistic trajectories can be heuristically understood as a half precession

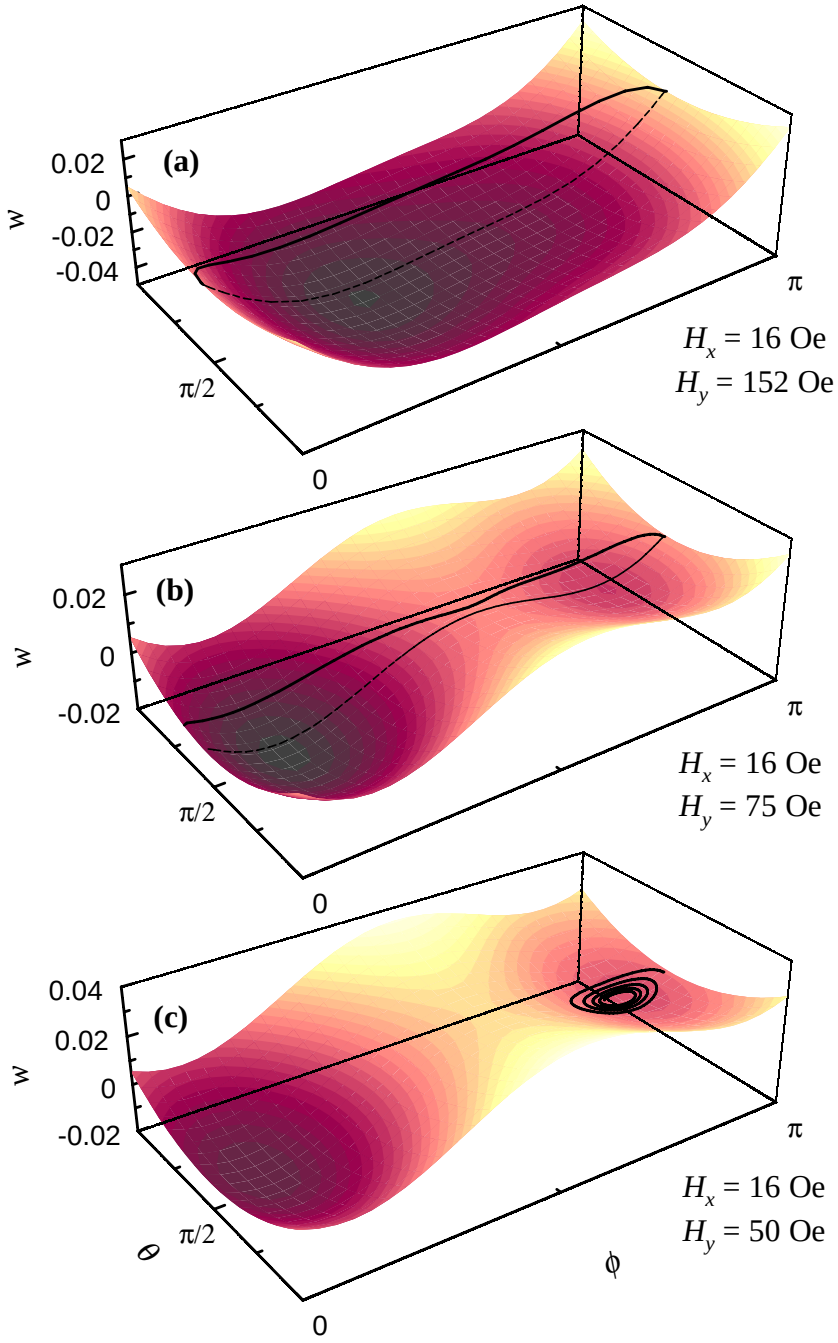

Figure 2.6: (Colour) Macrospin trajectories upon the energy surface landscape. **(a)** Ballistic switching (above the static astroid curve). **(b)** Switching below the static threshold. **(c)** Non-switching. The dotted lines stand for the only possible static trajectories (strictly in-plane).

motion of magnetisation around the demagnetising field axis always directed along z. If magnetisation motion was to be described solely be precession, i.e. disregarding damping effects, Eq. (1.15) should provide for a direct expression for the switching time when

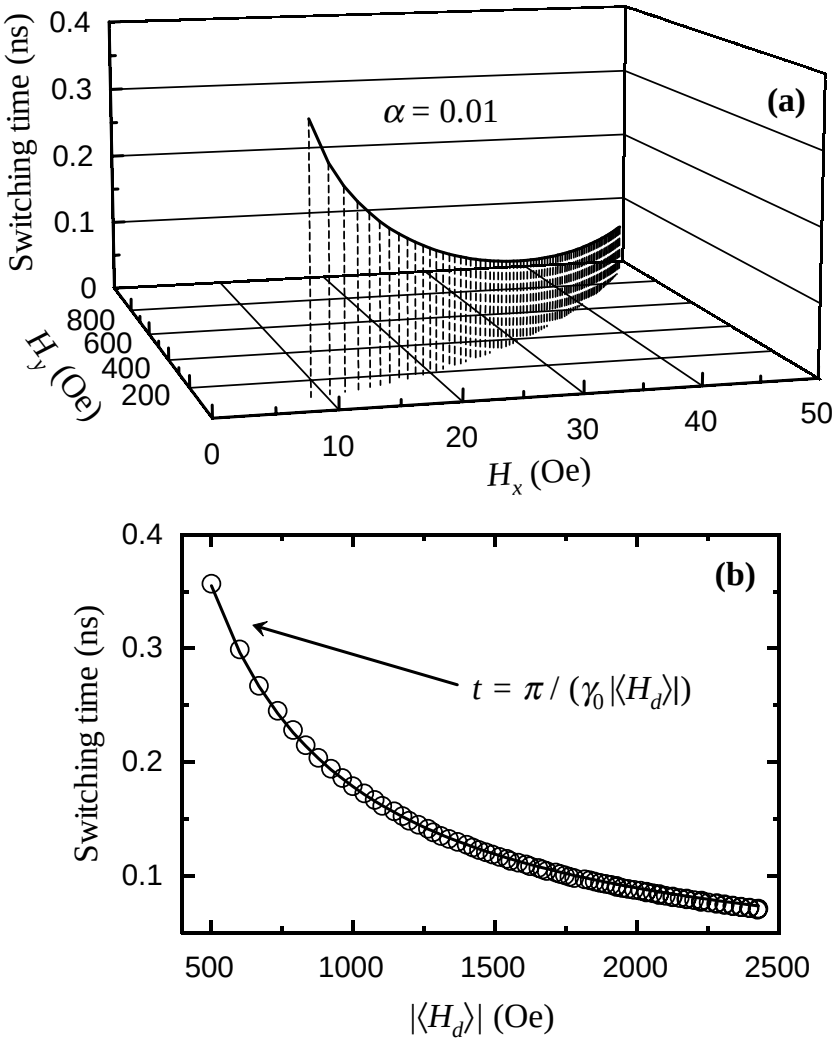

Figure 2.7: Magnetisation switching times. (**a**) Switching time value along the critical curve for $\alpha = 0.01$. Values where projected unto the $H_x H_y$ plane. (**b**) Switching time values as a function of the average demagnetising field during motion for the conditions of Fig. 2.7**a**. The line displayed corresponds to the theoretical switching time associated with a half-precession around $\langle H_d \rangle$. No fitting parameters are involved.

replacing ω by π/t. Since, during motion, the magnitude of the demagnetising field varies, its average value was considered. The numerical results are presented in Fig. 2.7**b** along with the theoretical line predicted by Eq. (1.15). The agreement between the theoretical prediction and the numerical data is excellent, emphasising the intimate relation between critical ballistic trajectories and half-precession cycles.

Intuitively, the existence or not of similar ballistic trajectories for the average value of a magnetisation distribution, together with other phenomena, may give some indication

on the dynamical coherence of a given magnetisation distribution. Indeed, the possibility of magnetisation oscillation (ringing) suppression has been experimentally found by field pulse tailoring in iron garnet films [36], a particular suitable material due to its low damping constants and large exchange lengths. This question will be briefly addressed again in Chap. 4.

2.4 Asymptotic Solutions for Transverse Oscillations

As stated before, even for the seemingly extremely simple problem of coherent magnetisation motion in a soft magnetic thin film, there exists no fully analytical solution to the equation of magnetisation motion including damping. In the following, however, we shall seek for an asymptotic solution at times long after the onset of the field, in the case where the applied field has a sole component along the y direction. Because we look for an asymptotic solution, we are entitled to linearise Eq. (2.9) in the variables η and ζ, which represent deviations from the values of θ and ϕ at equilibrium under field, namely

$$\theta_{\mathrm{eq}} = \frac{\pi}{2} \quad \text{and} \quad \sin\left(\phi_{\mathrm{eq}}\right) = \frac{h_y}{Q_{\mathrm{eff}}} \quad . \tag{2.19}$$

Defining $\mathcal{T}$ as the operator $d/d\tau$ and $\theta = \theta_{\mathrm{eq}} + \eta$, $\phi = \phi_{\mathrm{eq}} + \zeta$ yields

$$\begin{aligned} \left[\left(1+\alpha^2\right)\mathcal{T} + \alpha\right]\eta + \left(Q_{\mathrm{eff}} - \frac{h_{\mathrm{y}}^2}{Q_{\mathrm{eff}}}\right)\zeta = 0 \quad , \\ -\eta + \left[\left(1+\alpha^2\right)\mathcal{T} + \alpha\left(Q_{\mathrm{eff}} - \frac{h_{\mathrm{y}}^2}{Q_{\mathrm{eff}}}\right)\right]\zeta = 0 \quad . \end{aligned} \tag{2.20}$$

Because the LLG equation has been linearised, the solution of the set of linear differential equations (2.20) may only apply long after the onset of the pulse. The general solution to Eq. (2.20) are time exponentials, namely $\eta, \zeta \propto \exp\left(p\tau\right)$. If one further assumes that $\alpha \ll 1$, as it would be the case for a Permalloy thin film, for instance, the characteristic equation reads

$$p^2 + \alpha p + Q_{\mathrm{eff}}\left[1 - \left(\frac{h_y}{Q_{\mathrm{eff}}}\right)^2\right] = 0 \quad . \tag{2.21}$$

Two regimes may thus be separated according to the sign of the quantity

$$\Delta = \alpha^2 - 4Q_{\mathrm{eff}}\left[1 - \left(\frac{h_y}{Q_{\mathrm{eff}}}\right)^2\right] \quad . \tag{2.22}$$

If Δ is positive, critical damping is expected to occur. This may only happen in a tiny field amplitude span close to the anisotropy field, namely

$$\left(\frac{h_y}{Q_{\mathrm{eff}}}\right)^2 > 1 - \frac{\alpha^2}{4Q_{\mathrm{eff}}} \quad . \tag{2.23}$$

In most practical cases, such a condition will not hold and damped oscillations of the macrospin around its equilibrium position will take place. The general solution reads

$$\eta, \zeta = C_{\eta,\zeta} e^{-t/t_0} \cos\left(2\pi \frac{t}{t_1} + \text{Phase}\right) \quad . \tag{2.24}$$

The characteristic times t_0 and t_1 are the oscillations decay time and period, respectively. They are equal to

$$t_0 = \frac{2}{\alpha \gamma_0 M_s} \quad \text{and} \quad t_1 = \frac{4\pi}{\gamma_0 M_s} \frac{1}{\sqrt{4\left(Q_{\text{eff}} - h_y^2/Q_{\text{eff}}\right) - \alpha^2}} \quad . \tag{2.25}$$

In order to provide typical figures and a direct comparison with simulations results to be shown in the following, let us consider below the case of small Permalloy platelets characterised by a 2:1 aspect ratio where shape anisotropy may be shown to correspond globally to an anisotropy field of $\approx 13.13\,\text{kA/m}$ (165 Oe) (see Fig. 2.3). When submitted to an external field of amplitude $\approx 9.95\,\text{kA/m}$ (125 Oe) directed along the short axis of the platelet, such a system, if behaving as a macrospin, would, long after the onset of the applied field, exhibit oscillations of the magnetisation direction with a period of $\approx 0.425\,\text{ns}$ and a decay time of $\approx 1.13\,\text{ns}$, assuming $\alpha = 0.01$ and $\mu_0 M_s \approx 1\,\text{T}$ ($M_s = 800\,\text{emu/cc}$). These figures indicate the kind of temporal resolution to be achieved in a time resolved magnetometry experiment. It obviously proves highly demanding. In closing this section, let us mention that the problem of small magnitude oscillations in the macrospin regime can be treated on a more general footing [4].

Summary

Macrospin dynamics in thin films has been addressed in some detail, starting by a straightforward correlation with static properties. The switching phase diagram is determined under the condition of field pulse cutoff control. Due to the initial out-of-plane magnetisation motion, the field pulse cutoff criterion has been chosen as the time when m_z becomes nil for the first time. Under such assumptions, a critical ballistic magnetisation trajectory, corresponding to the minimum possible switching time, can be uniquely determined. The presentation of the magnetisation trajectories on top of the energy surface landscape allows for a clear understanding of the possibility of magnetisation switching under the static reversal/non-reversal boundary of the classical Stoner-Wolfarth's model. Although

full analytical solutions to the thin film macrospin dynamics cannot be derived, asymptotic expressions for magnetisation oscillations have been provided, allowing for a simple and direct comparison with full-scale simulation results.

Chapter 3

Platelets Dynamics: Asymptotic Solutions

This (transitional) chapter intends to bridge the gap between the macrospin approximation presented in the previous chapter and full-scale micromagnetic simulations of the dynamics of magnetisation switching in soft magnetic platelets. For lateral dimensions above, though not too far off, the single domain limit, only a limited number of magnetisation distributions may be generated depending upon field application and, more generally, magnetic history. We refer below to such magnetic configurations as states. Their energy hierarchy will be established, putting a special emphasis on the link between thickness values and the stabilisation of high remanence states. Of particular interest is the possibility of obtaining *almost* single domain magnetisation distributions, which Chappert termed Coherent Spin Structures (see [37]), and the possibility of mimicking, or inducing, coherent magnetisation rotation processes. The particular case of transverse oscillations is presented along with a comparison with the asymptotic analytical description of long time oscillations described in the previous chapter. Finally, a brief discussion is provided for the limits of applicability of asymptotic analytical solutions.

3.1 Equilibrium States: Rectangles with a 2:1 Aspect Ratio

When focusing on the magnetisation switching processes in elements of reduced lateral dimensions, one needs first to examine the initial (remanent) magnetisation distributions themselves, for much of the switching characteristics are conditioned by their properties. Of particular importance is the drawing of a neat boundary between high and low rema-

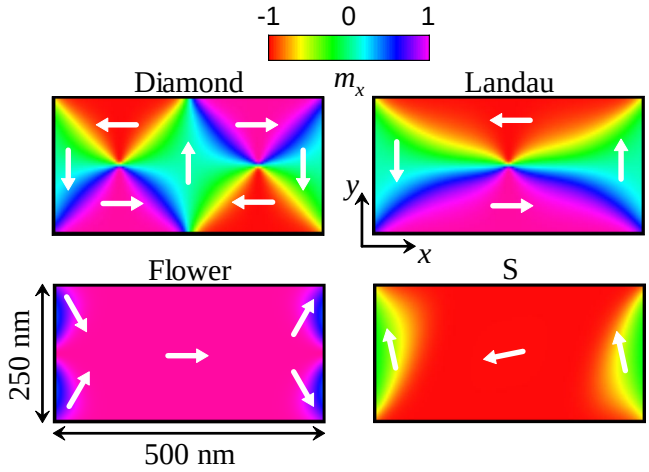

Figure 3.1: (Colour) Remanent magnetisation states for rectangular Permalloy platelets of dimensions $500 \times 250 \times 5$ nm^3. The colour code maps the x magnetisation component and the superposed arrows indicate the basic features of the magnetisation distributions.

nence states. Following on these lines, the need arises to establish the dimensional requirements under which these high remanence structures become stable (or at least marginally metastable). In connection with the proposals of the Micromagnetic Modelling Activity Group (μMAG) [38], dealing with standard problems in (static) micromagnetism, Rave and Hubert presented an extended analysis of remanent magnetisation states in rectangular Permalloy platelets [39]. Their discussion was centred on equilibrium magnetisation configurations of 2:1 aspect ratio thin film elements (20 nm thick) with lateral dimensions ranging from 0.1 μm to 2 μm. Only below the micrometre lateral range do Coherent Spin Structures become the lowest energy states. Thus is established the justification for focusing on the dynamics of magnetisation in submicron-sized lateral dimensioned elements.

Although there is no need to repeat here the details of Rave and Hubert's work, it is nevertheless useful to complement it by considering the thickness dependence of four commonly discussed magnetisation states in rectangular platelets of lateral dimensions 500×250 nm^2 (as depicted in Fig. 3.1), and to stress a couple of important features. The total energy values associated with these four magnetisation distributions are presented in Table 3.1 as a function of thickness. Below some threshold thickness value, high remanence magnetisation distributions become energetically more favourable than low remanence (flux closure) ones, as evidenced in Fig. 3.2**a** when considering the Landau and S states. Reasons for such behaviour appear clear when plotting the values of the individual energy terms (here only exchange and magnetostatic) versus thickness (Fig. 3.2**b**). Although

	3 nm	5 nm	10 nm
Diamond	0.016911	0.018400	0.020862
Landau	0.011381	0.013248	**0.016949**
Flower	0.008678	0.012881	0.021812
S	**0.007347**	**0.010998**	0.019096

Table 3.1: Reduced total energy values for the four remanent states displayed in Fig. 3.1, and for different thickness values. Bold figures indicate, for each thickness value, the lowest energy state.

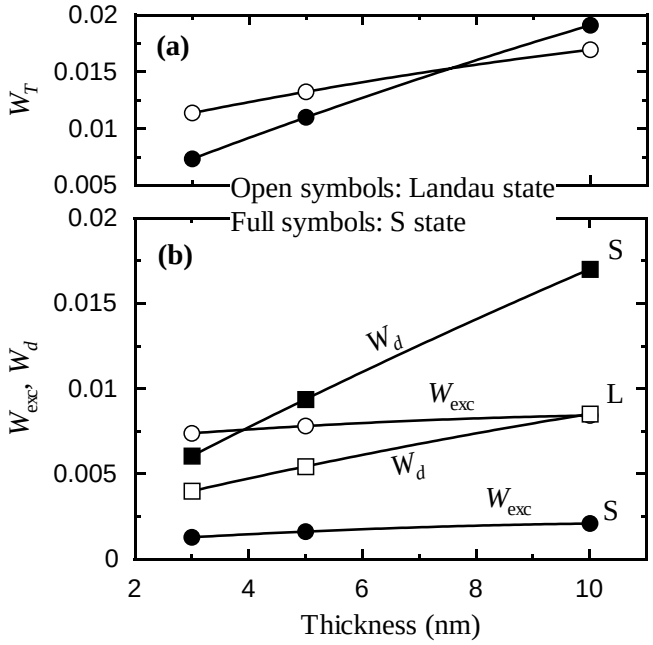

Figure 3.2: Energy versus thickness dependence for the Landau and S states. **(a)** Total energy. **(b)** Exchange and magnetostatic contributions as a function of thickness.

exchange energy values scale much at the same rate as a function of thickness (closure domain patterns having larger values than high remanence distributions), the increase in demagnetising energy for larger thickness values is much more noticeable in the S state. This reflects the additional energy penalty associated with the thickness scaling of volume magnetostatic contributions. Flux closure patterns, being mostly divergence-free, are essentially sensitive to the sole thickness scaling of surface demagnetising terms. *Mostly divergence-free* refers here to the existence of residual dipolar type charges within Néel walls.

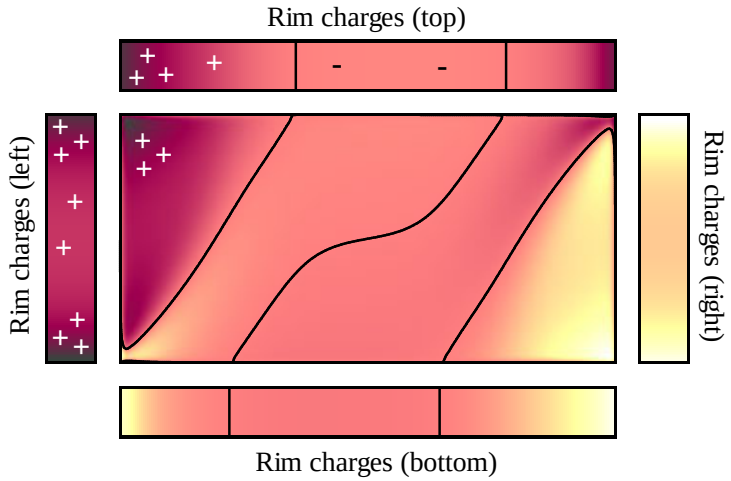

Figure 3.3: (Colour) Volume and rim magnetic charges for an S state. Lines inside the plots correspond to zero charge values.

For the given lateral dimensions, and within the thickness range from 3 to 5 nanometres, the S state remains the lowest possible energy state, even in comparison with highly symmetrical (strictly in-plane) magnetisation configurations such as the Flower state. This may be accounted for by the intrinsic features of the S state. As schematically indicated by the superimposed arrows in Fig. 3.1, the y magnetisation component at the element's core is opposite to that of the end domains. The volume charges so created (see Fig. 3.3) effectively compensate (although partially) both the rim charges and the energy penalty arising from a more non-uniform overall magnetisation distribution. In addition, volume charges are smeared throughout the platelet.

The initialisation of an S state may conveniently be achieved under the action of an external magnetic field directed at, for example, 45° with respect to the element's long axis. The direction of the edge closure domains will be aligned with the transverse direction of the applied field. In addition, this angular value displays a large margin of tolerance, ranging from a misorientation of a few degrees from the element's long axis to an almost perpendicular transverse direction. The intrinsic features of the S state (high transverse susceptibility and both end domain alignment and stability) will play a decisive role in the basic mechanisms of stable magnetisation switching, as will be seen in the following (Chap. 4). Actually, the S state, with its parallel alignment of closure domains, constitutes a most suitable magnetisation distribution in connection with the operating requirements of cross-point Magnetic Random Access Memory (MRAM) architectures. Throughout,

the S state will be consistently used as the initial magnetisation configuration.

Another commonly considered high remanence magnetisation state, the C state, was purposefully not considered. This magnetisation distribution is in all respects similar to an S state, differing only by the fact that the two closure domains are now oppositely oriented. For 2:1 aspect ratio rectangular Permalloy elements its energy value (and for the lateral dimensions considered above also the reversal field value) is virtually that of the S state [39]. In both cases, the quasi-static reversal process displays the same degree of complexity.

3.2 Transverse Susceptibility: Simulations

As seen above, the leading factor in choosing a particular magnetisation state was its degree of spatial magnetisation coherence, the aim being clearly directed at the use of high remanence magnetisation distributions in attempting to reproduce the main features of a macrospin type switching in submicron soft magnetic elements (whose dimensions are typically those in Fig. 3.1). From this standpoint, we present in this section a detailed analysis of a simulated experiment aimed at establishing the degree of macrospin behaviour in the dynamical response of a 0.5×0.25 μm^2 Permalloy platelet submitted to a sole y-directed field (along the element's short axis) in an initial S state. A damping parameter value of 0.01 will be supposed to hold true in the following when considering Permalloy elements.

The time evolution of the average values of magnetisation components is shown in Fig. 3.4 for a magnetic field amplitude value of 125 Oe. Focusing on the average x magnetisation component $\langle m_x \rangle$, seems to behave essentially as a damped sine type oscillation. On the other hand, $\langle m_y \rangle$ clearly does not follows such a behaviour. Reasons for this appear clear when looking at Fig. 3.5 which exhibits the magnetisation distributions corresponding to successive maxima (right) and minima (left) of $\langle m_x \rangle$ as a function of increasing time. Clear deviations from a rotation in unison are apparent when looking at the simulation snapshots. The main cause for such a behaviour is the pole avoidance principle which prevents the magnetisation from rotating freely close to the platelet rim. It may be said that the system oscillates between an S state where the majority of magnetisation is aligned along the long axis (left column) and a second S state where magnetisation is predominantly aligned along the short axis (right column in Fig. 3.5). This is the main cause

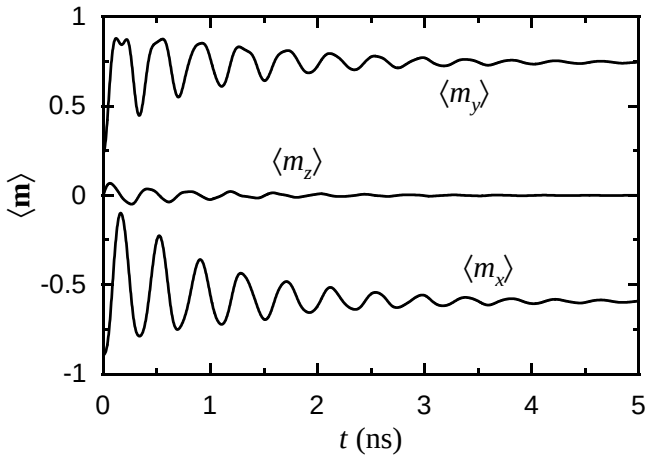

Figure 3.4: Time evolution of the average values of magnetisation components in a Permalloy platelet (0.5×0.25 μm^2) in an initial S state, submitted to a step like constant transverse applied magnetic field of amplitude 125 Oe.

for the slight deviation from a perfect damped sine type oscillation versus time. Actually, evoking the pole avoidance principle is slightly misleading because the lowering of the rim charge density is compensated by the appearance of volume charges. In other words, charges prefer to smear out in order to decrease the magnetostatic energy, as already seen before.

Further insight into the macrospin behaviour of micromagnetic systems may be gained by taking a closer look at its energy damping characteristics. In Chap. 1 a concise expression for the total energy dissipation rate of a micromagnetic system was derived which depends only on intrinsic material parameters and the actual magnetisation motion. Such equation can be immediately rewritten (in reduced units) in terms of the damping parameter, yielding

$$\alpha_{\rm dyn} = -\frac{d}{d\tau}\left(\int_\Omega w\, d\mathbf{r}\right) \Big/ \int_\Omega \left(\frac{\partial \mathbf{m}}{\partial \tau}\right)^2 d\mathbf{r} \quad . \tag{3.1}$$

During a dynamic micromagnetic calculation the recalculated value of the damping parameter $\alpha_{\rm dyn}$ can therefore be monitored and compared with the imposed damping value α. The importance of this (new) control feature in asserting the internal coherence of dynamical micromagnetic calculations will be amply discussed in the App. A. We are here interested in considering the macrospin equivalent of Eq. (3.1), i.e. the expression obtained if the magnetic system was indeed rotating in unison as a *single* magnetic vector

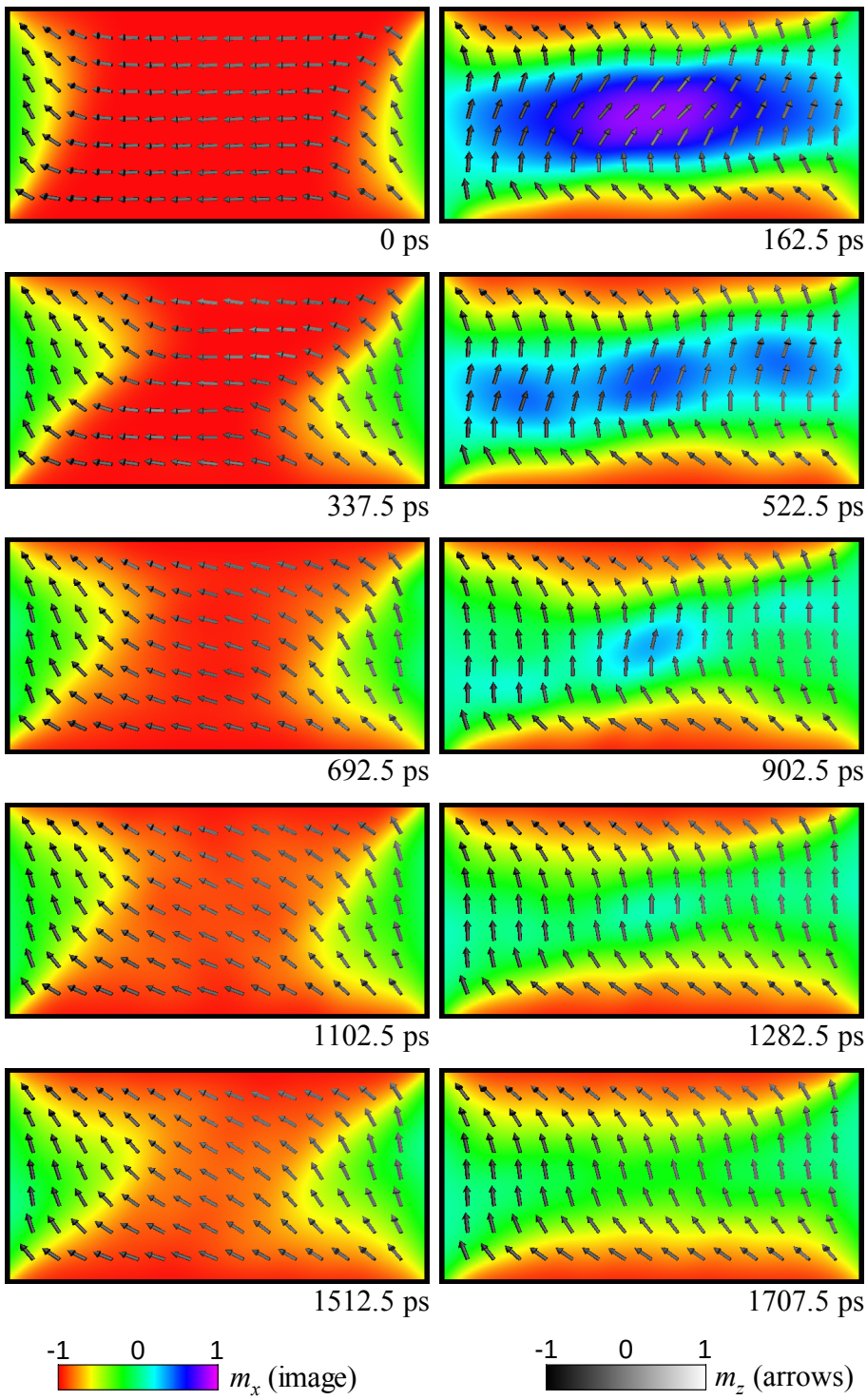

Figure 3.5: (Colour) Magnetisation distributions versus time. Left (right) column correspond to the successive minima (maxima) of $\langle m_x \rangle$ in Fig. 3.4. The picture at the top left represents the magnetisation distribution of the S state at rest.

would do. Equation (3.1) straightforwardly transforms into

$$\alpha_{\mathrm{MS}} = -\frac{d\langle w\rangle}{d\tau} \Bigg/ \left(\frac{d\langle \mathbf{m}\rangle}{d\tau}\right)^2 \quad . \tag{3.2}$$

The results obtained for the transverse oscillations experiment in Fig. 3.4 are given in Fig. 3.6 for the first 2.5 ns. The average magnetisation components are presented in Figs. 3.6**a** through 3.6**c** and the recalculated α values are given in Fig. 3.6**e**. An immediate comment concerns the nature of the strong peaks in α_{MS} which correspond roughly to stationary values of the average in-plane magnetisation components and to zeros of $\langle m_z\rangle$. Since a *true* macro spin system does evolve in time in accordance with the imposed value of the damping parameter (here 0.01), the aforementioned peaks must necessarily stand for a measure of the loss of magnetisation coherence, i.e. they indicate the time windows where the system, as a whole, can no longer be regarded as a macrospin[(a)]. To support this statement we present in Fig. 3.7 a set of magnetisation snapshots covering an oscillation period of $\langle m_x\rangle$. Indeed, when comparing the given time values with the data in Fig. 3.6, extrema of $\langle m_x\rangle$ are seen to be in a one-to-one correlation with α_{MS} peaks and correspond to such magnetisation patterns which more clearly deviate from a uniform distribution. In between (e.g. the shaded area in Fig. 3.6) magnetisation distributions do match those of almost perfectly aligned structures along the element's main diagonal (right side images in Fig. 3.7), and the values of α_{MS} approach that of α (or for that matter α_{dyn}) as explicitly presented in Fig. 3.6**e** using a highly zoomed y scale. It should be emphasised that even in such time windows the values of α_{MS} are persistently larger than those of α_{dyn} (which, as anticipated, remain at a constant value of 0.01).

The difference between α_{dyn} and α_{MS} stands therefore for a quantitative measure of the degree of coherency of a micromagnetic system (or the lack of it). Since every experimental measurement of α is bound to actually represent α_{MS} the principle above can be immediately transposed into the realm of experimental measurements, as any deviations from an overall macrospin behaviour is bound to produce different values of the damping parameter α_{MS}. Indeed, the values of the damping parameter determined as a function of the longitudinal bias field in large Permalloy stripes are easily interpreted in terms of spatial nonuniform magnetisation distribution [15]. Allowing for non-uniform magnetisation distributions in micromagnetic simulations immediately leads back to the correct values

[(a)] The peaks in α_{MS} must not be understood as a result of poor numerical procedures, as clearly demonstrated in App. A.

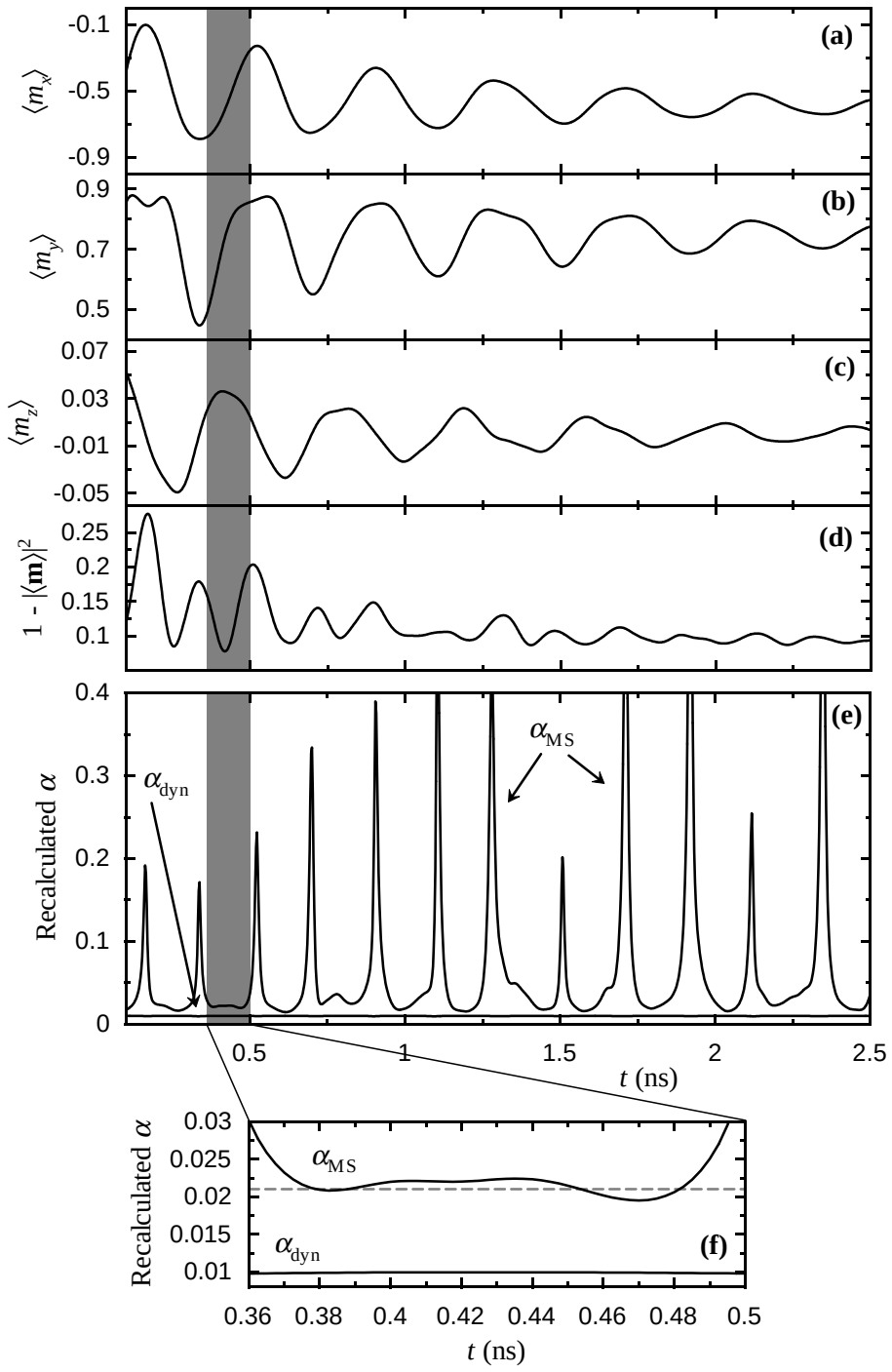

Figure 3.6: Recalculated α values for the simulation in Fig. 3.4. **(a)**–**(c)** Average x, y, and z magnetisation components, respectively. **(d)** Deviation of the norm of the average magnetisation vector. **(e)** Recalculated α values as a function of time according to Eqs. (3.1) and (3.2). **(f)** Zoomed time windows displaying the comparison between the smallest attainable values of α_{MS} and the featureless curve of α_{dyn}.

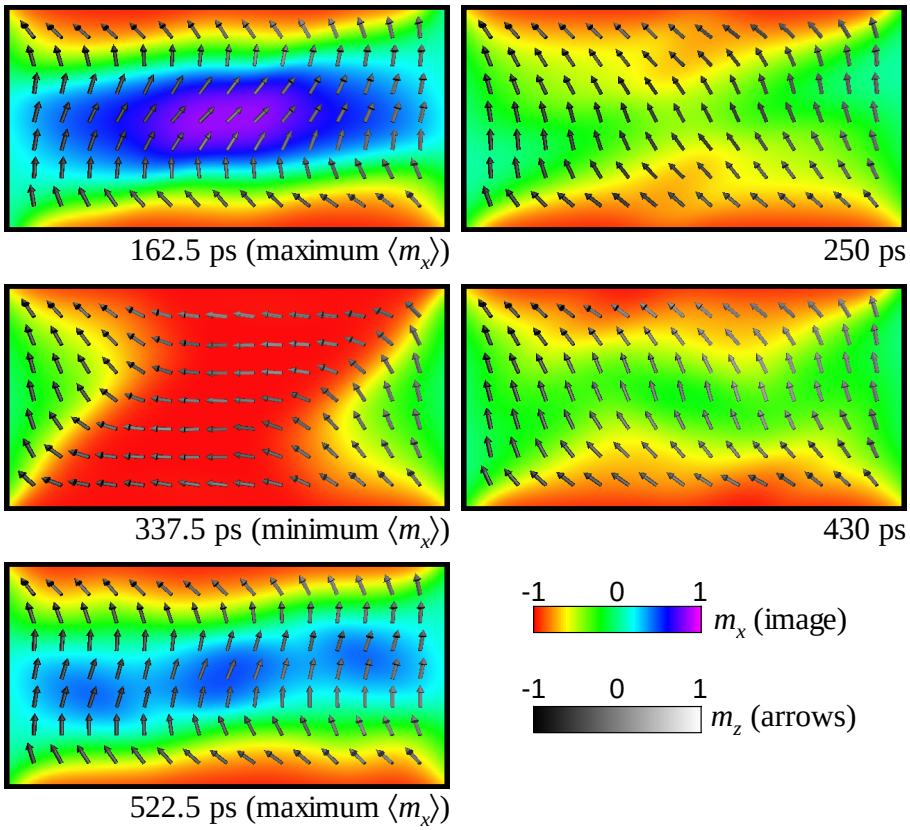

Figure 3.7: (Colour) Magnetisation snapshots corresponding to one oscillation period of Fig. 3.6. Right side images were taken at intermediate times between successive extrema of $\langle m_x \rangle$.

of the damping parameter [40].

Comparison between micromagnetic simulations results and fittings obtained from experimental data can therefore provide clear indications on the degree of non-macrospin behaviour of the experimental system under study. Future high resolution (both spatial and temporal) data should help clarify this point in the near future [16].

It proves nevertheless worthwhile to compare the predictions of the macrospin model with the oscillation period and decay time of $\langle m_x \rangle$ at times beyond, say, a few nanoseconds. In this way, full use can be made of the asymptotic solution for transverse oscillations derived in Sect. 2.4 for close-to-equilibrium magnetisation oscillations in low damping materials. The result is shown in Fig. 3.8**a**. Fitting the data displayed with Eq. (2.25) leads to values of the decay time and oscillation period equal to $t_0 = 1.245$ ns and $t_1 = 0.415$ ns, respectively, in fair agreement with expectations (1.130 ns and 0.425 ns, respectively). The inset displays the fitted function along with the experimental data for times smaller than 1

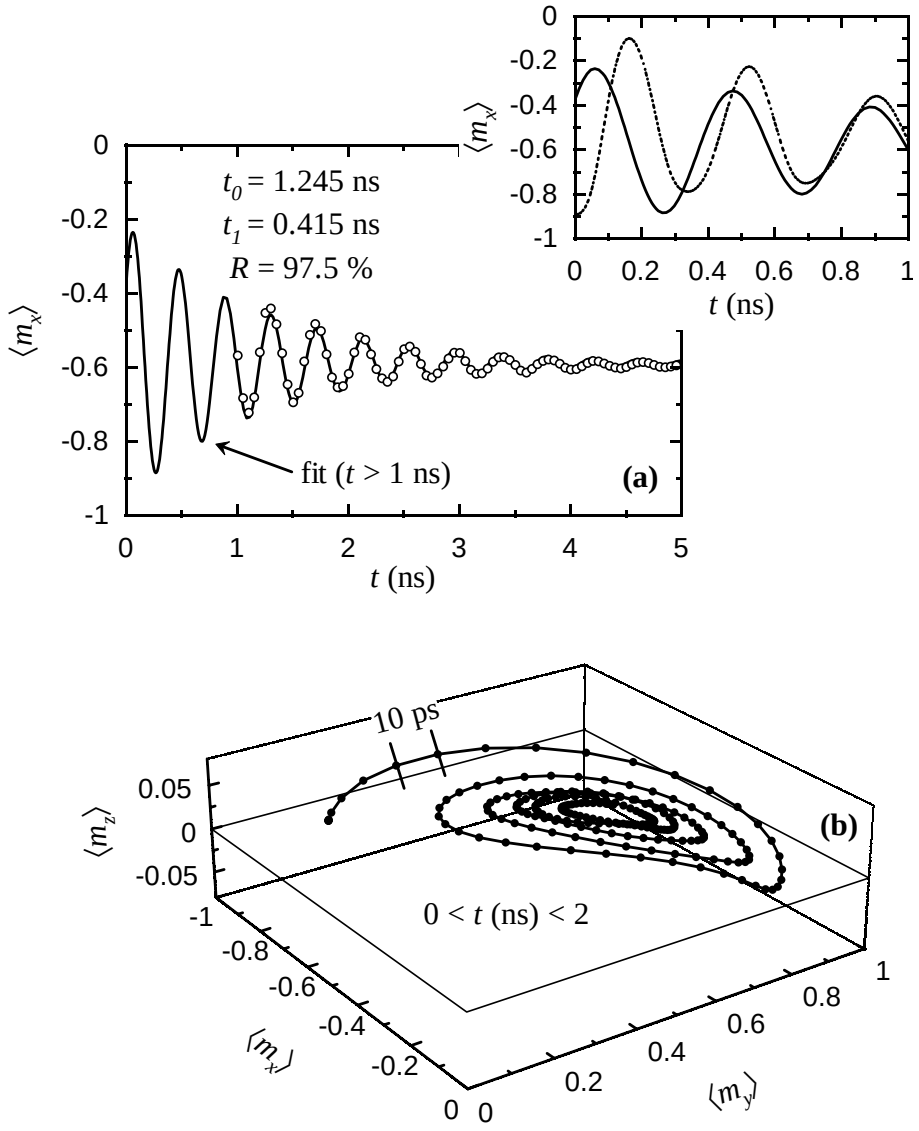

Figure 3.8: Analytical comparison of transverse oscillations experiment. **(a)** Fit of the $\langle m_x \rangle$ oscillations at times long after field pulse application (> 1 ns). The enlarged inset provides a comparison between the fitting curve and the experimental data at times smaller than 1 nanosecond distinctly revealing that the asymptotic expressions clearly do not apply for time windows other than close-to-equilibrium time values. The dotted line corresponds to the symbols in the larger image. **(b)** Spatial trajectory of the average magnetisation vector.

nanosecond, clearly evidencing the non-applicability (as should be expected) of the asymptotic oscillation expression within that time window. It should be mentioned that fitting the average magnetisation curves, or for that matter the experimentally measured data, with a single spin LLG equation using different time windows may lead to the determination of quite different intrinsic parameters, such as α. This should, of course, not be taken

as an indication that a sole intrinsic damping parameter (α in the LLG equation) is unable to represent actual measured data, as has been already demonstrated by Sandler and coworkers [40], since (among other factors) the precession frequency in complex micromagnetic structures is bound to change over time due to its proportionality with $\mathbf{h}_{\text{eff}}$ [41]. The trajectory described by the average magnetisation vector is equally well behaved, at times long after pulse application, as shown in Fig. 3.8**b**. Unsurprisingly, a macrospin type behaviour is anticipated to be best respected (in high remanence magnetisation states) when the oscillations amplitude vanish away, i.e. in situations where magnetisation coherence is best approached. Recent experimental data support this statement. In magnetisation ringing suppression experiments [36, 42] and magnetisation dynamic response to both step-like [42] and pulsed [41] magnetic fields the essential macro spin nature of magnetisation motion can be asserted in magnetic elements of considerable lateral extension (100 μm to 1 mm).

As will be seen in the following chapter, when attempting magnetisation switching, this simple picture of an almost macro spin behaviour must be revised. The differences are now between the average magnetisation on the element and the details of small scale magnetisation directions and the degree of coherence between neighbouring regions. The main goal, however, still remains the development of suitable strategies leading to the quasi-coherent magnetisation rotation during switching.

Summary

The magnetisation state energy hierarchy was established for a 500×250 nm^2 *Permalloy platelet as a function of thickness (3, 5, and* 10 nm*) and for the S, Flower, Landau, and Diamond configurations. For the* 5 nm *thickness value considered throughout this work, high remanence states become the most stable energy configurations. Field initialisation considerations, on top of a strong transverse field susceptibility, lead us to the unconditional adoption of the S state. Transverse susceptibility numerical experiments were performed. These provide for both a clear determination of the characteristic time scales in the dynamics of such platelets, but also allows for a straightforward evaluation of the degree of macrospin like behaviour of non-uniform magnetisation distributions through a macrospin equivalent as expressed via self-consistency of the damping parameter.*

Chapter 4

Platelets Dynamics: Micromagnetic Simulations

As suggested by the discussion in the previous chapter, the simple picture of an overall macrospin behaviour should be revised when considering magnetisation switching[(a)] in submicron-sized elements. Due attention must now be paid to the details of small-scale magnetisation distributions (in particular the degree of coherence between neighbouring regions) possibly hidden underneath smooth average magnetisation curves. Additionally, the quest for subnanosecond switching times necessarily binds one's attention to the role of precession-driven motion. The aim is now the development of suitable switching strategies possibly mimicking the macrospin ballistic trajectories (see Sect. 2.3) and leading to a quasi-coherent magnetisation rotation. Such are also some of the issues connected with MRAM development, i.e. the achievement of fast, stable, and reversible state switching between non-flux closure, high remanence, magnetisation distributions. Fully exploiting the intrinsic design features of cross-point MRAM architectures [43], actually leads to a rethinking of the operating principles of bit writing through an optimised use of the two available orthogonal field pulses.

4.1 Classical Thinking: Easy Axis Field Switching

The first studies of magnetisation switching in patterned soft magnetic elements followed the approach commonly employed in most quasi-static reversal experiments, i.e. the sole

[(a)] Throughout this work, the term switching will be used when referring to the dynamics of magnetisation motion, as opposed to the word reversal (employed solely in quasi-statics).

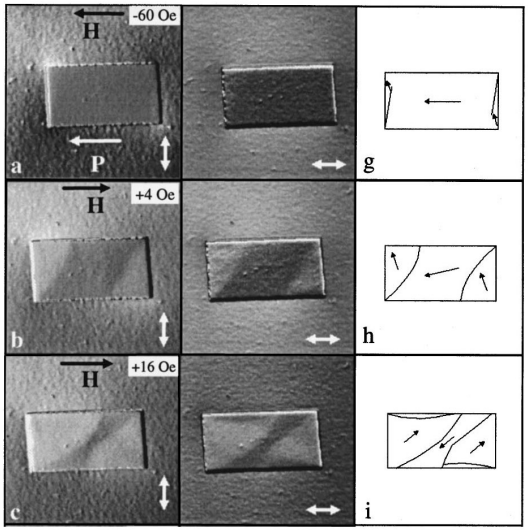

Figure 4.1: *Reprinted from J. Appl. Phys.* ***83****, 5321 (1998).* S state's quasi-static reversal properties induced by an easy axis oriented magnetic field. **a**–**c** Differential Phase Contrast (DPC) images of a 4×2 μm^2 element recorded at different applied fields. P denotes the pinning direction in the spin valve stack (see text) and the double headed arrows denote the direction of the induction mapped in each image. **g**–**i** Schematics of the magnetisation distributions as deduced from the images in **a**–**c** (note that the arrows within the closure domains have been misplaced in **h**).

use of a field pulse directed along the element's easy axis. In 4×2 μm^2 patterned spin valve elements, with an 8 nm thick Permalloy free layer, Chapman and coworkers reported on the details of the magnetisation reversal process set off by the action of an in-plane, easy axis oriented, magnetic field [44] (see Fig. 4.1). For the lateral dimensions indicated above, and after saturation under the action of a nominal x-directed field (Fig. 4.1**a**), their initial magnetisation distribution was an S state oriented along the element's longest edge. The sequence of Differential Phase Contrast (DPC) images above clearly reveals that magnetisation reversal takes place following the growth of the S state's end domains towards the centre of the platelet and their subsequent rotation in the direction of the applied field.

Consider next an equivalent switching experiment in a Permalloy submicron element, whose lateral dimensions are still those given in Fig. 3.1. The simulation results are displayed in Fig. 4.2 in terms of the average magnetisation components. Clearly, switching may be attained under the sole action of an x-directed field pulse, and this well within the first nanosecond time window. The sole presentation of the average values of magnetisa-

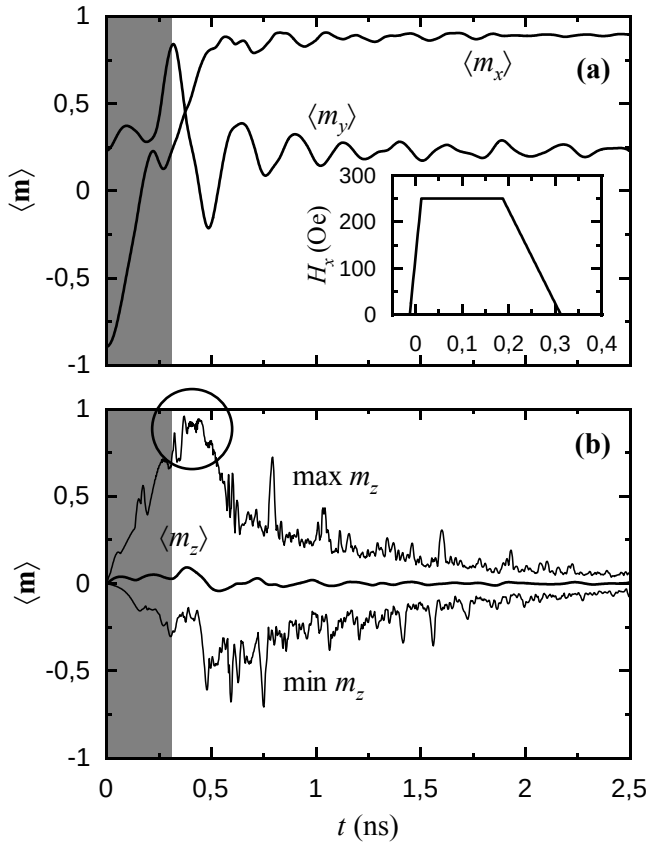

Figure 4.2: S state magnetisation switching under the sole action of an x-directed field pulse. The shaded areas delineate the time window where the field pulse is nonzero. **(a)** In-plane average magnetisation components. The inset displays the field pulse profile **(b)** Maximum, average, and minimum out-of-plane magnetisation values as a function of time.

tion components is, however, highly misleading, since their smooth behaviour conceals a rather complex picture at a local scale. Indeed, despite a rather featureless $\langle m_z \rangle$ curve, the maximum value of the out-of-plane magnetisation component grazes 1, indicating the near nucleation of micromagnetic structures such as vortices (Fig. 4.2**b**). For the data shown, the maximum out-of-plane angle ($\varphi = \pi - \theta$) inside the platelet corresponds to values as large as 72°. Since micromagnetic structures such as lines and vortices are known to have a considerable influence on magnetisation dynamics, as amply demonstrated in the study of magnetic bubbles [6], and raise its degree of complexity accordingly, their nucleation do pose serious problems when aiming at a fast and predictable switching mechanism (as already alluded to in Chapman's work). Additionally, from a strictly numerical viewpoint, the dynamics of such small magnetic structures represent a daunting challenge to micromagnetic simulations. A more thorough discussion of the topological questions raised

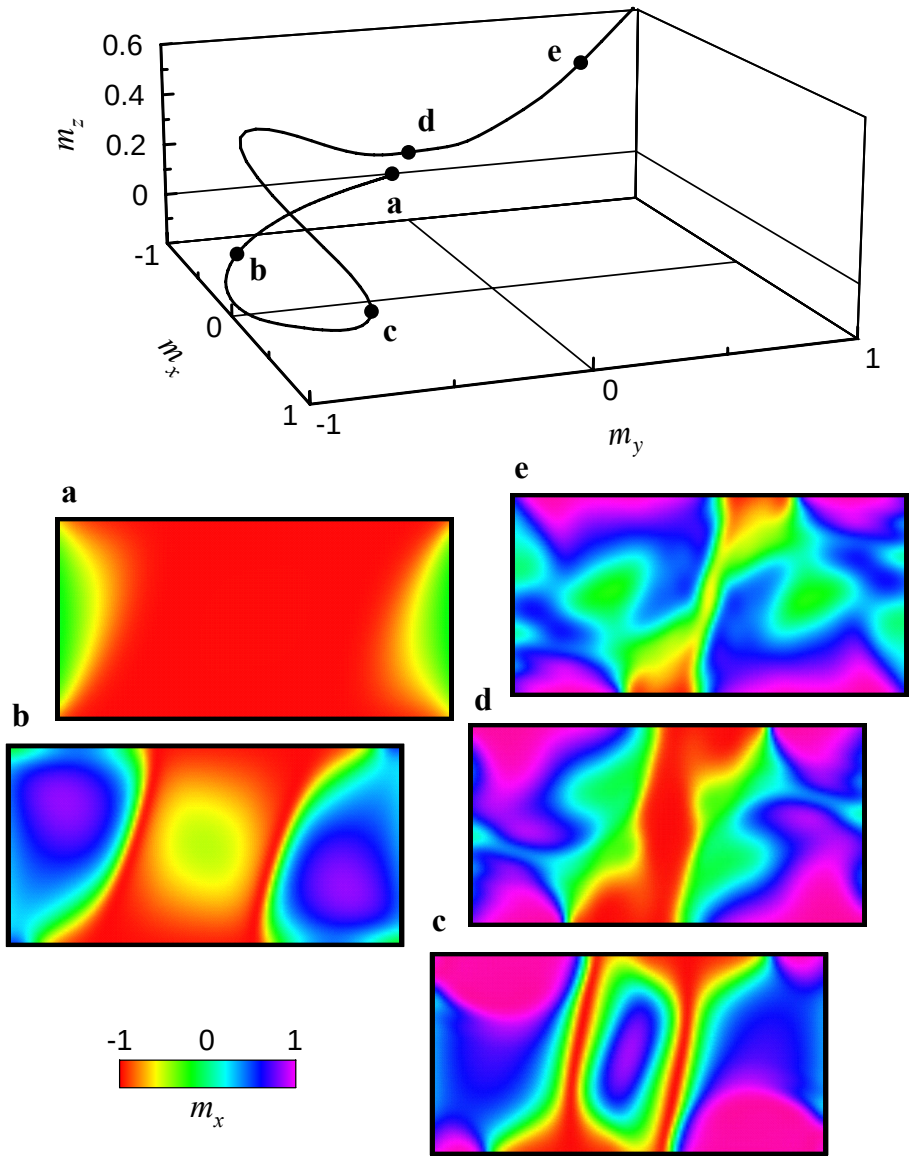

Figure 4.3: (Colour) Centre point magnetisation trajectory for the simulation in Fig. 4.2 and selected magnetisation distribution snapshots. The trajectory is displayed up to $t \approx 0.32$ ns, corresponding to the pulse cutoff time. Points **a**, **b**, **c**, **d**, and **e** correspond to times -0.05, 0.14, 0.21, 0.28, and 0.31 nanoseconds, respectively.

by strong "gyrotropic" effects on micromagnetic structures such as vortices, and their dependence on spatial meshing, will be made in App. A.

Further insights into the switching process taking place under the action of a sole easy axis field can be obtained by looking at the data presented in Fig. 4.3. Here, the trajectory of the central magnetisation vector is displayed from -0.05 to approximately 0.32 nanoseconds, along with several magnetisation snapshots collected at chosen times.

It can be seen that magnetisation movement starts, as in quasi-static experiments, by an expansion of the S state's edge closure domains, with a correspondent clockwise rotation inside the domains. Simultaneously, the magnetisation at the core of the platelet rotates *counterclockwise* giving rise to the formation of two 360° walls (snapshots **a** through **c**). This peculiar switching mechanism can be easily understood when taking a closer look at the magnetisation distribution of an S state. At the centre of the distribution, magnetisation tends to compensate charges, as already schematically indicated by the superposed arrows in Fig. 3.1, and is actually tilted towards the negative y values, whereas the end domains point along $+y$. This is a general feature of S states, even for lateral dimensions smaller than those used in this work, and originates from the existing balance between magnetostatic and exchange energies. The former stems from charges within the transition regions (walls) separating the core region of the platelet from its two closure domains as well as from boundary charges (see Fig. 3.3). The latter arises from the nonuniform magnetisation distribution. The aforementioned 360° walls eventually unwind at the cost of large magnetisation fluctuations (snapshots **d** and **e**) and will, at length, lead to a switched (mainly $+x$-oriented) S state.

Although the analysis above is in fair agreement with the broad features of the in-plane magnetisation components' time evolution presented in the work of Koch et al [14], in what proved to be the first combined numerical and experimental study of subnanosecond switching in micron-sized magnetic elements ($0.8 \times 1.6\ \mu\text{m}^2$), the fine prints of the actual magnetisation distributions are still the subject of debate. In particular, the details of the closure domains' rotation and expansion are in disagreement with our own data, theirs evidencing some sort of edge pinning effect of an unknown origin. Apart from exhaustive comparisons between different simulation data, let it be hoped that imaging techniques capable of both subnanosecond and tenths of nanometres, time and spatial resolutions, respectively, will provide some day experimental data precise enough to allow for a detailed comparison with simulation predictions. This, however, remains a genuine challenge (see, for instance, [16] and references therein).

The field pulse parameters used in the simulation above (Figs. 4.2 and 4.3) have been chosen in order to achieve the fastest possible switching without, nonetheless, nucleating strongly localised micromagnetic structures, for, as already stated, these may pose severe physical problems. In situations where the energy dissipation rate becomes the leading factor governing magnetisation motion, either through the use of a large damping param-

eter α or when field pulse values decay over a wide time window when compared with the characteristic precessional frequency of the system, the final magnetisation distribution may become trapped in a low remanence configuration, such as a Landau or a Diamond state (see Fig. 3.1), if micromagnetic structures have been nucleated during the switching process [45].

4.2 Precessional Switching

Both the existence of ballistic switching trajectories in the macrospin limit and the quasi-uniform nature of magnetisation configurations in submicron-sized elements allow to assume that we can indeed expect to induce magnetisation switching through a close-to-unison rotation. The S state's high transverse susceptibility (when the field pulse direction is aligned with the end domains' magnetisation) can be effectively used in triggering a clockwise magnetisation rotation in the core of the element (if $\langle m_x \rangle < 0$), as already exemplified in the transverse oscillations experiments of Sect. 3.2. In full analogy with the discussion on macrospin behaviour, a strong precessional motion will be unleashed by this y-directed field pulse (vide infra).

Currently considered cross-point MRAM architectures [43] rely on memory cell write selectivity through the combined action of two orthogonal field pulses arising from independently addressed current lines, above and below the active magnetic cell[(b)] (see Fig. 4.4). Fully exploiting this feature provides for an additional degree of control over the mechanisms of bit switching, as will be shown in Sect. 4.2.2. As a first approach, we look into the use of simultaneous (and square) field pulses, following the approach of Chap. 2. Such a discussion not only introduces the basic principles of precessional switching by quasi-coherent magnetisation rotation in patterned structures, but also allows to address the issue of ringing control after magnetisation switching.

4.2.1 Superimposed Field Pulses and Apparent Ringing Suppression

The existence of oscillation-free (ballistic) trajectories via pulse length tailoring has been clearly established in Chap. 2. Ringing control in finite size elements remains, however, more elusive. Bauer and coworkers [36] (see Fig. 4.5) have indeed produced experimental

[(b)] For simplicity, in simulations possibly connected with the operating principles of MRAM cells, current generated fields are assumed to be uniform inside the active magnetic layer.

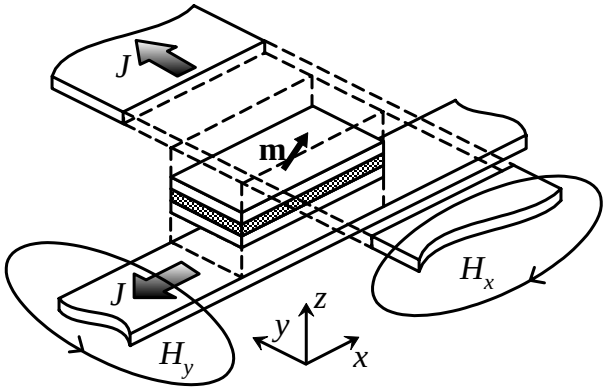

Figure 4.4: Schematic view of an MRAM cell in a cross-point architecture array. A single memory cell is addressed by the simultaneous use of both the word and bit current lines. The magnitude and time profile of the two orthogonal field pulses may then be independently controlled.

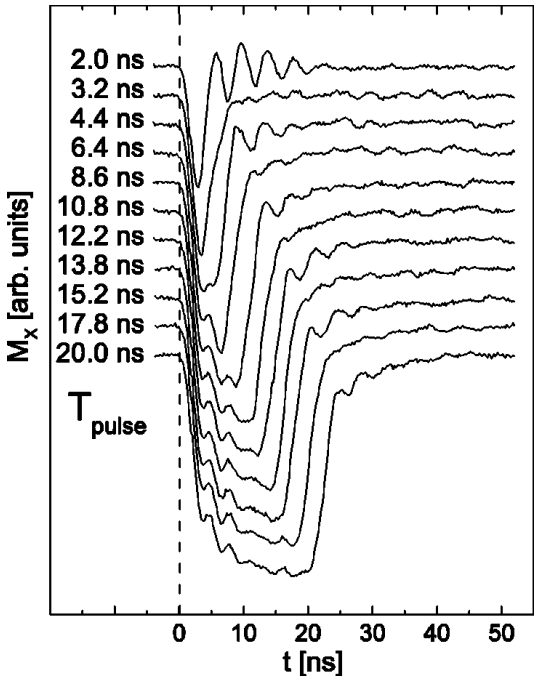

Figure 4.5: *Reprinted from Appl. Phys. Lett.* ***76****, 2758 (2000).* Ringing suppression in an iron garnet film through pulse length tailoring. Time evolution of the measured x magnetisation component (in-plane and aligned with the field direction) versus time for different pulse duration values, as indicated. The dotted vertical line indicates the pulse starting time.

evidence for *ringing suppression* in patterned elements. However, the size of those elements was large enough in order for the sensing light beam to probe an area where

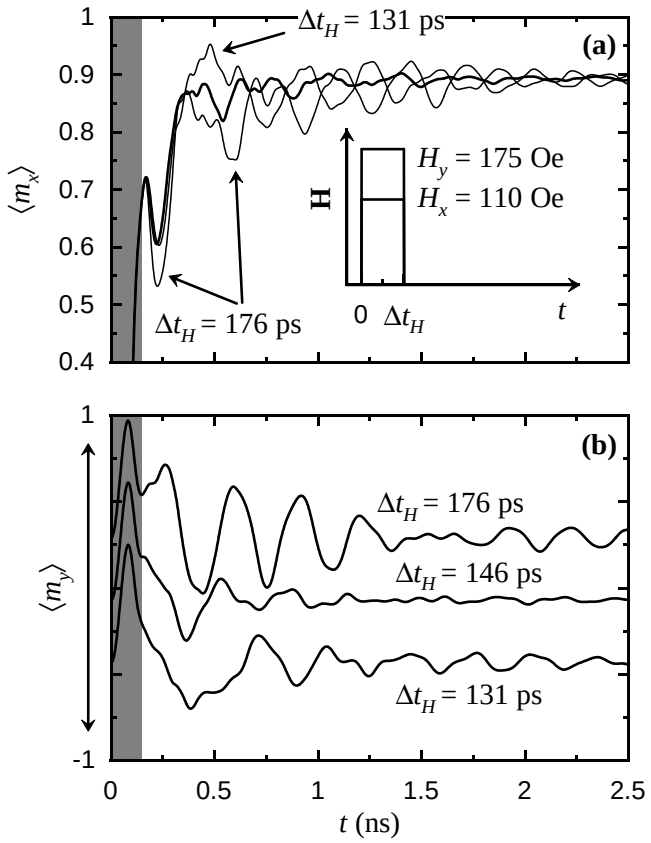

Figure 4.6: Ringing suppression after magnetisation switching by way of pulse length tailoring in 500×250 nm^2, 5 nm thick, Permalloy elements. **(a)** Average x magnetisation curves. The bold line corresponds to $\Delta t_H = 146$ ps. Beware of the expanded scale of $\langle m_x \rangle$. **(b)** Average y magnetisation curves (vertically shifted for increased visibility). The shaded area corresponds to the pulse duration for the *non-ringing* case: $\Delta t_H = 146$ ps.

magnetisation could rotate in close to unison motion. Moreover, these experiments do not involve switching, but a limited deviation from the equilibrium magnetisation position. Therefore, the development of a switching strategy leading to the definition of analogous (macrospin) critical ballistic magnetisation trajectories will now be attempted for the case of submicron size patterned elements.

Looking back at Fig. 2.3, it is clear that for each α value, the critical curve for ballistic switching spans an almost infinite range of field values. The larger the field, the shorter the switching time. Attempting to reproduce these results in the case of finite size elements is numerically out of reach. Therefore, only selected examples of typical behaviours may be provided. The choice was made to restrict field pulse magnitudes to values smaller than $\approx$ 200 Oe. A numerical equivalent to a ringing suppression experiment is displayed in Fig. 4.6.

A visible control over the post-switching motion can indeed be achieved by finely adjusting the field pulse duration. The large fluctuations displayed in the average y magnetisation curves as a function of pulse duration (Fig. 4.6**b**) lead, in the first approximation, to the conclusion of a switching experiment that turns out to be extremely sensitive to small variations in applied field characteristics. It is, however, utmost instructive to present the same data in a rather different manner. Collecting the combined information of the three curves corresponding to the different average magnetisation components, one can represent, within the unit sphere ($\langle m_x \rangle^2 + \langle m_y \rangle^2 + \langle m_z \rangle^2 \leq 1$), an average magnetisation trajectory. Two of such trajectories are plotted in Fig. 4.7: On top the large amplitude oscillation case and at the bottom the *suppressed* oscillations situation for the displayed field pulse amplitude values. During field application one is immediately struck by the evidence of an identical average trajectory. This is a direct consequence of the strong precessional motion of magnetisation around the demagnetising field axis, in full analogy with the results presented in Sect. 2.3 (compare with the macrospin trajectories in Fig. 2.5). Indeed, for both trajectories, the maximum $\langle m_z \rangle$ value is approximately equal to 0.1. The associated demagnetising field in Permalloy reaches therefore a value of $\approx$ 1000 Oe, which completely supersedes the effects of the transverse applied field value (here 175 Oe). After this initial out of the plane, fast, magnetisation rotation, roughly coinciding with the duration of the applied field pulse, differences appear. In the *controlled* ringing case (Fig. 4.7**a**), the *average* magnetisation trajectory rapidly arrives at its switched equilibrium value, displaying reduced oscillations. In contrast, the larger field pulse length simulation (Fig. 4.7**b**) reveals, after pulse cutoff, a significant oscillatory motion.

These large oscillations describe a strongly flattened ellipse, the characteristics of which are defined by the relative values of the demagnetising field (arising from the out-of-plane magnetisation component) and the shape anisotropy field associated with the equilibrium magnetisation distribution. They closely resemble those of the macrospin dynamical switching experiments for non-optimal field pulse values [4]. These large macrospin like fluctuations actually remain strongly confined in the yz plane, as shown in Fig. 4.7, and never approach the critical $\langle m_x \rangle$ value of zero. In the same respect the average m_y value remains always greater than zero, which is a general feature of an S to S state switching. From both numerical and experimental studies on infinite layer (in a single spin approximation) a high degree of control can be achieved in controlling ringing arising in the aftermath of magnetisation state switching. In the case of submicron laterally defined magnetic el-

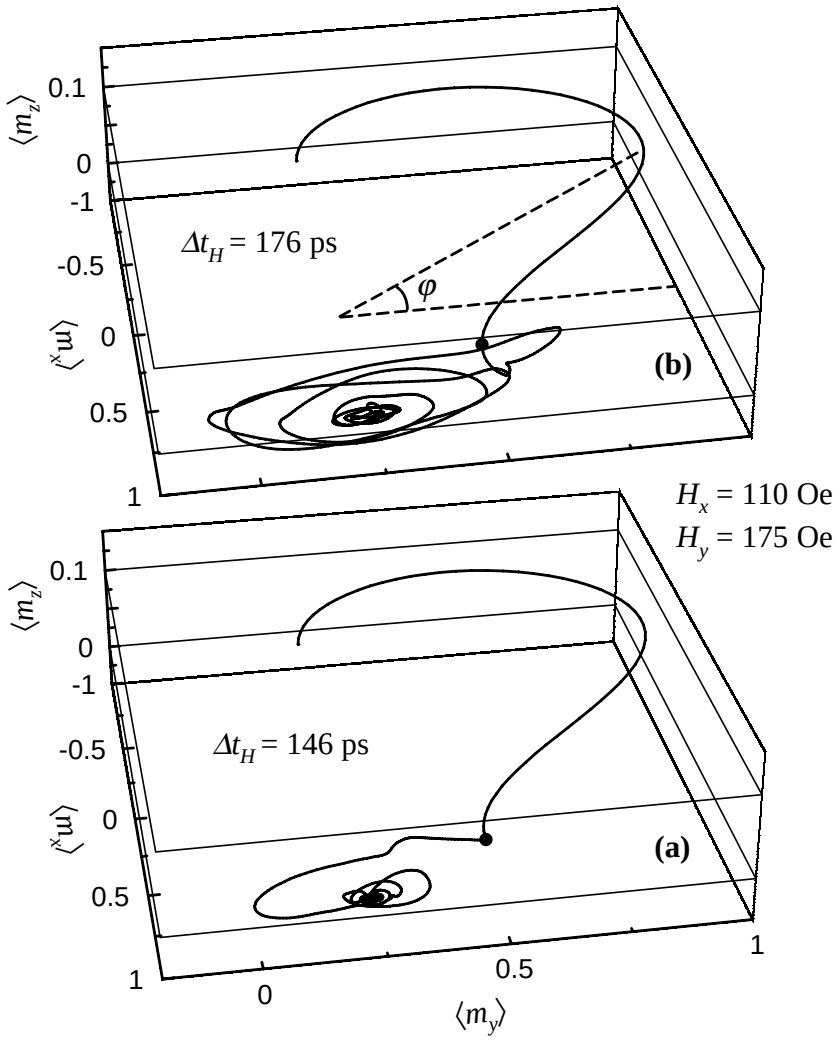

Figure 4.7: Magnetisation trajectories of the average magnetisation vector for two of the curves in Fig. 4.6. **(a)** Best ringing suppression conditions. The angle φ represented by the dashed lines indicates the maximum out of plane value of the average magnetisation vector (7.7°). **(b)** Strong oscillations condition. The oscillations observed in the average y component of magnetisation correspond to macrospin like oscillations of the element as a whole. The dots upon the magnetisation trajectories indicate the field cutoff instant.

ements, this ringing suppression should be viewed as simply *apparent*. In other words, if the reminiscence of a coherent macrospin type movement can be effectively controlled, local magnetisation fluctuations still prevail on a localised scale, as shown below.

One can summarise the overall magnetisation motion by looking at the sequence of diagrams in Fig. 4.8. Both state transitions are depicted, i.e. from a negative average x

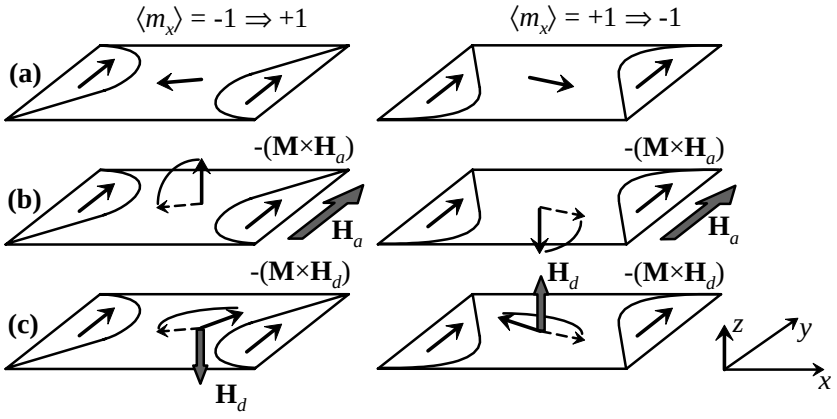

Figure 4.8: Diagram representing the precessional-driven fast switching mechanism. Both state transitions are depicted. **(a)** Initial magnetisation state. **(b)** Precession around the applied field forces magnetisation out of the platelet's plane therefore generating a z directed demagnetising field. **(c)** Strong precessional motion around $\mathbf{H}_d$ in the direction of the final magnetisation state. Note that in both cases the direction of the S state end domain remains unchanged and are effectively stabilised by the y-directed field pulse.

magnetisation component to a positive one (left side) and vice versa (right side). Both transitions originate from the action of the *same transverse field pulse*, which not only initiates magnetisation movement but helps, afterwards, in stabilising the end domains direction. Focusing on the left sequence, the process can be described as follows. Upon transverse field application, the magnetisation starts a precessional movement that forces it out of the film plane. Doing so, a strong demagnetising field develops in the opposite direction. Considering the saturation magnetisation value of Permalloy thin films, and taking into account the reduced thickness values used, one can see that the magnitude of such field will be far greater than that of the applied or shape anisotropy. The inner core region of the platelet will now continue its precessional movement, but now revolving around the demagnetising field, much as in the case of macrospin ballistic trajectories (see Sect. 2.3). Simple geometrical considerations reveal that magnetisation will now rotate towards positive x values: The larger the field, the faster the magnetisation swing. At this stage, and still focusing on the left sequence, the $+x$-directed field pulse actively participates in damping out residual magnetisation fluctuations and stabilises a mainly $+x$-oriented magnetisation state. If the whole process can justly be associated with precession, it is not so much the action of the applied pulse that allows for the attaintment of subnanosecond switching speeds but the fast rotation that ensues from a precession around

the demagnetising field, efficiently driving the magnetisation towards its new equilibrium direction. One condition needs, however, to be satisfied: The field pulse rise times must remain small versus the precessional period of the active (here demagnetising) field value.

Contrary to widespread assumptions, edge closure domains not only do not hinder the achievement of a quasi-coherent magnetisation rotation process but can be effectively used in stabilising the end state magnetisation distribution. Further details on the basic micromagnetic mechanisms of this process will be given next, in the framework of an optimised and still more controlled switching experiment.

4.2.2 Sequential Field Pulses

Given the basic principles of precessional driven magnetisation switching described above, a better degree of control can be expected to be gained by time-shifting the transverse and longitudinal field pulses. This procedure can be regarded as the dynamical equivalent of quasi-static magnetisation reversal experiments under the combined action of a constant transverse bias field and an axial field. It was, to the authors knowledge, first proposed by Miltat and coworkers at the 1999 *MRS Spring Meeting* [45] and at the 1999 edition of *Frontiers in Magnetism* [46]. The claims made of a more controlled switching process have been tentatively put to test afterwards, albeit in larger elements than those used in this work and considering fairly long (≈ 20 ns) field pulses [47]. Even if the experimental data bear no direct link with the precessional driven switching mechanism described in the previous section, due to the fact that the field pulse durations are significantly larger than the characteristic precessional times of the system, they still support the idea of better controlled switching events, if only for the stabilisation of end domains. Again, attempting to validate the mechanisms of magnetisation switching drives us to the frontiers of experimental techniques' capabilities (see [18]).

The *initial* quasi-coherent magnetisation rotation of the platelet's inner core region is uniquely controlled by the transverse field pulse, actively exploiting the S state demagnetising field-mediated high transverse susceptibility. Stabilisation of the average magnetisation component in the aftermath of the demagnetising field controlled motion is imposed by a sole longitudinal ($+x$-directed) field pulse, that is delayed with respect to the transverse field pulse. The results of a near optimised numerical switching experiment, where all field pulse parameters have been selected in order to obtain a quasi non-ringing switching

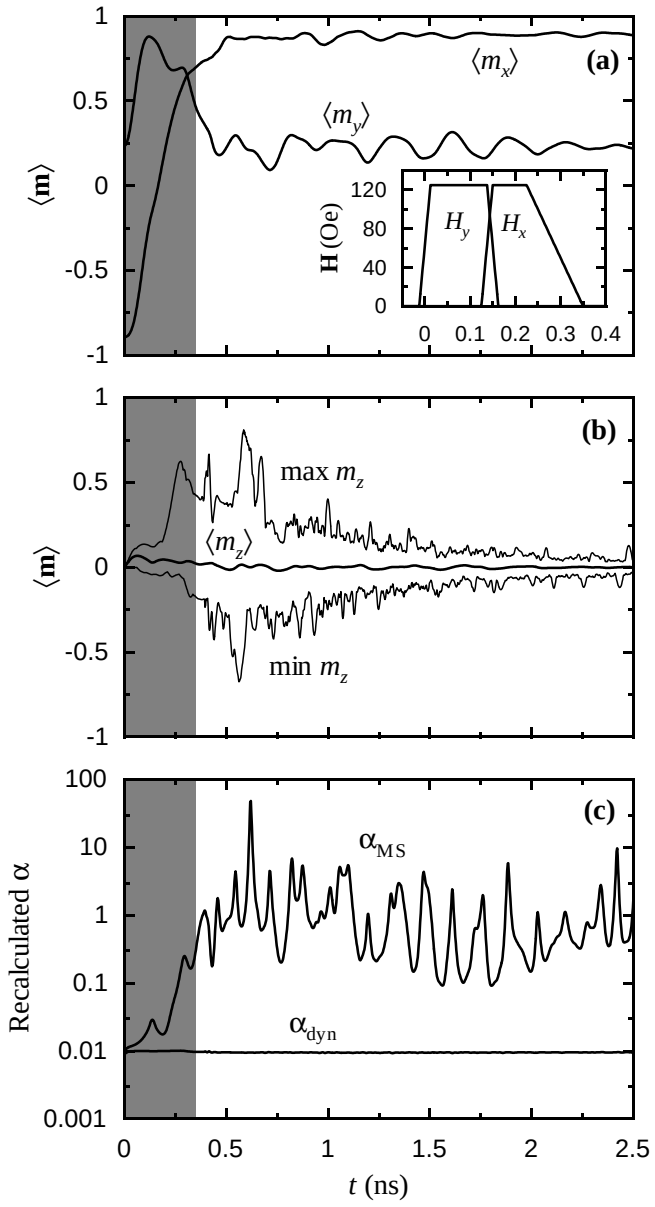

Figure 4.9: Near optimised, quasi non-ringing, sequential field pulse switching experiment. Grey areas stand for the time window were field pulses are nonzero. **(a)** In-plane average magnetisation components. The inset displays the profile details of both field pulses. **(b)** Maximum, average, and minimum out-of-plane magnetisation component. **(c)** Recalculated α values according to Sect. 3.2.

event, is presented in Fig. 4.9 and is to be compared with those given in the previous section. In broad terms the switching mechanism can be divided into these two phases, but the intricacies of the process deserve that we enter into the fine details by providing a series of magnetisation snapshots taken at selected time values (Fig. 4.10). After the

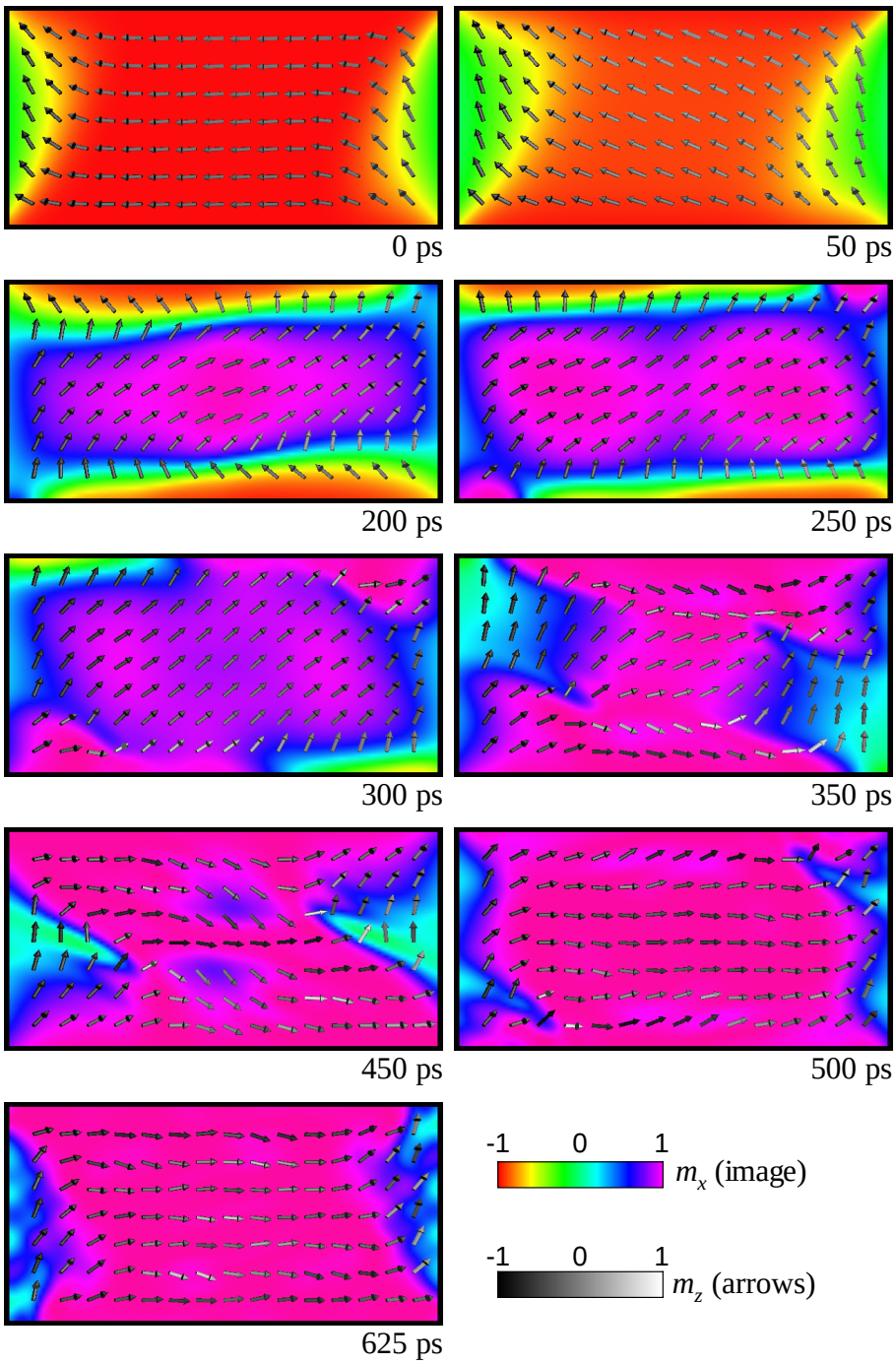

Figure 4.10: (Colour) Sequence of magnetisation snapshots corresponding to the curves presented in Fig. 4.9.

application of the transverse field pulse ($\approx$ 200 ps), the magnetisation in the platelet's core region has almost completely rotated towards the positive x direction. The magnetisation distribution now resembles to a rotated (directed along y) S state. At the top and bottom edges, magnetisation is still pointing along its original direction ($-x$). Completion

of the switching process, under the action of the longitudinal field pulse, should now get rid of these newly developed edge closure domains (see also [48]). This is achieved by the development of a magnetisation fluctuation at both the top and bottom edges of the platelet that will eventually push the end domains towards the left and right boundaries, respectively (see Fig. 4.11). These highly localised fluctuations, besides moving along the top and bottom edges, also propagate towards the element's core in what resemble soliton like waves (300 and 350 picoseconds snapshots in Fig. 4.11 and Fig. 4.12). The strong precessional motion associated with such fluctuations is also the driving force behind the completion of the switching process and the overall definition of a plus x oriented S state. This can most clearly be seen in the magnetisation snapshots representation of Fig. 4.12. While the centre region of the platelet slowly rotates clockwise under the action of the external x field pulse, areas corresponding to the passing of these magnetisation fluctuations (coloured in blue) almost immediately align their magnetisation with the direction of the field pulse (see in particular the 350 ps snapshot).

From the collision of these fluctuations at the element's centre results a background of magnetisation oscillations on a small spatial scale, which nevertheless preserve the initial direction of the S state's closure domains. The expulsion of the newly created top and bottom end domains is followed by a final phase where, essentially, the system relaxes into its new equilibrium configuration ($+x$-directed S state). This occurs in a relatively long time scale within which magnetisation fluctuations damp out through a mechanism resembling that of mode ramification with its associated energy transfer into shorter wavelength fluctuations (Fig 4.13). In the end, the out-of-plane magnetisation component landscape proves strongly reminiscent of water waves in a confined volume, presenting, nonetheless, at a small spatial scale, relatively large fluctuations as compared with the average value (compare the curves given in Fig. 4.9**b**). Another particular feature of this process relates to its associated (overall) damping value, as given by the α_{MS} values in Fig. 4.9**c**, which, on the average, appears to display a critical value close to 1, a clear indication of the damping efficiency of such mechanisms.

Interestingly enough, full animations of switching events such as represented in Figs. 4.10 and 4.11 leave the impression of interactive surface waves with apparent reflections along the element's boundaries. Such a picture would remain essentially incomplete without noticing that waves are here *precessional waves*. Their activity depends on the effective

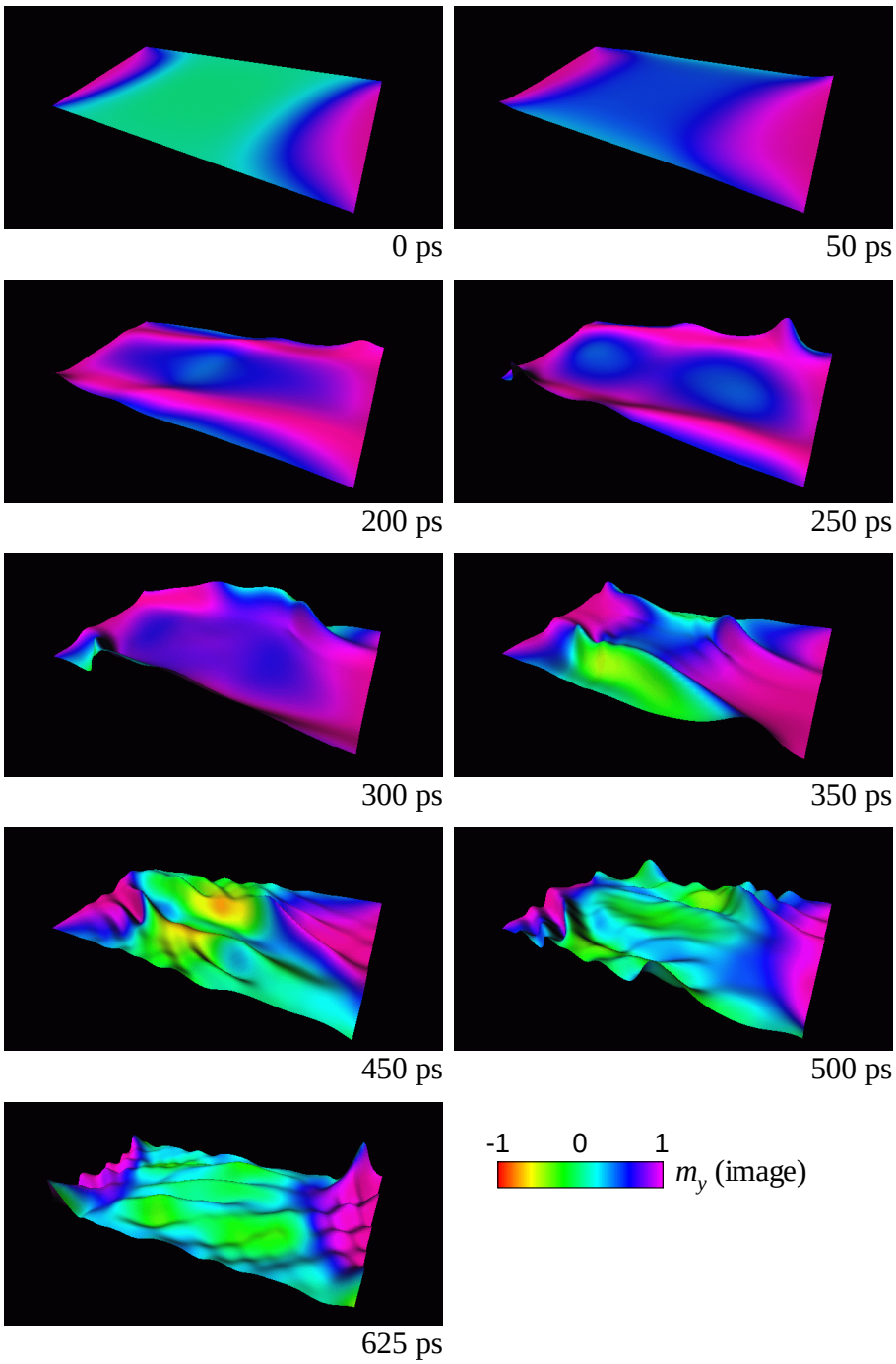

Figure 4.11: (Colour) Sequence of magnetisation snapshots corresponding to the curves presented in Fig. 4.9 and in a one-to-one correspondence with the images given in Fig. 4.10. The three-dimensional surface is scaled by the out-of-plane magnetisation component and coloured according to the value of m_y.

field distribution which gives rise to them. At the same time, due to damping and wave interaction, the effective field landscape evolves continuously. Here waves must therefore

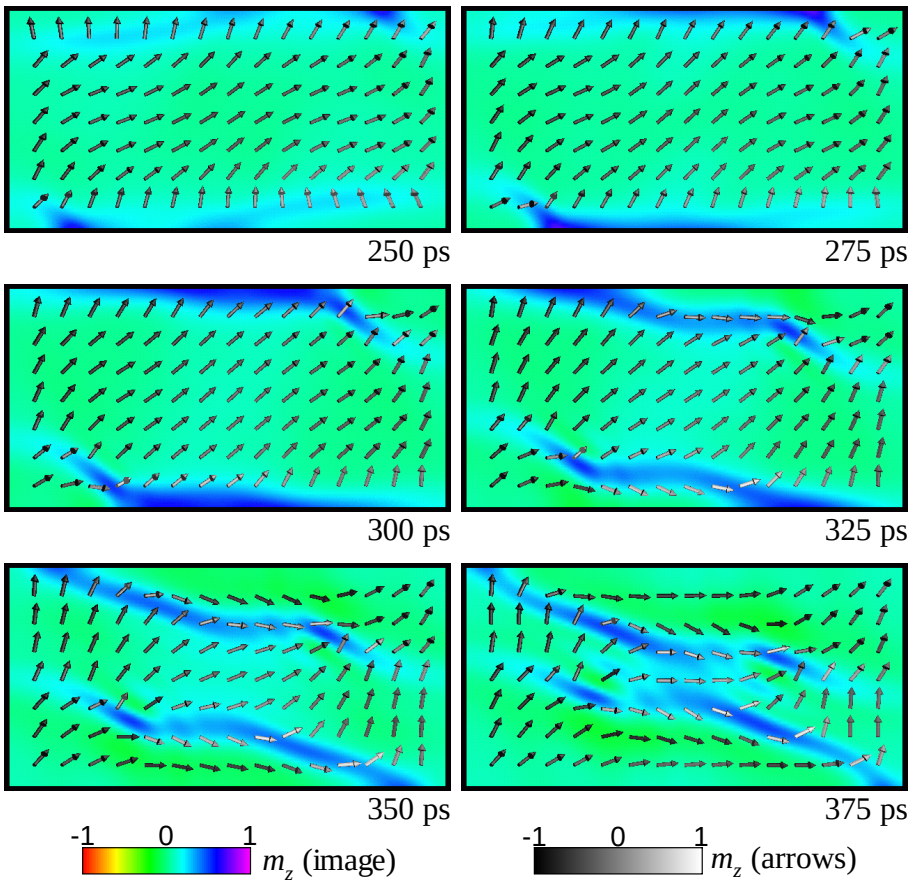

Figure 4.12: (Colour) Magnetisation snapshots highlighting the out-of-plane fluctuations arising from the longitudinal field pulse and the corresponding strong precessional motion of magnetisation swiftly rotating towards positive x values.

not be compared to the superposition of waves in a purely elastic medium in the linear excitation regime, namely a regime where Hooke's law applies. The experiments of Acremann and coworkers [49] provide the closest experimental realisation of micromagnetic simulations of the type shown here. Consider an experiment sensitive to the out-of-plane magnetisation component (Polar Kerr Effect, for instance), then a tree-dimensional representation of the experimental signal versus position and time would yield pictures essentially comparable to those of Fig. 4.11, although a large increase in spatial resolution is still required.

As already stated, fully continuous magnetisation transitions ensure the overall conservation of the lateral edge domains magnetisation directions, leading to the stability of an S to S state switching. This is all the most important since no transverse field pulse,

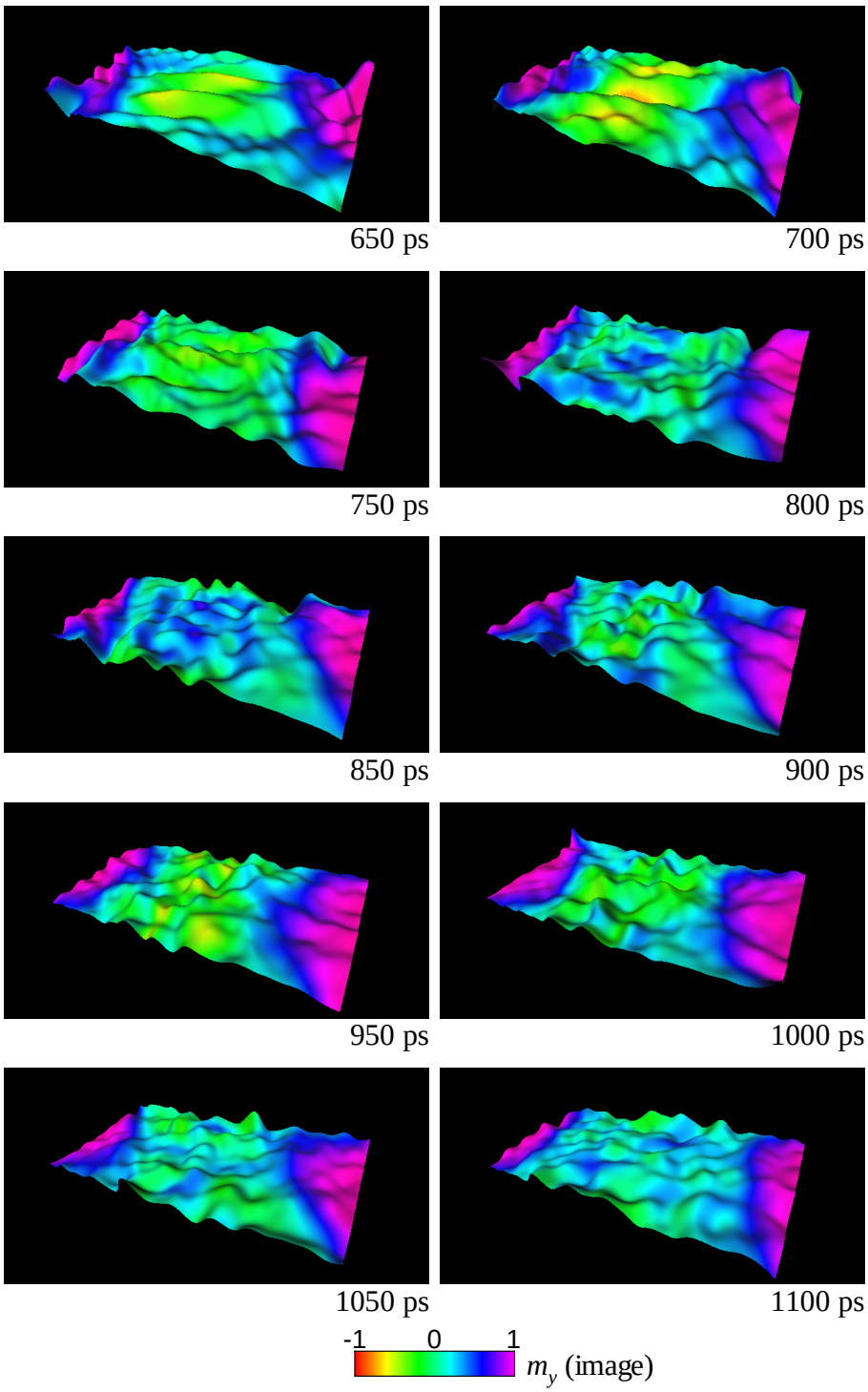

Figure 4.13: (Colour) Evidence for mode ramification leading to efficient energy dissipation at long times. As in Fig. 4.11, the three-dimensional surface shown is scaled by the out-of-plane magnetisation value.

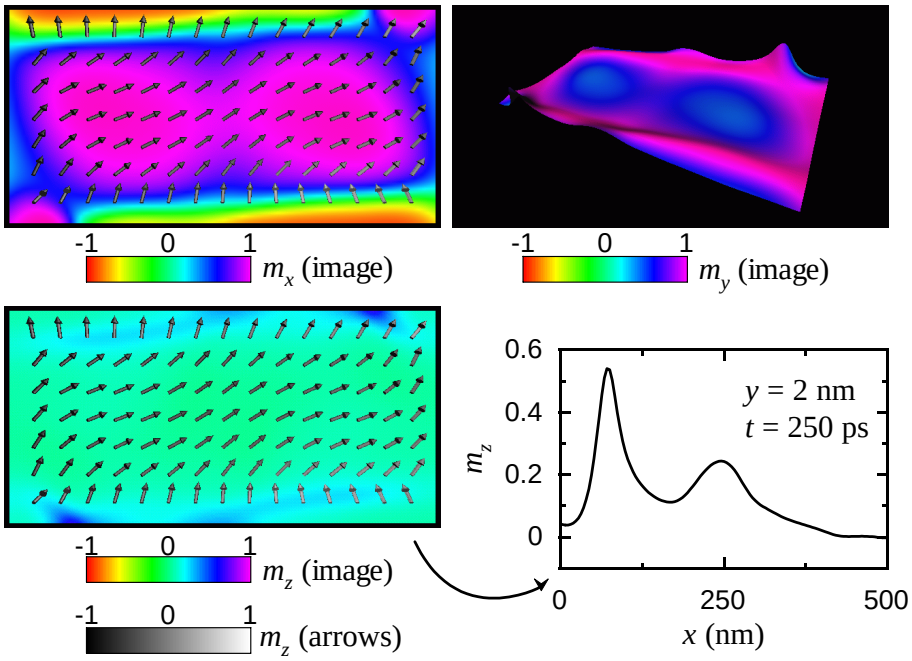

Figure 4.14: (Colour) Different magnetisation snapshots corresponding to the initial stage of end domains expulsion through the displacement of top and bottom edge fluctuation ($t = 250$ ps). The graphic displays the out-of-plane magnetisation profile along the platelet's bottom edge.

possibly imposing a single oriented end domains direction, is any more applied after some 150 ps. It should be stressed that during the process of (top and bottom) end domains expulsion, no nucleation of micromagnetic structures occurs. In fact, the magnetisation fluctuations responsible for such end domains expulsion are perfectly continuous and at no instant in time the maximum (minimum) m_z magnetisation values reach the values +1 (-1). This is clearly shown in Fig. 4.14, where different snapshots of the same magnetisation distribution are given (corresponding to the initial stage of edge domains expulsion), along with the magnetisation profile of the bottom platelet's edge (see also Fig. 4.9**b**). It should be borne in mind that C and S states almost possess the same energy and one must ensure that no parasitic transition between these two magnetisation configurations occurs during switching, which could lead to undesirable creep effects.

In accordance with the MRAM operating principles outlined in the beginning of this section, memory cell write selectivity relies upon the combined action of two (essentially orthogonal) current generated field pulses (see Fig. 4.4). As such, for the sequential field pulse switching experiment described above to be effectively used as a guideline for the

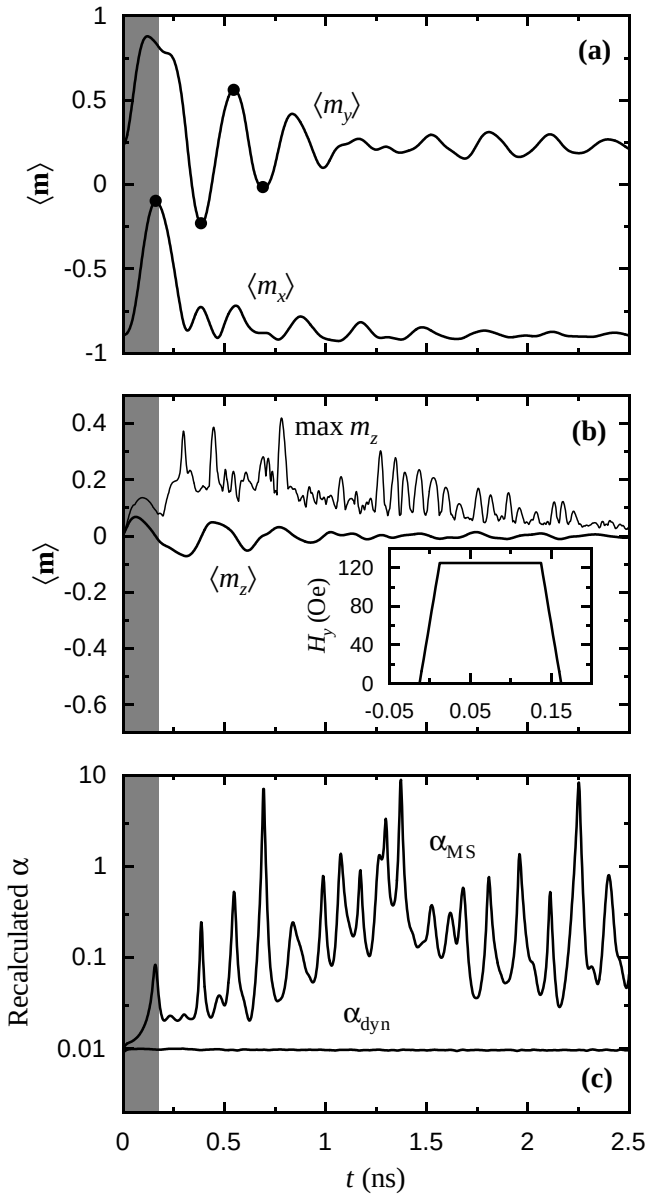

Figure 4.15: Write selectivity demonstration for the transverse field pulse case. The shaded regions represent the time window where the field pulse has a nonzero value. **(a)** In-plane average magnetisation components. **(b)** Average and maximum out-of-plane magnetisation values along with the applied field pulse profile (exactly equivalent to the transverse pulse component in Fig. 4.9). Note the reduced vertical scale. **(c)** Recalculated α values.

development of reliable MRAM architectures, memory cells subjected to the action of a sole field pulse must not switch. The predicted behaviour for cells such as considered here is presented in Fig. 4.15 for the transverse field case (applied field along the y direction). Although the average y magnetisation curve does display significant oscillations, and the

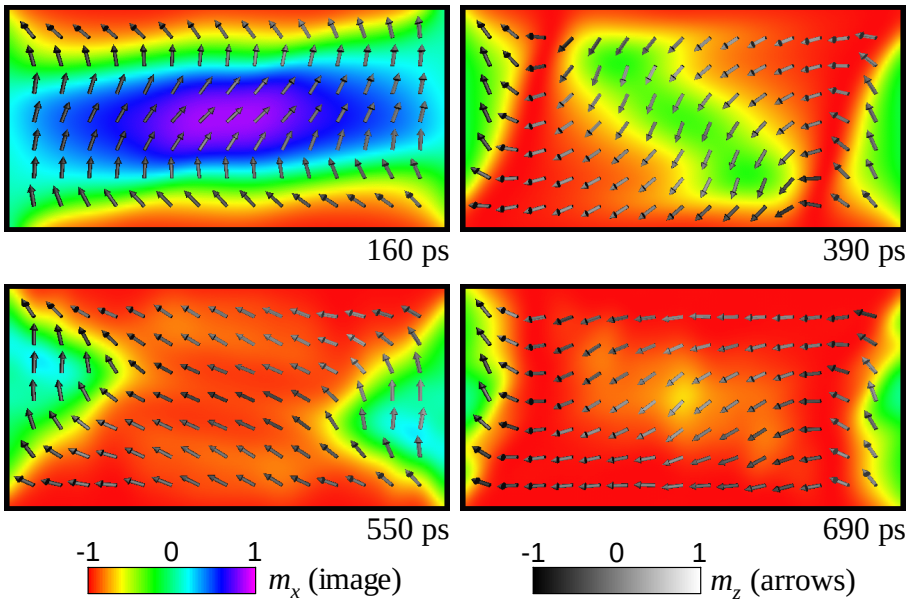

Figure 4.16: (Colour) Magnetisation snapshots roughly corresponding to the first oscillation period of $\langle m_y \rangle$ in Fig. 4.15**a** (dots).

$\langle m_x \rangle$ value almost reaches zero, the maximum out-of-plane magnetisation values remain well below the critical value of one. Likewise, the magnetisation snapshots, roughly corresponding to the first oscillation of the average magnetisation values (Fig. 4.16), provide evidence for a spring like behaviour, without the magnetisation distribution ever loosing a high degree of spatial continuity. Finally, comparison with the sequential field pulse switching data presented in Figs. 4.9 and 4.10 leads to the following comment. Under the sole action of the transverse field pulse, neither state switching, nor the nucleation of the magnetisation fluctuation ultimately responsible for the completion of the switching process, occur. If these two facts are related, the development of the aforementioned fluctuation is seen to be intimately connected with the action of the longitudinal applied field pulse (acting on a magnetisation distribution mainly oriented along y on the top and bottom edges), and, as such, the optimised switching experiment given in this section should exhibit a fairly large tolerance margin to y field pulse values, a probably key property when dealing with hard axis selectivity.

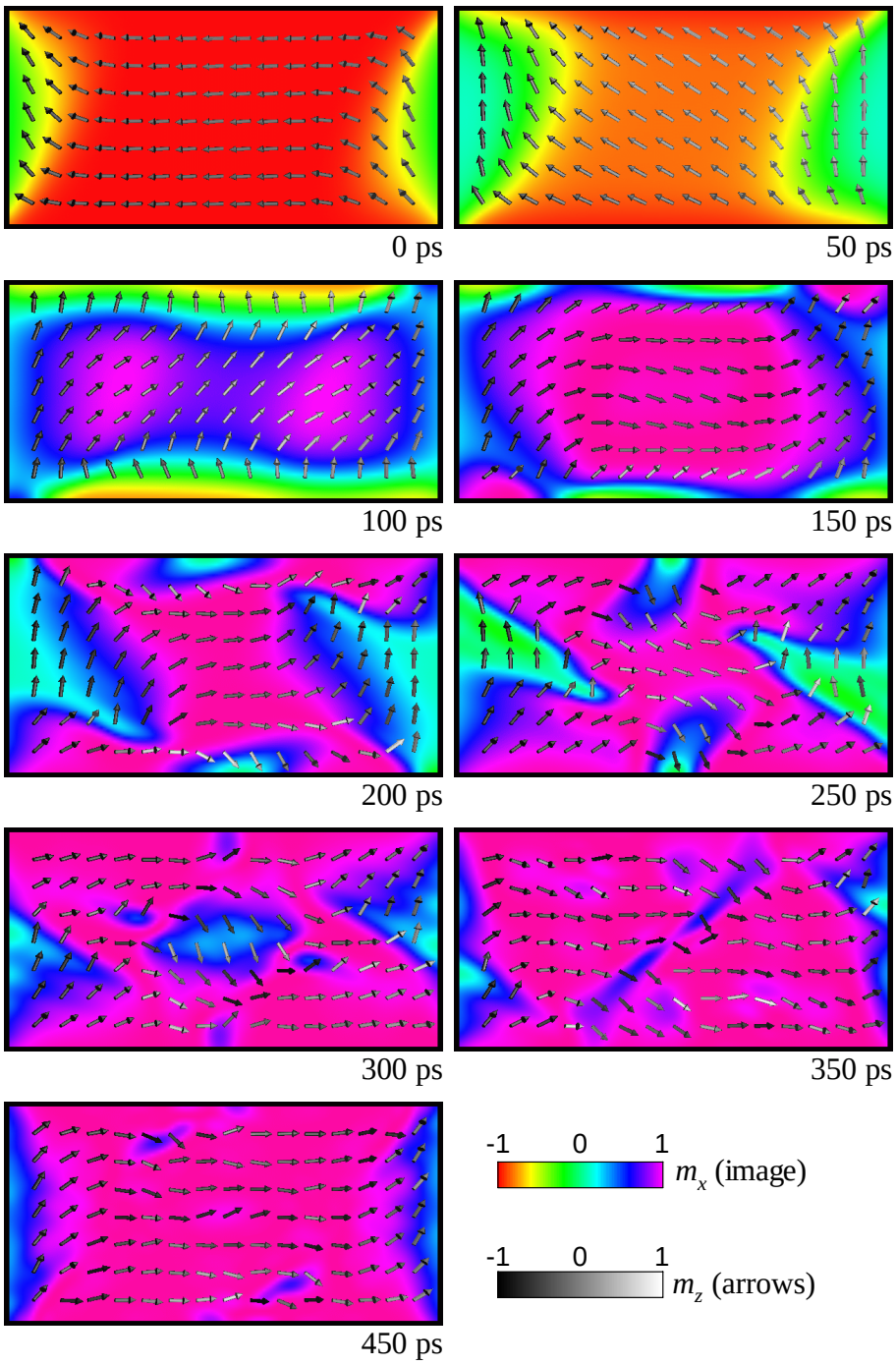

Figure 4.17: (Colour) Sequence of magnetisation snapshots corresponding to the curves presented in Fig. 4.6. Field cutoff instant: 146 ps.

Closing Remarks

Having reached this point in our discussion of precessional magnetisation switching in submicron-sized platelets it is of some pertinence to discuss in detail the differences between

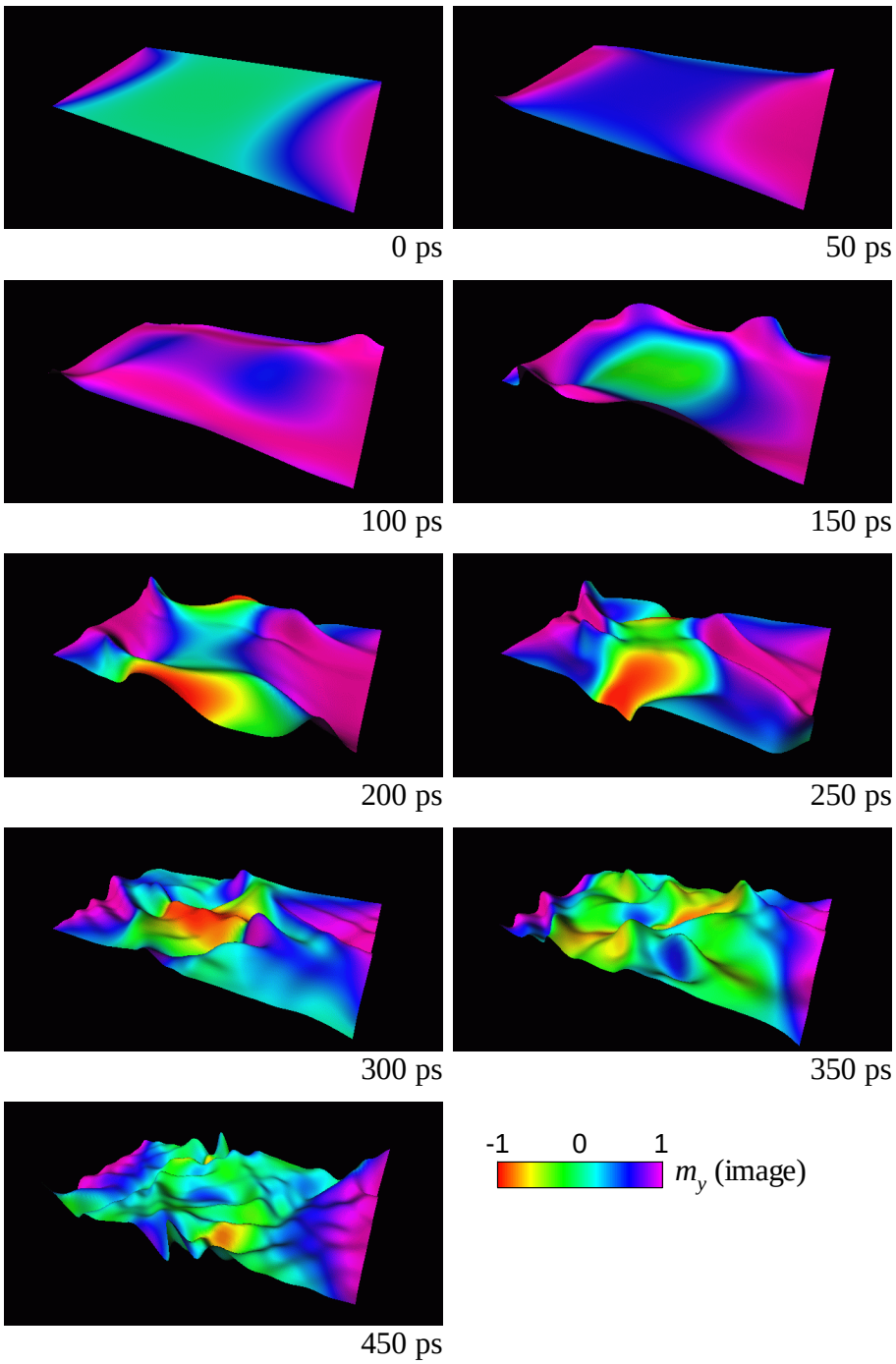

Figure 4.18: (Colour) Sequence of magnetisation snapshots corresponding to the curves presented in Fig. 4.6 and in a one-to-one correspondence with the images given in Fig. 4.17. The three-dimensional surface is scaled by the out-of-plane magnetisation component and coloured according to the value of m_y.

the use of simultaneous and sequential field pulses. The following discussion is based on Figs. 4.17 and 4.18 displaying sequences of magnetisation snapshots corresponding to the

non-ringing case in Fig. 4.6 (to be directly compared with Figs. 4.10 and 4.11, respectively).

An immediate remark concerns the nonzero field pulse time windows and the magnitude of the individual field components. Since an initial longitudinal field components triggers a counterclockwise magnetisation rotation of the platelet's core (as seen in Sect. 4.1), the transverse field component value needs to be high enough in order to compensate this effect so that an overall clockwise rotation may develop in the first phase of switching. Due to the enhanced y field, and the additional application of a $+x$ field, a mainly $+x$-oriented distribution is reached faster in the simultaneous pulse case (150 ps versus 250 ps for the shifted pulses simulations). This has nonetheless a cost. The initial presence of the longitudinal pulse more severely distorts the magnetisation distribution, as can be plainly seen for the 200 ps snapshot, and induces the development of the necessary out-of-plane fluctuation, responsible for the final unwinding of the top and bottom edge-pinned domains, in two locations instead of just one for the case of shifted field pulses. This seemingly innocuous fact generates, in the end, a fair amount of uncorrelated localised fluctuations leading to the same overall switching time as in the case of the time shifted experiment ($\approx$ 500 ps). In addition the development of several fluctuations at both top and bottom edges more closely resemble situations where micromagnetic structures are nucleated inside the platelet, therefore possibly restricting the operational margin for field pulse values. Finally, let us mention that at long times after pulse cutoff the nature of the still undamped magnetisation fluctuations are essentially the same. This short discussion might convince the reader of the greater stability attainable via field pulse time shifting. Thus, hopefully, a more reliable, stable, and controllable switching mechanism may be achieved.

Chapter 5

Incursion into the Real World

In the previous chapter, the foundations of a precessional-driven magnetisation state switching in submicron-sized platelets have been laid down. Despite the detailed analysis of the magnetisation processes taking place, the magnetic system under study still remained, what we might call, highly immaterial: A non-textured, perfectly defined, rectangular platelet immersed in free space. Attempting to handle the intricate features of the real world raises numerous difficulties. Nonetheless, a (necessarily brief) incursion into the real world subtleties must at least be attempted. This is done below through both the modelling of the effects of an underlying Artificial AntiFerromagnetic (AAF) stack on the Permalloy free layer and the introduction of structural disorder. Indeed, elements with reduced lateral dimensions will comprise only a limited number of grains with potential effects on the switching characteristics.

5.1 Sensitivity to Edge Roughness: Selected Examples

The precessional switching mechanism described in Sect. 4.2 relies essentially on the initial and coherent magnetisation rotation of the element's core region. In order to more clearly underline this interdependence, a comparison is made here between a switching experiment in a perfectly defined rectangular element (as used in previous chapters) and two less than perfect platelets, mimicking the possible outcome of a lithographic process: A simpler structure where the four corners of the platelet were rounded off and a more *realistic* structure, where edge roughness is supposed to arise from selective grain etch/lift-off (Figs. 5.1 and 5.2).

Simulations of rectangular elements presenting rounded corners and edge irregularities

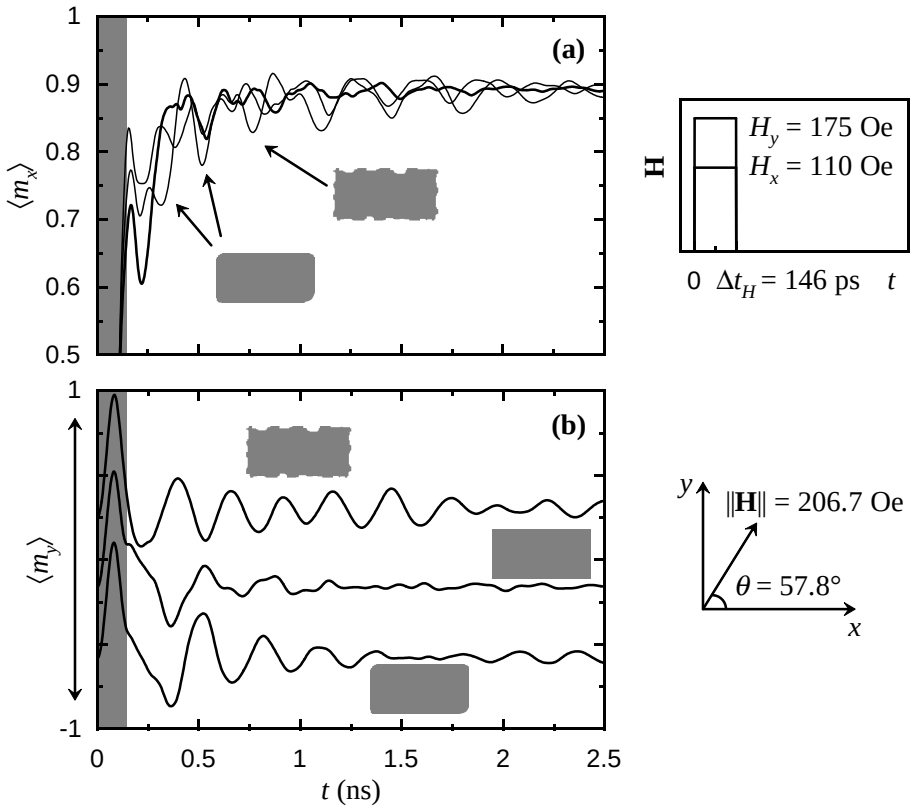

Figure 5.1: Comparison between a precessional switching experiment in perfect rectangular elements and irregular platelets. Field pulses characteristics are displayed on the right and correspond to the switching experiment in Sect. 4.2.1. The grey regions denote nonzero field values. **(a)** Average x magnetisation curves. The bold line corresponds to the perfect element. Beware of the expanded vertical scale. **(b)** Average y magnetisation curves (vertically shifted for increased visibility).

were performed using the publicly available micromagnetic simulation package OOMMF (Object Oriented MicroMagnetic Framework) [50] developed at the National Institute for Standards and Technology (NIST). In order to ensure that both codes provided the exact same magnetisation motion, a comprehensive analysis of numerical control parameters was carried out. In particular, spatial discretisation values and integration time steps were strictly surveyed in test case simulations (for example, the transverse oscillations experiments described in App. A and the Standard Micromagnetic Problem No. 4 [51] presented in App. B).

Figure 5.1 displays the average in-plane magnetisation curves during switching for the three structures considered. In all cases, magnetisation switching is achieved within the same time window as before (well below the first nanosecond). Sizeable oscillations

in the y magnetisation component are, however, observed for the non-perfect elements. Actually, the three simulations were made using the field parameters which induced the nearly optimised square (and simultaneous) field pulse switching of Fig. 4.6 (see also the schematic diagrams in Fig. 5.1), and no attempt has therefore been made at the precise definition of corrects field parameters for each of the irregular platelets. As before, average magnetisation trajectories along with time-selected magnetisation snapshots allow for a deeper understanding of the various phases of the switching process. This data is displayed in Fig. 5.2. As expected, since the initial out-of-plane magnetisation motion is intimately associated with precession around the demagnetising field, the three curves presented nearly superpose with one another during the first stage of switching.

The magnetisation distribution images showed correspond to the instant when the applied field pulses were switched off ($t = 146$ ps). The centre region of the platelet is completely reversed and the overall magnetisation distribution remains highly insensitive to the details of edges/corners definitions. Despite the presence of highly irregular platelets no nucleation of micromagnetic structures occurs, demonstrating the robustness of *precessional-driven* magnetisation switching. Only the details of post-switching fluctuations differ. The exact same arguments can be demonstrated to hold valid when considering intentionally fabricated irregular platelets, such as elongated hexagons, ellipses, and eye-shaped elements [52].

5.2 The Role of Artificial AntiFerromagnetic Structures

Since in 1995 Heim and Parkin [53] introduced the use of Artificial AntiFerromagnetic (AAF) stacks as pinned layers in pseudo-spin valve structures, a considerable amount of effort has been put into the study of such structures (sometimes also referred to as Synthetic AntiFerromagnets). The driving force behind such developments is the search for both pinned layer stability and a reduction in the stray field (magnetostatic coupling) sensed by the free layer (besides thermal stability, which will not be further evoked here).

The goal of this section is not so much a detailed study of the dynamic behaviour of AAF stacks but their possible influence on the switching characteristics of the free layer. Throughout the following pages the discussion will evolve always towards higher degrees of complexity, especially through the introduction of structural disorder.

The choice of Co/Ru/Co stacks was made due to the possibility of achieving large

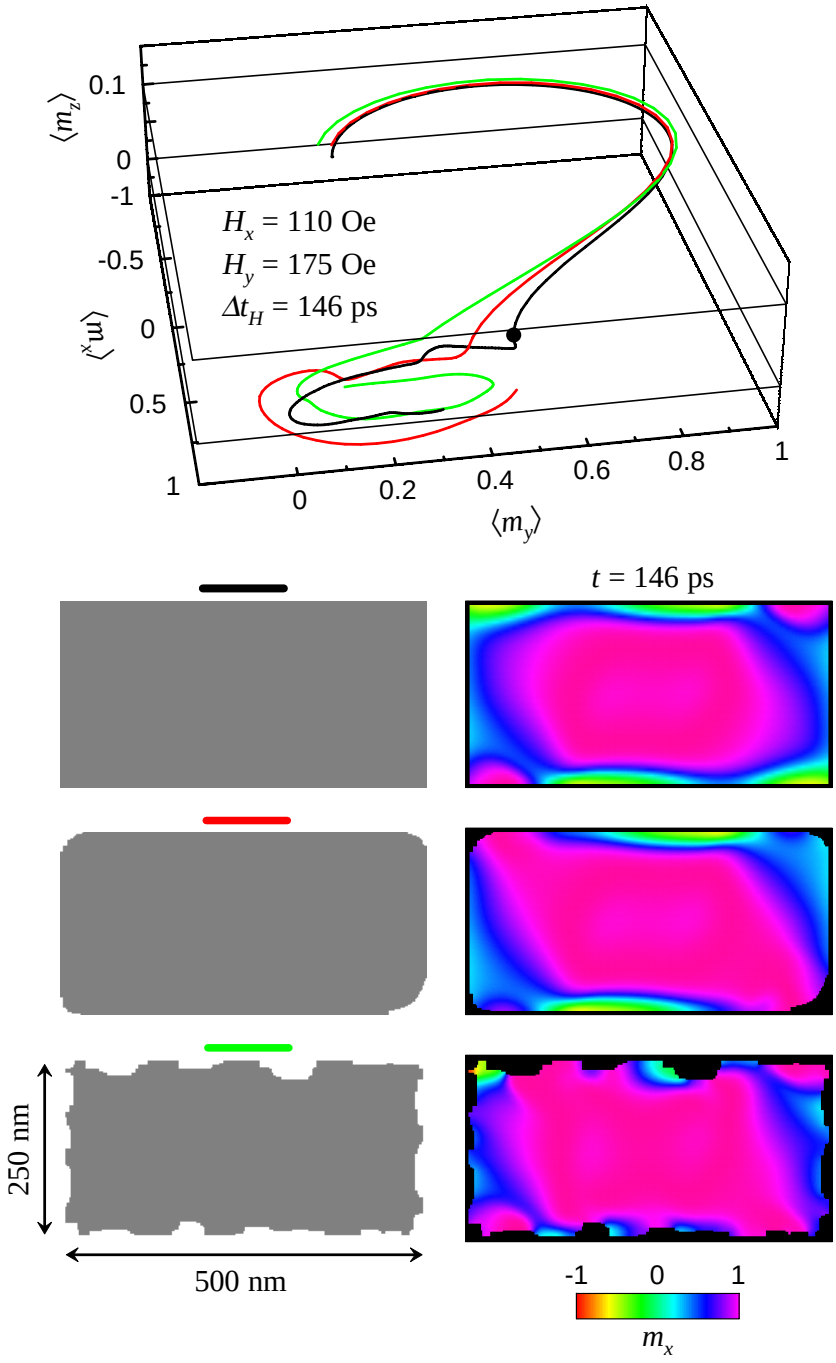

Figure 5.2: (Colour) Average magnetisation trajectories corresponding to the parameters in Fig. 5.1. The curves shown correspond to a duration of ≈ 0.5 ns. Magnetisation snapshots were taken at the same instant in time (field cutoff) and provide evidence for essentially the same switching mechanism: Inner core magnetisation reversal, which revealed itself very insensitive to edge and/or corners roughnesses.

values of interlayer antiferromagnetic exchange coupling, for a considerable wide range of Ru thickness [54]. Symmetric AAF stacks were considered, where both Co layers were 3 nm thick and the Ru was 0.7 nm. For such values of Ru thickness, exchange coupling values as large as 1 erg/cc have been reported [55]. Although the thickness of the Ru spacer defines the strength of the coupling between the two Co layers, this interaction has no intrinsic in-plane preferential direction. This in-plane preferential direction is usually imposed through exchange biasing the AAF stack with an antiferromagnetic layer. Here, however, no exchange bias layer was modelled and the AAF structure was simply cut down to the usual 2:1 aspect ratio, having the largest dimension of 500 nm.

5.2.1 AAF Stability under Static Fields

The use of AAF structures as pinned layers requires field stability. Thus, a static field was first applied along both the longitudinal and transverse (in-plane) directions. Data is shown in Fig. 5.3 for a Co (3 nm)/Ru (0.7 nm)/Co (3 nm) symmetric stack in an initial, fully antiparallel, double S State configuration. Up to 150 Oe field values, the average transverse magnetisation components only weakly depend on the applied field. The top Co layer (Fig. 5.3**c**), nonetheless, is slightly more responsive to both the x- and y-directed fields. This may be explained by the fact that the two Co layers are not symmetric with respect to the applied fields due to the different relative orientations of the edge closure domains. In the following, the assumption of the AAF stack's immobility will be made due first, to the relative insensitivity to field mentioned above and, additionally, to the fact that this sensitivity would be further reduced in the case of an AF-pinned AAF stack.

The fully antiparallel double S state configuration in the AAF stack is not only imposed by the strong interlayer exchange coupling across the Ru spacer but is also favoured through a charge compensation phenomenon between both Co layers (see Fig. 5.4**a**). Nonetheless, due to the generally weak interlayer exchange coupling through the spacer separating the free and pinned layer (see Fig. 5.4**b**), four possibilities are available for the relative orientation of magnetisation in the free layer relative to the AAF stack. In order to investigate the minimum energy configuration for this three-layer structure, the remanent magnetisation distributions were computed for the four possible free layer magnetisation orientations, as shown in Fig. 5.4**c**. Since the magnetisation distribution in the AAF stack remained unchanged and that of the free layer correspond to symmetry reflections along the x and y axes, the only possible energy differences necessarily arise

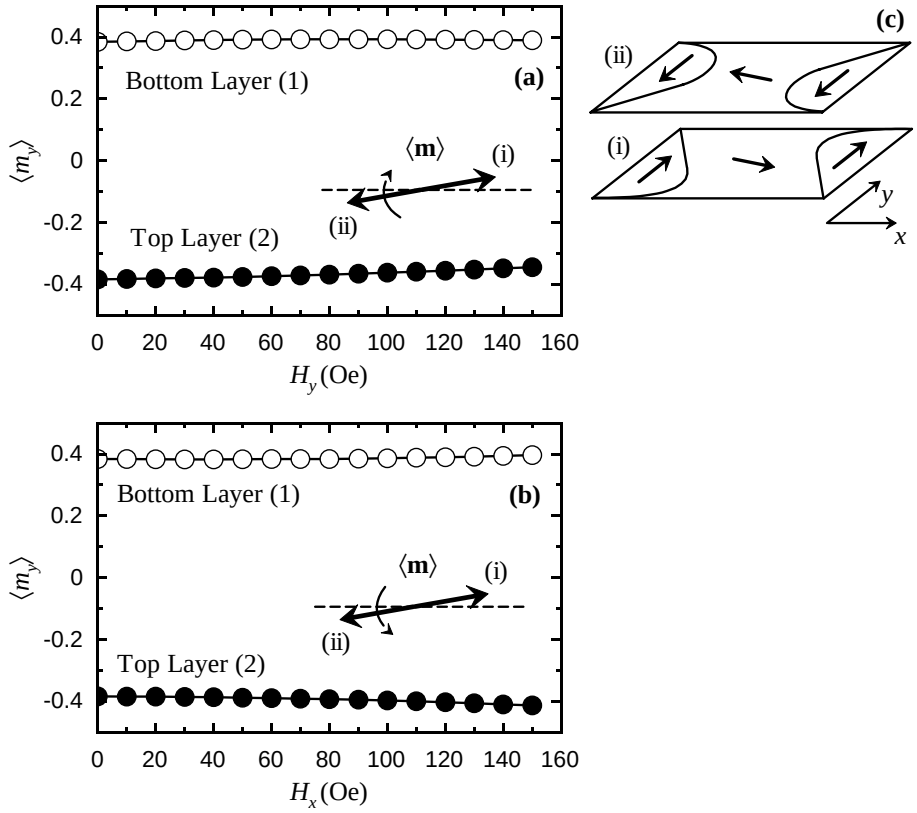

Figure 5.3: Field stability of an AAF stack. The magnetic parameters used for Co were $M_s = 1400$ emu/cc, $A = 2 \times 10^{-6}$ erg/cm. No anisotropy contributions were considered. **(a)** Transverse field. **(b)** Longitudinal field. **(c)** Schematic diagram of the remanent magnetisation distributions in the AAF stack.

from the magnetostatic coupling (Zeeman type) between the underlying AAF stack and the topmost magnetic layer, namely

$$-\int \mathbf{m} \cdot \left(\mathbf{h}^{(1)}_{\text{stray}} + \mathbf{h}^{(2)}_{\text{stray}} \right) d\mathbf{r} \quad , \tag{5.1}$$

where $\mathbf{h}^{(i)}_{\text{stray}}$ are seen to behave as external applied fields on the free layer. These values are given Fig. 5.4**c** in reduced units for a 5 nm thick Permalloy layer. A fully antiparallel three-layer stack is seen to be the lowest energy configuration (the corresponding free layer magnetisation distribution is also shown in Fig. 5.4**c**). Although the basic features of the S state distributions on both the AAF layers and the free Permalloy layer are essentially equivalent, due to charge compensation across the Ru spacer, magnetisation configurations on the Co layers have slightly more symmetric edge closure domains.

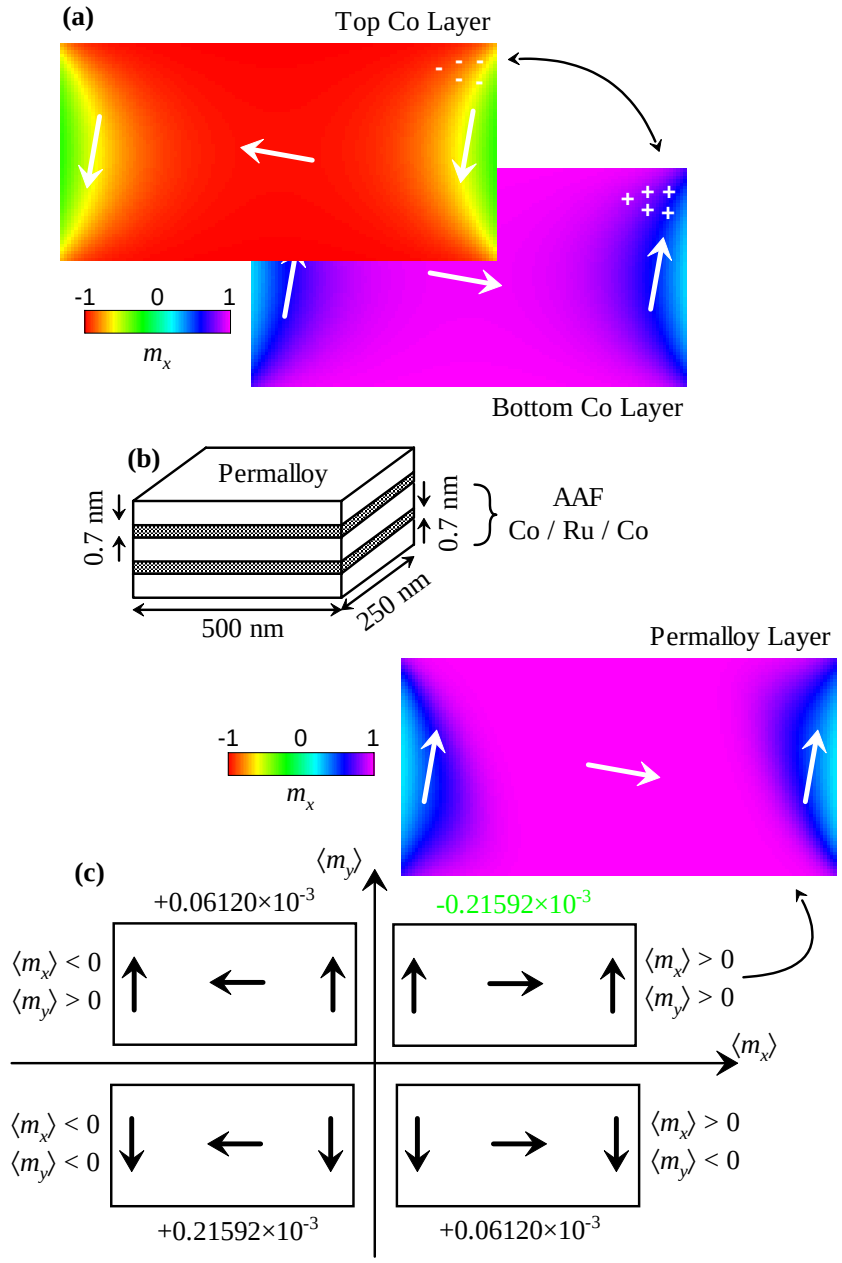

Figure 5.4: (Colour) Determination of the remanent distributions in a three-layer stack. **(a)** Remanent magnetisation distribution in both Co layer composing the AAF stack. **(b)** Schematics of the system considered. **(c)** Values of the magnetostatic coupling energy for unit volume and for the four different magnetisation states in the free Permalloy layer (5 nm thick).

5.2.2 Introducing Structural Disorder

The effects of structural disorder are next considered. Both Co layers were considered as fcc with a cubic anisotropy value of $K_1 = -1.0 \times 10^6$ erg/cm^3. Inside each grain a cubic

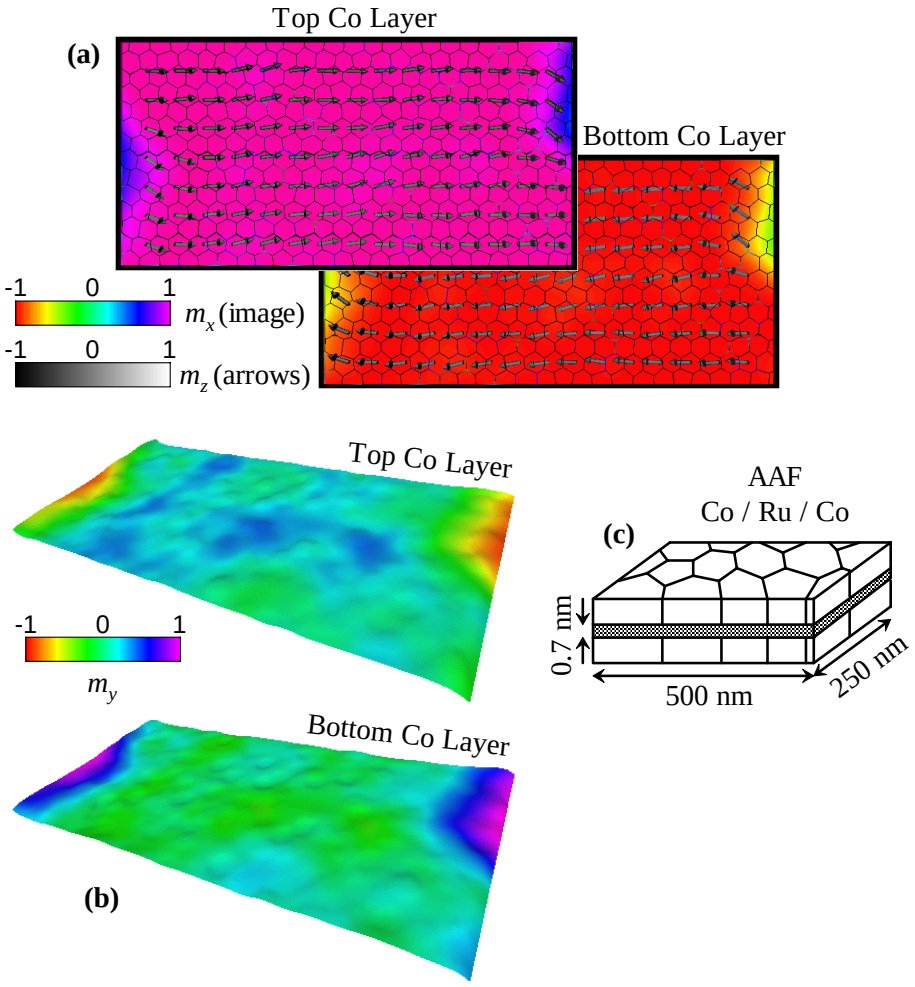

Figure 5.5: (Colour) Remanent x magnetisation component distribution in a textured AAF stack. **(a)** In-plane magnetisation distribution superimposed on the grain structure modelled. **(b)** Transverse magnetisation distribution (in colour) along with a three-dimensional mapping of the out-of-plane (z) magnetisation values. **(c)** Schematic diagram of the textured AAF stack.

anisotropy with a three-dimensional random orientation was assumed. Each Co layer was decomposed in an ensemble of grains having an average diameter of approximately 100 Å, and the anisotropy axes were randomly oriented in space. Figure 5.5 shows a schematic representation of the AAF stack considered and the remanent magnetisation distribution.

Direct comparison with the remanent magnetisation distributions of Fig. 5.4 for non-textured Co layers reveals the influence of the structural disorder introduced. Apart from small magnetisation fluctuations spreading through the whole of the platelet, both in the plane (Fig. 5.5**a**) and out of the plane (Fig. 5.5**b**), one immediately observes the strong

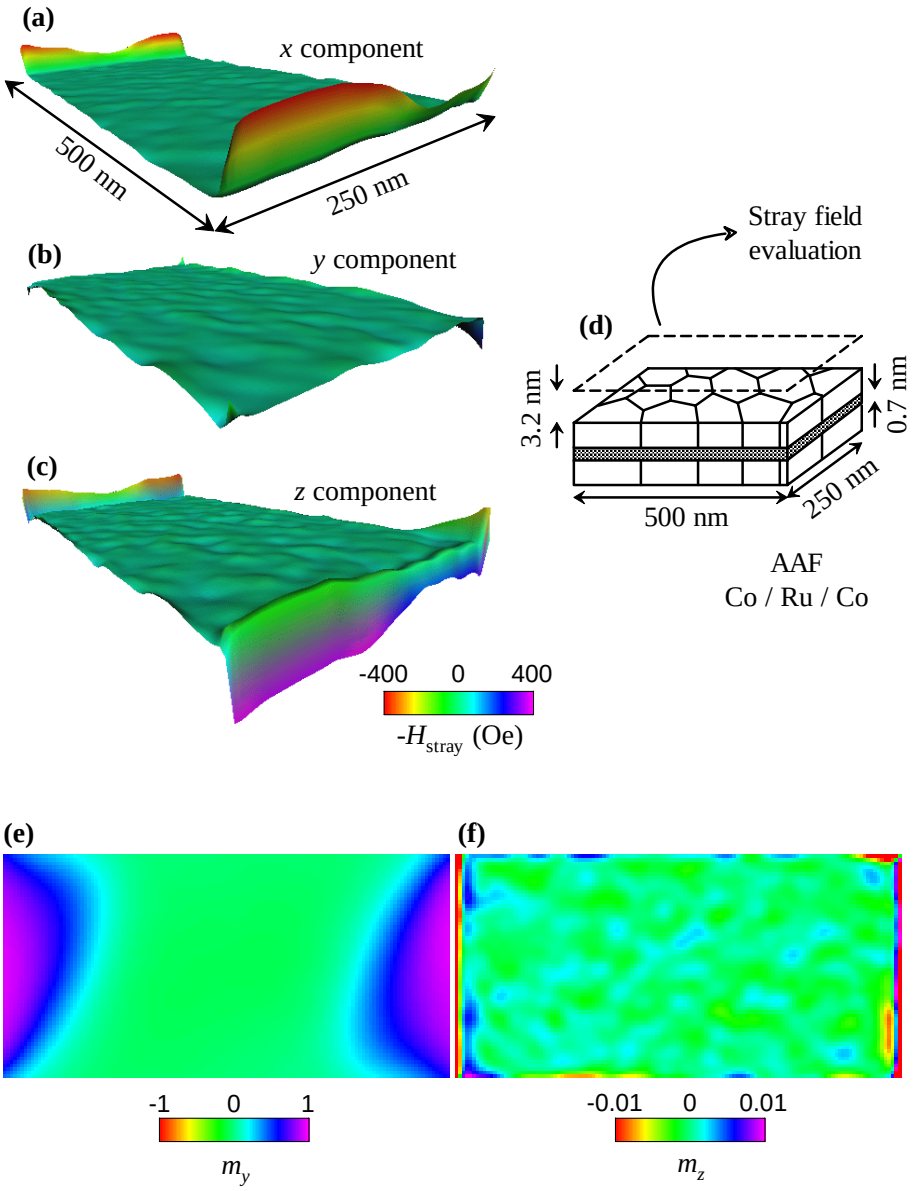

Figure 5.6: (Colour) Surface mapping of the AFF's stray field. **(a)**–**(c)** Field components. Both the colour code and the three-dimensional surface mapping correspond to the indicated component. **(d)** Stack schematics. **(e)**–**(f)** Remanent free Permalloy configuration. Note the highly expanded scale used for the m_z snapshot.

reduction in size of the edge closure domains of both Co layers S state. This is due to the interlayer magnetostatic coupling between the two AAF layers, but also to their irregular shape comes as a consequence of the strong random anisotropy existing inside each grain.

Quantifying the stray field sensed by the free layer on top of the AAF stack depicted in Fig. 5.5 comes as the next question. Given the system presented in Fig. 5.5, the

components of such stray field, evaluated at a distance of 3.2 nm, are displayed in Figs. 5.6**a** through 5.6**c**. This distance corresponds to the centre (in thickness) of a 5 nm thick layer separated by a 0.7 nm spacer from the AAF stack (Fig. 5.6**d**). At the edges of the platelet, large stray field values can be present, the magnitude of which can exceed 400 Oe for the material parameters and the geometry considered. Despite these high values, field amplitude decreases rapidly towards the interior of the magnetic element. At only 10 nm from the lateral surfaces (i.e. essentially two exchange lengths in Permalloy), the field amplitude is reduced in magnitude to values comprised between 30 and 50 Oe. Field fluctuations inside the free platelet arise from the magnetic disorder introduced into the Co layers of the AAF stack (compare the spatial length scale of the out-of-plane magnetisation fluctuations in Fig. 5.5**b** with the mapped surfaces in Figs 5.6**a-c**).

The effects of such a magnetic field distribution on the remanent magnetisation configuration of the free Permalloy layer (located at the same height) is presented in Figs. 5.6**e** and 5.6**f**. The free Permalloy layer is now modelled together with its associated texture, different from that of the Co layers. This choice was suggested by the fact that an amorphous oxide layer would separate the free layer from the AAF stack in tunnel junctions. The coherency of the grain structure would thus not be maintained. A cubic anisotropy was considered, with axes being randomly distributed from grain to grain ($K_1 = -5.0 \times 10^3$ erg/cm^3). Surprisingly enough, the magnetisation state is almost completely unaffected by the presence of the AAF's stray field. This is due to the softness of Permalloy, large exchange constants smoothing completely any small deviations from the remanent (nil stray field) configuration (note the highly expanded scale in Fig. 5.6**f**). In particular, magnetisation is essentially in an S state defined in the film plane. The maximum value of m_z in the free layer is 0.0345, corresponding approximately to an angle of 2°. This out-of-plane magnetisation components must necessarily have developed as a reaction to the sensed stray field. This implies that small magnetisation rearrangements generate an internal effective field that almost perfectly counterpoise the sensed stray field. In order to demonstrate this hypothesis, the z components of both the internal effective field and the sensed stray field are plotted in Fig. 5.7**a-b**. The choice of the sole z component representation can easily be justified. Since the out-of-plane magnetisation component are actually very small, i.e. the magnetisation essentially lies on the platelet plane, the z component of the effective field, is actually at an almost perpendicular angle with respect to the magnetisation. It, therefore, gives rise to a nonzero torque on $\mathbf{m}$. Visual inspection

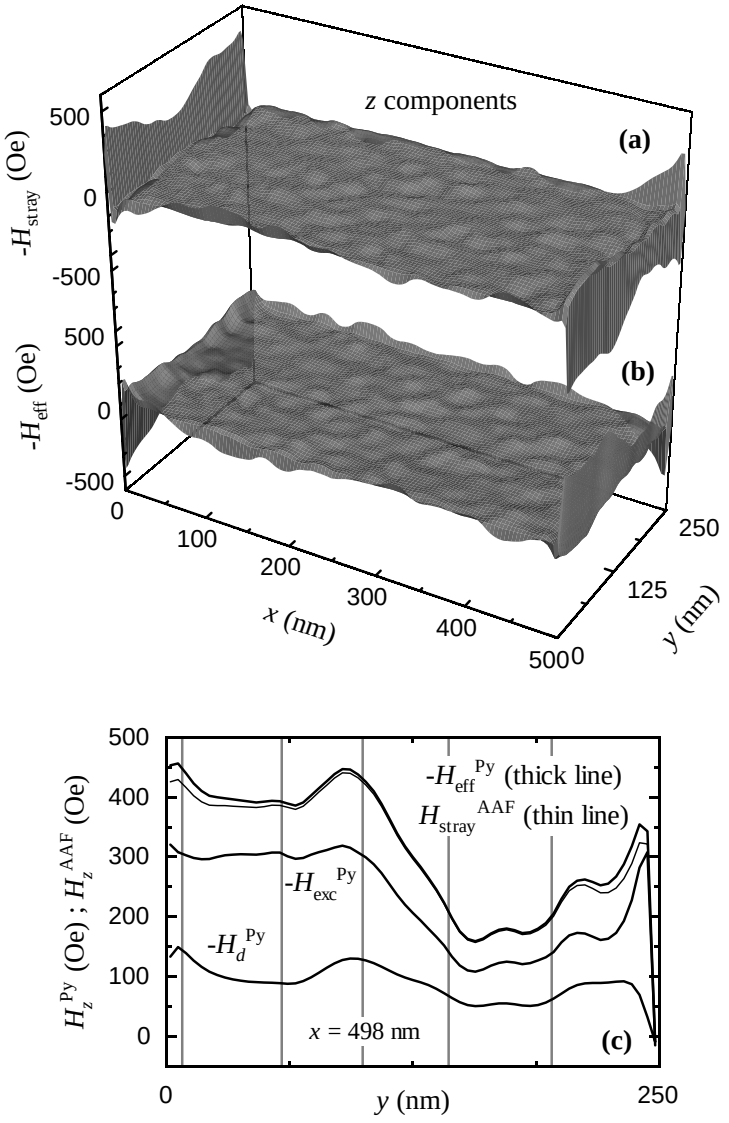

Figure 5.7: Comparison between the z values of stray field **(a)** and the internal effective field in the free Permalloy layer **(b)**. **(c)** Effective field contributions along the shorter right edge of the platelet. Grey lines represent grain boundaries in the Permalloy layer.

indicates that both field distributions almost perfectly cancel each other out.

To gain a better understanding of this compensation effect (especially near the edges of the platelet), a cut was made at the abscissa value of 498 nm, corresponding to the last magnetisation grid point in simulations (see App. A). Such data, conveniently separated into effective field contributions (exchange plus demagnetising), is displayed in Fig. 5.7**c**. Apart from the aforementioned field compensation, and perhaps contrary to common sense knowledge, exchange contributions to the effective field provide the largest reaction

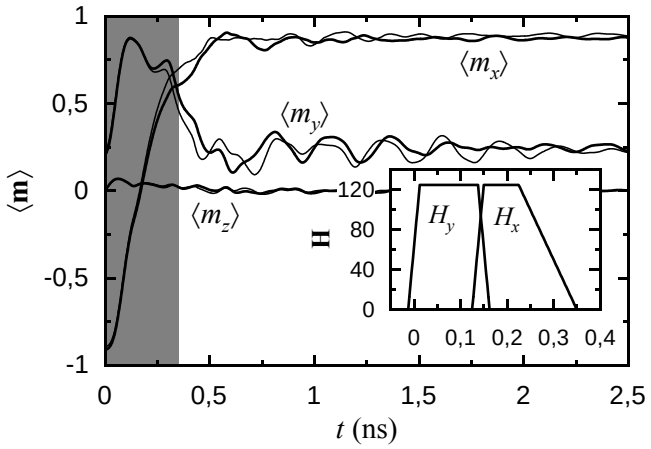

Figure 5.8: Comparison between the results of an optimised switching experiment in a non-textured element (thin lines) and the inhomogeneous Permalloy platelet immersed in the stray field arising from the disordered AAF structure in Fig. 5.5 (thick lines). The field pulse profiles are shown in the inset. The shaded area corresponds to nonzero field values.

to the presence of the very localised AAF-generated external field. Similar effects of internal field compensation, essentially governed by exchange interactions, are known to occur when dealing with micromagnetic singularities at edges and/or corners of perfectly defined rectangular (or three-dimensional parallepipedical) elements [56]. Again we should stress the fact that such high field values are the result of extremely small magnetisation deviations from equilibrium positions.

In closing this chapter, we attempt a quantification of the repercussions of these local magnetisation rearrangements on the switching characteristics of a textured submicron platelet. A straightforward comparison between the optimised switching experiment of Sect. 4.2.2 (time-shifted field pulses and a non-textured Permalloy layer) and the results obtained when considering a textured Permalloy layer subject to the stray field of the underlying AAF stack is exhibited in Fig. 5.8. Clearly, the switching process remains essentially unchanged even when due account is made for the inhomogeneous stray field originating from the AAF stack and for the possible microstructure of the free Permalloy layer. An overall final remark can be made when focusing on the time window following field application. The average y magnetisation component for the disordered AAF coupled element seems to relax faster than that of the perfect isolated element. This can probably be accounted for by considering the dephasing of the local magnetisation fluctuations due

to grain-induced disorder.

Summary

A description of the real world intricacies was attempted in this chapter. It focused on determining the influence of the following parameters on the precessional-driven magnetisation state switching described in the previous chapter:

- *Edge roughness.*
- *Artificial AntiFerromagnetic stacks' coupling and structural disorder.*

As a conclusion we can state that both the above factors produce a limited effect on the switching properties of the studied platelets. This is due to the following reasons. First, considering edge roughness, the quasi-coherent rotation mode triggered in the platelets inner region remains highly insensitive to the details of edge definitions. Second, due essentially to the softness of the Permalloy layers considered in this work, stray fields originating from a pinned AAF layer are swiftly screened off. Similarly, the effects of structural disorder (random anisotropy axes inside each ferromagnetic grain), modify only the details of post-switching oscillations, and this on a reduced scale.

Perspectives

As concluding remarks to this thesis' work, several additional research paths might be considered. Apart from detailed technical discussions regarding prototype validation, more fundamental insights into the nature of coherent precessional-driven magnetisation switching can be attained when considering the following topics.

If the continuing reduction of magnetic devices' lateral dimensions can only be propitious to the reinforcement of coherent magnetisation switching events, the details of small-scale magnetisation structures, and their associated dynamics, shall bear an increasingly large weight in the overall description of magnetisation motion. In particular, the ratio of lateral surfaces to the element's volume will continue to increase, and the influence of surface effects accordingly. Therefore, the damping characteristics of boundary surfaces might start to play a significant role in the detailed features of energy dissipation in the aftermath of switching. In this context, the work of Bailey and coworkers [57] on the control of magnetisation dynamics through the tailoring of the volume damping parameter should be mentioned. A precise understanding of the energy damping processes taking place during post-switching magnetisation oscillations is still an open research topic and control of localised out-of-plane magnetisation excursions may promote a really faster post-switching damping.

Micromagnetic simulations have effectively paved the way for the first experimental setups aimed at a time-monitoring of coherent magnetisation dynamics in submicron-sized platelets and several research groups are now in a position to produce the needed experimental feedback to proposed switching mechanisms and their characteristics [17, 18]. A fruitful dialogue is now starting between the worlds of simulations and experiments which should prove beneficial to both.

In a rather different register, following the pioneering works of Berger [58] and Slonczewski [59], recent experimental data have demonstrated the feasibility of inducing mag-

netisation reversal by the injection of a spin-polarised current through a thin ferromagnetic layer (for the latest references see [60, 61, 62]). Unfortunately, they all apply to the quasi-static regime. As for simulation data, only in the macrospin approximation has an attempt been made at exploring the dynamics of spin-injection-mediated magnetisation switching [63]. During this thesis' work, we started to expand the scope of these preliminary works and tackle the question of spin injection dynamics in inhomogeneous magnetisation distributions [64]. In a low current regime [to be published], magnetisation switching is found to occur after the development of highly coherent magnetisation oscillations arising from what could be called a pumping mechanism under the combined action of the spin injection torque and demagnetising effects due to out-of-plane excursions. Again, the role of precessional-driven motion is essential in the characterisation of magnetisation dynamics.

As lateral dimensions continue to be decreased, a considerable amount of attention will no doubt start to be paid to the effects of thermal fluctuations. This will perhaps, from a strictly numerical micromagnetics' viewpoint, be the next major direction where to bend all one's attention.

Appendix A

Numerical Methods

Throughout this thesis' chapters the reader has been frequently directed to the appendices with the aim of allowing for the main text to focus on the physical contents embedded in micromagnetism, rather than on its numerical aspects. In the following, a coherent, although brief, account of algorithm implementation will be given. We shall, however, not be concerned with an exhaustive account of numerical procedures, but rather with the innovative contributions developed during this work. These are essentially centred around the *quantification* of time domain errors associated with the accuracy of numerical integration schemes for the LLG equation, along with the assertion of the physical validity of micromagnetic simulation data.

A.1 Computational Schemes

Discussions on the validity of numerical micromagnetic simulations invariably aver the prime role played by both length and time scales. In this respect, the question of edge singularities in static micromagnetics proves emblematic [65]. When considering a magnetic body where sharp edges or corners exist the demagnetising field at the surfaces may become infinite. Such diverging demagnetising fields were found to be compensated by equally diverging exchange fields. This apparent paradox of diverging exchange fields produced by smooth magnetisation distributions has been solved by Thiaville and coworkers [56] in a two- and three-dimensional analytical study of corner singularities. As a crude summary of these works we can state the following: The balancing of diverging fields is done at a length scale corresponding to the familiar exchange length Λ. Therefore, by imposing spatial discretisation values smaller than the exchange length, correct numerical calculations

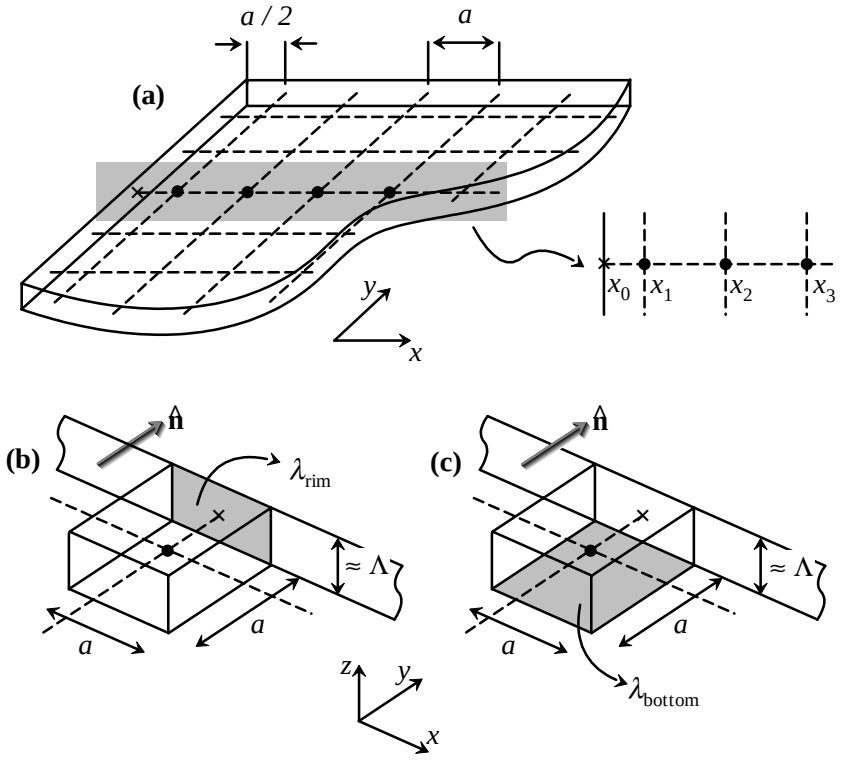

Figure A.1: Two-dimensional grid used in simulations. Calculation points are explicitly represented by dots (note that none belong to boundary surfaces).

are possible as long as one avoids the explicit evaluation of exchange and magnetostatic fields at sharp edges or corners (either two- or three-dimensional).

It seems, therefore, a harsh task to conciliate the correct imposition of the boundary conditions associated with the micromagnetic governing equations (see Sects. 1.2.2 and 1.2.3) and the impossibility of explicitly evaluating effective field components at the very same surfaces. When considering thin magnetic platelets (restricted in shape to perfectly defined rectangles), the solution proposed in this work relies on the partitioning of the volume into a regular array of parallelepiped cells (see Fig. A.1). Due to the small thickness values considered in this work, a single layer of volume cells was solely needed in the thickness. Magnetisation grid points are located at the geometric centre of such cells, in a one-to-one correspondence, so that all are strictly in the interior of the platelet. In addition, such a grid will also define the evaluation locus for all volume or surface contributions to the effective field. In this way, every magnetisation point is subjected to the exactly evaluated effective field at the same spatial location, which corresponds to what might be called a grid-field approach. In particular, no average of effective field

components is made over the cell volumes. Although no magnetisation grid points belong to the surfaces of the platelet, the correct imposition of boundary constraints is attained through a local fourth-order Taylor expansion of $\mathbf{m}$, as shown in the following section.

The question of determining if grid-field approaches are better suited for an accurate description of magnetisation dynamics still remains an open question. Only detailed comparison between numerical codes will no doubt elucidate this question. Here, we want only to underline the *consistency* of such methods.

A.1.1 Statics

Static micromagnetic calculations rely on solving Brown's equations. Using the set of reduced (dimensionless) units introduced in Sect. 1.3, in their most simplest form (no surface interactions), Brown's equations read

$$\mathbf{m} \times \mathbf{h}_{\text{eff}} = 0 \quad \text{with} \quad \frac{\partial \mathbf{m}}{\partial \hat{\mathbf{n}}} = 0 \quad , \tag{A.1}$$

$$\mathbf{h}_{\text{eff}} = \Lambda^2 \left(\nabla^2 \mathbf{m} \right) + \mathbf{h}_d + \mathbf{h}_a - \frac{\delta w_{\text{ani}}}{\delta \mathbf{m}} \quad . \tag{A.2}$$

The effective field comprises contributions from exchange, demagnetising, applied and anisotropy fields. In the present work, no provision has been made for magnetostriction-related contributions.

In a grid-field approach, the evaluation of exchange interactions requires the computation of the second-order spatial derivatives of $\mathbf{m}$. In finite-difference type methods, low-order expansions of $\mathbf{m}$ are known to provide inaccurate numerical approximations of spatial magnetisation derivatives [66]. In this work, following on with previous implementations [66], the evaluation of second-order spatial derivatives relies on a local fourth-order Taylor expansion of $\mathbf{m}$. Consider a one-dimensional scalar function f. Around the grid point i, its Taylor expansion along x, and that of its first derivative, are given by

$$f(x_j) = \sum_{k=0}^{\infty} \frac{(x_j - x_i)^k}{k!} f^{(k)}(x_i) \quad , \tag{A.3}$$

$$f^{(1)}(x_j) = \sum_{k=1}^{\infty} \frac{(x_j - x_i)^{k-1}}{(k-1)!} f^{(k)}(x_i) \quad . \tag{A.4}$$

For an interior grid point i having two nearest-neighbours on each side, straightforward

use of Eq. (A.3) yields the matrix equation

$$\begin{bmatrix} -2a & (-2a)^2\frac{1}{2!} & (-2a)^3\frac{1}{3!} & (-2a)^4\frac{1}{4!} \\ -a & (-a)^2\frac{1}{2!} & (-a)^3\frac{1}{3!} & (-a)^4\frac{1}{4!} \\ a & (a)^2\frac{1}{2!} & (a)^3\frac{1}{3!} & (a)^4\frac{1}{4!} \\ 2a & (2a)^2\frac{1}{2!} & (2a)^3\frac{1}{3!} & (2a)^4\frac{1}{4!} \end{bmatrix} \cdot \begin{bmatrix} f^{(1)}(x_i) \\ f^{(2)}(x_i) \\ f^{(3)}(x_i) \\ f^{(4)}(x_i) \end{bmatrix} = \begin{bmatrix} f(x_{i-2}) - f(x_i) \\ f(x_{i-1}) - f(x_i) \\ f(x_{i+1}) - f(x_i) \\ f(x_{i+2}) - f(x_i) \end{bmatrix} \quad . \tag{A.5}$$

The equation above can be immediately solved for the $f^{(k)}(x_i)$, obtaining therefore the first, second, third, and fourth derivatives of f at the grid point i. These general expressions can be directly employed in determining the spatial derivatives, along x and y, of every magnetisation component by simply replacing f by m_x, m_y, or m_z. The gradient of $\mathbf{m}$ along z is here nil by construction (see Fig. A.1). In particular, the general form of the second derivative reads

$$f^{(2)}(x_i) = \frac{-f(x_{i-2}) + 16f(x_{i-1}) - 30f(x_i) + 16f(x_{i+1}) - f(x_{i+2})}{12a^2} \quad . \tag{A.6}$$

For grid points sufficiently near the surfaces, such as those with the indices 1 or 2 in Fig. A.1**a**, Eq. (A.5) cannot be used since at least one grid point will be missing on the left of point i. The special nature of near-surface grid points may, however, be utilised in enforcing the boundary conditions associated with Brown's equations. Although the working principle of the method can be found in the work of Labrune and Miltat [67], explicit expressions of such calculation will be reproduced here in order to stress the fact that magnetisation points are now defined at the cell's centre. Supplementary equations must be found to replace the missing ones. These are to be found through the use of Eq. (A.4). For $i = 2$, Eq. (A.5) becomes

$$\begin{bmatrix} 1 & \frac{(-3a/2)^1}{1!} & \frac{(-3a/2)^2}{2!} & \frac{(-3a/2)^3}{3!} \\ -a & \frac{(-a)^2}{2!} & \frac{(-a)^3}{3!} & \frac{(-a)^4}{4!} \\ a & \frac{(a)^2}{2!} & \frac{(a)^3}{3!} & \frac{(a)^4}{4!} \\ 2a & \frac{(2a)^2}{2!} & \frac{(2a)^3}{3!} & \frac{(2a)^4}{4!} \end{bmatrix} \cdot \begin{bmatrix} f^{(1)}(x_2) \\ f^{(2)}(x_2) \\ f^{(3)}(x_2) \\ f^{(4)}(x_2) \end{bmatrix} = \begin{bmatrix} f^{(1)}(x_0) \\ f(x_1) - f(x_2) \\ f(x_3) - f(x_2) \\ f(x_4) - f(x_2) \end{bmatrix} \quad , \tag{A.7}$$

while for $i = 1$ only three equations must be considered, yielding

$$\begin{bmatrix} 1 & \frac{(-a/2)^1}{1!} & \frac{(-a/2)^2}{2!} \\ \frac{(a)}{1} & \frac{(a)^2}{2!} & \frac{(a)^3}{3!} \\ \frac{(2a)}{1} & \frac{(2a)^2}{2!} & \frac{(2a)^3}{3!} \end{bmatrix} \cdot \begin{bmatrix} f^{(1)}(x_1) \\ f^{(2)}(x_1) \\ f^{(3)}(x_1) \end{bmatrix} = \begin{bmatrix} f^{(1)}(x_0) \\ f(x_2) - f(x_1) \\ f(x_3) - f(x_1) \end{bmatrix} \quad . \tag{A.8}$$

In particular, the expression for the second derivative becomes then

$$f^{(2)}(x_1) = -\frac{24}{23}\frac{f^{(1)}(x_0)}{a} + \frac{-25f(x_1) + 26f(x_2) - f(x_3)}{12a^2} \quad . \tag{A.9}$$

In Eqs. (A.7) and (A.8), the boundary condition in Brown's equations is explicitly enforced when evaluating exchange interactions *even if no magnetisation grid point lies on the surface*. The equations above are directly usable in the presence of interlayer exchange interactions (or more generally any surface anisotropy contribution), through the direct evaluation of $f^{(1)}(x_0)$ in the equations above.

In accordance with the grid-field method outlined in the introductory text of this section, the magnetostatic field is evaluated pointwise, at the centre of each volume cell, through a direct use of

$$\mathbf{h}_d(\mathbf{r}) = \frac{1}{4\pi}\left[\int_\Omega \frac{(\mathbf{r}-\mathbf{r}')\rho(\mathbf{r}')}{|\mathbf{r}-\mathbf{r}'|^3}d\mathbf{r}' + \int_\Gamma \frac{(\mathbf{r}-\mathbf{r}')\lambda(\mathbf{r}')}{|\mathbf{r}-\mathbf{r}'|^3}d\mathbf{r}'\right] \quad , \tag{A.10}$$

with

$$\rho(\mathbf{r}') = -\boldsymbol{\nabla}\cdot\mathbf{m} = -\left(\frac{\partial m_x}{\partial x} + \frac{\partial m_y}{\partial y}\right) \quad , \tag{A.11}$$

$$\lambda(\mathbf{r}') = \mathbf{m}\cdot\hat{\mathbf{n}} \quad , \tag{A.12}$$

the volume and surface magnetic charges, respectively. Let G denote the Green's function associated with Poisson's equation

$$G(\mathbf{r}-\mathbf{r}') = \frac{1}{4\pi}\frac{1}{|\mathbf{r}-\mathbf{r}'|} \quad . \tag{A.13}$$

Equation (A.10) may be easily understood as a convolution product of the kernel function $\boldsymbol{\nabla}_{r'}G$ and both the volume and surface charges

$$\mathbf{h}_d(\mathbf{r}) = \left[\boldsymbol{\nabla}_{r'}G(\mathbf{r}-\mathbf{r}')\otimes\rho(\mathbf{r}') + \boldsymbol{\nabla}_{r'}G(\mathbf{r}-\mathbf{r}')\otimes\lambda(\mathbf{r}')\right] \quad . \tag{A.14}$$

The convolution theorem provides for an efficient way of calculating the convolution product above. Let $\mathcal{F}$ denote the Fourier transform and $\mathcal{F}^{-1}$ its inverse. The convolution product $\boldsymbol{\nabla}_{r'}G\otimes\rho$ can be calculated by

$$\boldsymbol{\nabla}_{r'}G\otimes\rho = \mathcal{F}^{-1}(\mathcal{F}(\boldsymbol{\nabla}_{r'}G)\mathcal{F}(\rho)) \quad . \tag{A.15}$$

The fourth-order expansions of in-plane components of magnetisation, along both x and y, needed in the evaluation of exchange interactions, also provide for the values of the first-order spatial derivatives of $\mathbf{m}$ at every grid point i. The volume magnetic charges $\rho(\mathbf{r}')$ are

thus readily available. These values are assumed to be constant inside the corresponding volume cell. The use of a single layer of volume cells, and, accordingly, of magnetisation points in the thickness, immediately provides for the values of top and bottom surface magnetic charges (λ_{top} and λ_{bottom}). However, the evaluation of rim charges (λ_{rim}) requires the knowledge of $\mathbf{m}$ at lateral surfaces, which are not immediately available due to the mesh used (see Figs. A.1**b** and A.1**c**). These are to be found through the use, again, of the aforementioned expansions, consistent with boundary conditions. The values of λ_{top}, λ_{bottom}, and λ_{rim} are considered as constants over the corresponding cell surfaces.

Following the grid-field approach outlined above, the discretised equivalent of Eq. (A.10), or Eq. (A.14), may be written as the discrete convolution products

$$\mathbf{h}_d(\mathbf{r}_i) = \sum_j \rho(\mathbf{r}_j) \int_{\Omega_{\text{cell}}} \boldsymbol{\nabla}_{\mathbf{r}'} G(\mathbf{r}_i - \mathbf{r}') d\mathbf{r}' + \sum_k \lambda(\mathbf{r}_k) \int_{\Gamma} \boldsymbol{\nabla}_{\mathbf{r}'} G(\mathbf{r}_i - \mathbf{r}') d\mathbf{r}' \quad . \tag{A.16}$$

Fast Fourier Transform (FFT) methods can therefore be implemented in order to speed-up the evaluation of the demagnetising fields [68, 69, 70, 71]. The use of such techniques reduce the number of computations needed for N grid points from $2N^2$ to $2N \log_2 N$, where $\log_2$ is the base-2 logarithm [72].

Applied and anisotropy field contributions to $\mathbf{h}_{\text{eff}}$ (or, for that matter, stray fields), being strictly local, are straightforwardly implemented through an explicit evaluation of analytical expressions at every grid point.

When dealing with static problems, following the work of Trouilloud and Miltat [66], which proved to be a significant improvement over the original LaBonte calculation [73], magnetisation rotation towards the direction of the effective field is performed at each computational cycle through a discrete overdamped LLG equation

$$\Delta\mathbf{m} = -\alpha'[\mathbf{m} \times (\mathbf{m} \times \mathbf{h}_{\text{eff}})] \quad . \tag{A.17}$$

The damping parameter α' does not necessarily posses any physical meaning. Its use is here that of an adjustable parameter allowing for the swiftest possible convergence rate. Values typically range from 0.1 to 0.5. Note that, when converging low remanence magnetisation configurations in very thin films, calculations frequently diverge for α' values greater than 0.25. Although Eq. (A.17) guarantees that $\mathbf{m} \cdot \Delta\mathbf{m} \equiv 0$ this condition is only equivalent to $\|\mathbf{m}\| \equiv 1$ to first order in $\mathbf{m}$. Therefore, after each rotation step, magnetisation vectors at

each grid point are explicitly renormalised. Convergence is achieved, and the calculation stopped, when the maximum value of the reduced torque's norm drops below predefined values, usually

$$\max \|\mathbf{m} \times \mathbf{h}_{\text{eff}}\| < 10^{-6} \quad . \tag{A.18}$$

Nowhere, during a full algorithm cycle, does one requires the explicit evaluation of specific energy terms. For the single purpose of monitoring, the different contributions to the energy were calculated using a very simple approach. Since every contribution to the effective field is explicitly evaluated at every magnetisation grid point, using the energy density expressions presented in Chap. 1, the pointwise energy density may immediately be found. This value is assumed to be a constant throughout the corresponding cell volume leading to the total energy values given in the main text. Even though our energy evaluation method might appear crude, Eq. (A.18) is in most cases supplemented by a close monitoring of energy values: Only when each energy component becomes sufficiently stable is convergence attained.

Validation

The validation of micromagnetic codes seems to elude a straightforward set of procedures. Apart from the direct comparison of total energy values, or effective field values at selected locations (for magnetisation distributions allowing for an analytical evaluation of energy or fields), the only generally agreed procedure is based on some sort of asymptotic analysis, in particular as a function of decreasing mesh parameters. In so doing precision is replaced by accuracy. The reader should not be deceived by this statement. Indeed, what are the guarantees that a correct energy evaluation for a uniformly magnetised body should produce the same degree of precision when the magnetisation distribution becomes highly non-uniform? Generally, the answer is not known a priori.

Plain common sense is almost the most reliable procedure available: For how can we pretend to an accurate description of a given micromagnetic distribution (e.g. a vortex) if the mesh spacing value is not beyond the characteristic value of micromagnetic structures, i.e. the exchange length Λ in soft magnetic materials (see Fig. A.2)? In Fig. A.3, we present the convergence analysis of the different energy contributions as a function of grid spacing for a Permalloy platelet in an initial S state. This set of results presents a clear plateau in the limit of an infinitely small grid spacing. A similar behaviour (which

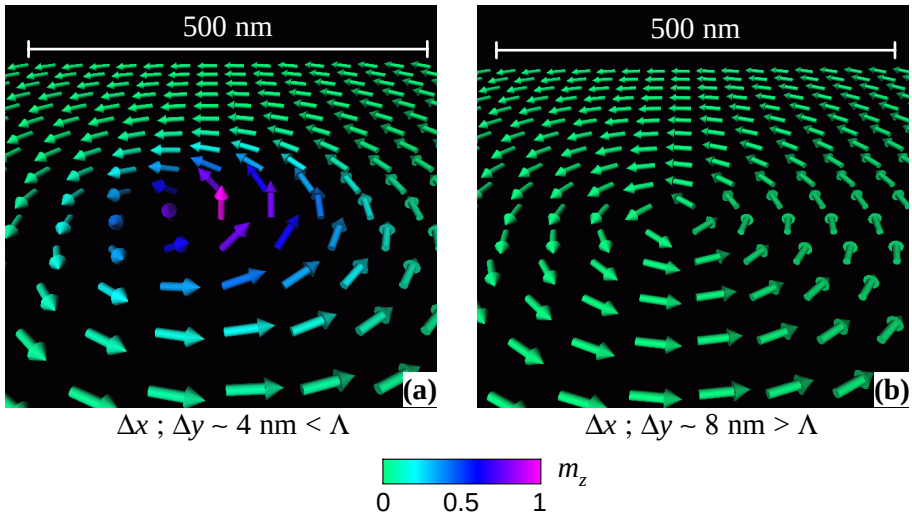

Figure A.2: (Colour) Vortex definition in a square, 10 nm thick, Permalloy platelet. **(a)** Full details of the out-of-plane magnetisation distribution are obtained for mesh spacing values smaller than the characteristic length of the material (exchange length Λ) in contrast with **(b)**. Note that the vectors displayed do not correspond to actual mesh points.

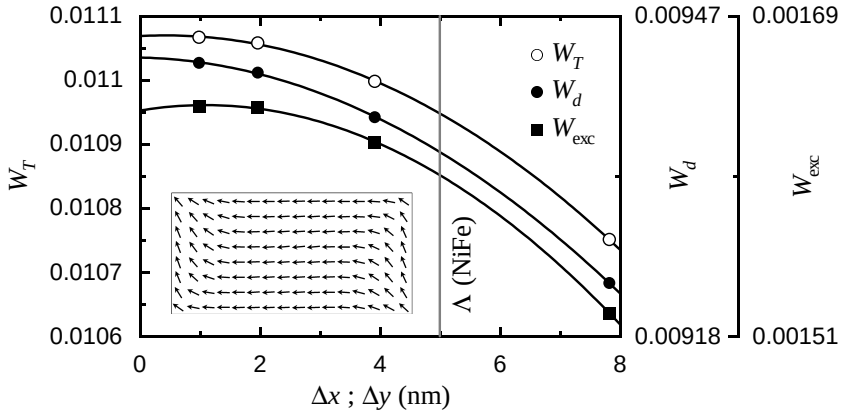

Figure A.3: Static energy convergence versus grid spacing for an S state magnetisation distribution in a Permalloy platelet of dimensions $500 \times 250 \times 5$ nm^3. The lines shown are just guides to the eye.

looks reasonable when Δx tends to zero) has also been observed by Rave and Hubert [39]. It seems, nevertheless, that averaging procedures do not always comply with this rule of thumb, and energy convergence versus grid spacing can, in some cases, be a linear function of the spatial discretisation values used (see App. B).

A.1.2 Dynamics

Magnetisation motion is commonly assumed to derive from the LLG equation (Sect. 1.2.3). Using the reduced (dimensionless) system of units introduced in Sect. 1.3, this equation reads

$$(1+\alpha^2)\frac{\partial \mathbf{m}}{\partial \tau} = -(\mathbf{m}\times\mathbf{h}_{\text{eff}}) - \alpha\,[\mathbf{m}\times(\mathbf{m}\times\mathbf{h}_{\text{eff}})] \quad . \tag{A.19}$$

As already stressed in Chap. 1, although not commonly stated in the literature, Brown's boundary constraint on $\mathbf{m}$ remains valid for the LLG equation: The same variational procedures used in obtaining Eqs. (1.40) and (1.41) are employed when deriving the gyromagnetic equations (and the LLG equation, accordingly) from Hamilton's principle. In the framework of dynamical micromagnetics, the constraint of stationary magnetisation at free surfaces, is fully implemented through the procedures described in Sect. A.1.1.

Equation (A.19) represents a set of stiff differential equations, especially in the limit of small α values [74, 75]. *Therefore, addressing the issue of numerical stability lead us to the adoption of a Crank-Nicolson integration scheme* [72]. In its most simple expression this numerical integration method can be viewed as a centred average between a forward (explicit) and a backward (implicit) differencing schemes.

Setting $\mathbf{h}'_{\text{eff}} = \mathbf{h}_{\text{eff}} + \alpha\,(\mathbf{m}\times\mathbf{h}_{\text{eff}})$ the LLG equation simply reads

$$(1+\alpha^2)\frac{\partial \mathbf{m}}{\partial \tau} = -\left(\mathbf{m}\times\mathbf{h}'_{\text{eff}}\right) \quad . \tag{A.20}$$

In a forward scheme the right-hand side is evaluated at τ, while for a backward scheme the evaluation is made at $\tau+\Delta\tau$, namely

$$\text{Forward} \qquad (1+\alpha^2)\frac{\Delta \mathbf{m}}{\Delta \tau} = -\left(\mathbf{m}\times\mathbf{h}'_{\text{eff}}\right)_{\tau} \quad , \tag{A.21}$$

$$\text{Backward} \qquad (1+\alpha^2)\frac{\Delta \mathbf{m}}{\Delta \tau} = -\left(\mathbf{m}\times\mathbf{h}'_{\text{eff}}\right)_{\tau+\Delta\tau} \quad , \tag{A.22}$$

with $\Delta\mathbf{m} = \mathbf{m}_{\tau+\Delta\tau} - \mathbf{m}_{\tau}$. In both cases, the time derivative term is simply represented by a forward Euler differencing, a designation employed only for time derivatives. Since Eq. (A.19) preserves the norm of $\mathbf{m}$ at every instant τ, to first-order, the discretised expressions above should comply with $\mathbf{m}\cdot\Delta\mathbf{m} = 0$, namely

$$-\mathbf{m}\cdot\left(\mathbf{m}\times\mathbf{h}'_{\text{eff}}\right) = 0 \quad , \tag{A.23}$$

$$-\left[\mathbf{m}\cdot\left(\Delta\mathbf{m}\times\mathbf{h}'_{\text{eff}}\right) + \mathbf{m}\cdot\left(\mathbf{m}\times\Delta\mathbf{h}'_{\text{eff}}\right) + \mathbf{m}\cdot\left(\mathbf{m}\times\mathbf{h}'_{\text{eff}}\right)\right] = 0 \quad . \tag{A.24}$$

The last two terms on the left-hand side of the last equation are, by definition, nil. Following the arguments of Nakatani and coworkers [76], all discretised terms not satisfying the first-order constraint $\mathbf{m} \cdot \Delta\mathbf{m} = 0$, i.e. $(\Delta\mathbf{m} \times \mathbf{h}'_{\text{eff}})$ will be excluded from the integration scheme. Accordingly, a numerical implementation of Eq. (A.19) may be written as

$$\begin{aligned}(1+\alpha^2)\frac{\Delta\mathbf{m}}{\Delta\tau} &= -\frac{1}{2}\left(2\mathbf{m}\times\mathbf{h}'_{\text{eff}} + \mathbf{m}\times\Delta\mathbf{h}'_{\text{eff}}\right) \\ &= -\mathbf{m}\times\mathbf{h}'_{\text{eff}} - \frac{1}{2}\mathbf{m}\times\Delta\mathbf{h}'_{\text{eff}} \quad .\end{aligned} \tag{A.25}$$

Expanding the double vector products in the equation above, and making use of the norm constraint $\mathbf{m}\cdot\mathbf{m} \equiv 1$ and of the vector triple product identity[(a)], eventually leads to

$$\left[\frac{1+\alpha^2}{\Delta\tau} + \frac{1}{2}\alpha(\mathbf{m}\cdot\mathbf{h}_{\text{eff}})\right]\Delta\mathbf{m} + \frac{1}{2}\mathcal{D}(\Delta\mathbf{h}_{\text{eff}}) = -\mathcal{D}(\mathbf{h}_{\text{eff}}) \quad , \tag{A.26}$$

with $\mathcal{D}(\mathbf{u}) = \mathbf{m}\times\mathbf{u} + \alpha\left[(\mathbf{m}\cdot\mathbf{u})\mathbf{m} - \mathbf{u}\right]$[(b)]. By expressing $\Delta\mathbf{h}_{\text{eff}}$ as a set of *linear* equations in $\Delta\mathbf{m}$, Eq. (A.26) can be stated in the condensed matrix form

$$\mathsf{A}\cdot\Delta\mathbf{m} = \mathsf{b} \quad , \tag{A.27}$$

where all implicit contributions to the integration scheme are included in A and b is simply the discretised version of $-\mathcal{D}(\mathbf{h}_{\text{eff}})$.

Since all the explicit contributions of Eq. (A.19) (right-hand side) are included in the vector b (which is evaluated using no other approximations than those arising from the spatial discretisation procedures employed), the contents of the matrix A are uniquely dependent upon mathematical considerations. In fact, although explicit schemes are in reality poor numerical procedures, leading, as we shall see, to an almost immediate numerical breakdown, they do contain all the physics described by the LLG equation. Therefore, extensions made to this numerical integration scheme are simply a matter of mathematical convenience. In particular, we are at liberty to drop particular discretised terms, as done in [76], or, indeed, as shall be seen in the following, to include only selected contributions to the effective field.

Of particular importance is the handling of demagnetising interactions. Since $\mathbf{h}_d$ at any given point $\mathbf{r}$ depends on the whole of the magnetic body, the complete inclusion of demagnetising interactions in the implicit terms in Eq. (A.26) would result in a fully populated matrix. Even for a reasonably small problem involving 127×63 grid points,

[(a)] $\mathbf{A}\times(\mathbf{B}\times\mathbf{C}) = \mathbf{B}(\mathbf{A}\cdot\mathbf{C}) - \mathbf{C}(\mathbf{A}\cdot\mathbf{B})$

[(b)] $\mathcal{D}(\mathbf{u}) = \mathbf{m}\times\mathbf{u} + \alpha\left[(\mathbf{m}\cdot\mathbf{u})\mathbf{m} - \mathbf{u}\right] = \mathbf{m}\times\mathbf{u} + \alpha\left[\mathbf{m}\times(\mathbf{m}\times\mathbf{u})\right]$

this would amount to the storing (in native 64-bit machines) of a matrix of more than 4 GB (not to speak of the cost of inverting it at each calculation time step)! Choices must clearly be made. In general, a reduced number of nearest-neighbours is taken as acting on a given magnetisation grid point. This generally leads to the assembling of a banded sparse matrix structure, especially when sequentially numbering the magnetisation grid points componentwise (see Fig. A.4). Again, let us stress the solely mathematical meaning of the inclusion (or removing) of terms. In addition, from a physical viewpoint, the inclusion of demagnetising terms tends to favour a strong magnetisation antiparallel alignment between neighbouring spins.

A further simplification derives from considering just exchange contributions when assembling the matrix A. The sparse matrix structure arising from the sole inclusion of exchange contributions is shown in Fig. A.4. For each block corresponding to the three components of magnetisation, the matrix A displays a highly regular band structure. Indeed, exchange interactions couple only those grid locations lying on orthogonal directions and being first or second nearest-neighbours. Due to the fact that the correct boundary conditions were explicitly included when evaluation second-order derivatives at grid points near the edges, the given matrix is, unfortunately, not symmetric (comparing Eqs. (A.6) and (A.9) immediately displays the symmetry breaking between, for instance, grid locations 1 and 3). Accordingly, a Generalised Minimum RESidual (GMRES) method was used at each iteration step to solve for $\Delta\mathbf{m}$ in Eq. (A.27) (see [72] and original references therein). Full use of the sparse nature of A has therefore been made, since the GMRES method only relies on matrix-vector multiplication operations.

Although, here, a detailed analysis of the spectral properties of the matrix A will not be made, it is worthwhile to further discuss an additional point. If the nonzero structure of A has been given in Fig. A.4, nothing has been said about the values there stored. Surprisingly enough, the main diagonal entries are consistently three orders of magnitude higher than any off-diagonal values. Indeed, main diagonal entries are almost completely determined by the value of the term $(1+\alpha^2)/\Delta\tau$ in Eq. (A.26) arising from the explicit contribution to the Crank-Nicolson scheme, which, for the small α values considered is simply the inverse of the time step value used. Implicit contributions, even for the main diagonal entries, stand only for small corrections. Nevertheless, they do provide for the necessary stabilisation of the iterative procedure (vide infra). The question remains as to determine if the self-contributions (those corresponding to the main diagonal entries)

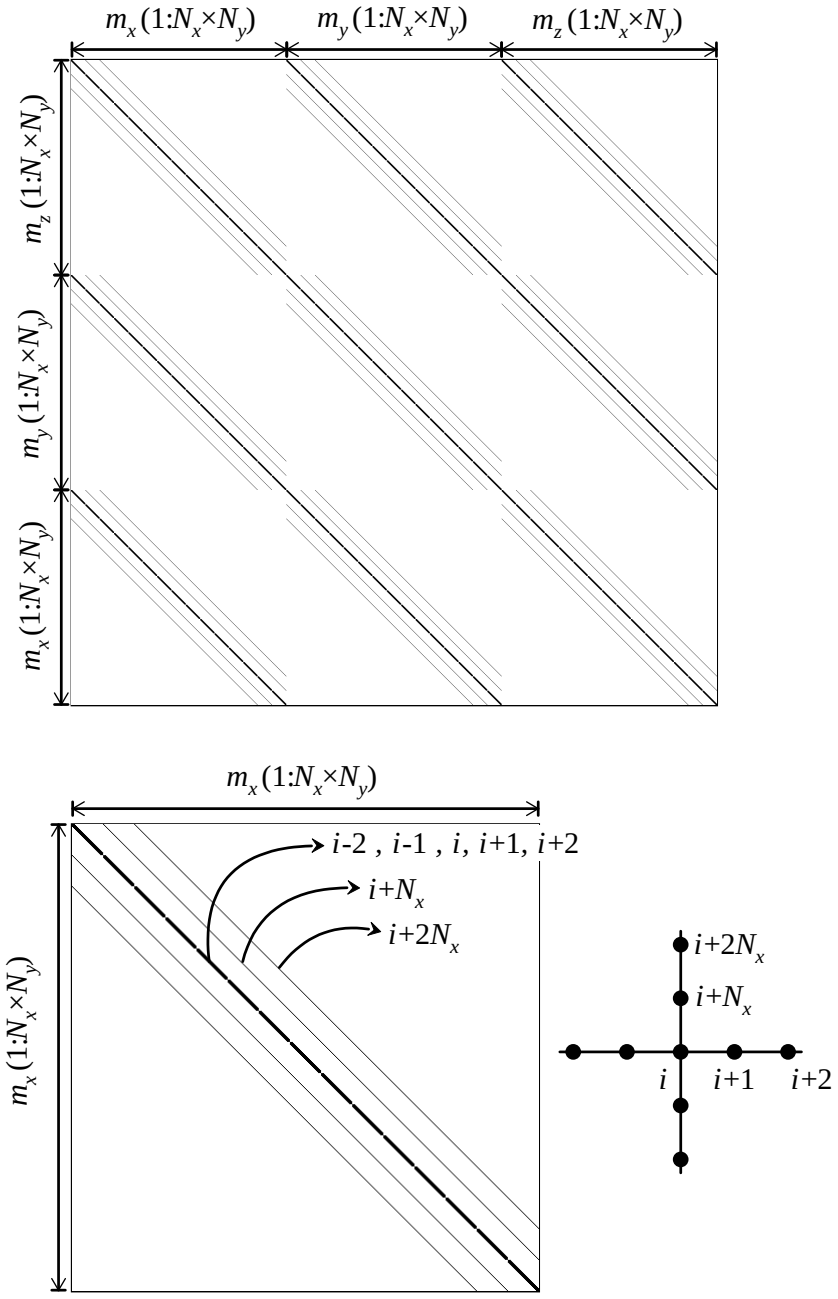

Figure A.4: Sparse matrix structure arising from the sole inclusion of exchange interactions in the implicit contributions to the Crank-Nicolson scheme. N_x and N_y denote the number of grid points along x and y, respectively.

deriving from the implicit terms are actually capable of producing the same degree of stabilisation. If such was to be the case, then only the main diagonal needs to be taken into account, therefore notably speeding up the overall calculation of $\mathbf{\Delta m}$, since solving Eq. (A.27) would be trivial. This is still to be further explored.

von Neumann Stability Analysis

Ensuring numerical stability comes, nonetheless, at a cost, namely the trade-off between stability and both precision and accuracy. If numerical precision is nowadays easily guaranteed through the use of widely available 64-bit computational resources, accuracy must still be controlled. In particular, the allowed time steps values must be established. Since, within their stability limits, explicit integration schemes are known to maintain a high level of accuracy, their stability analysis should provide for a lower bound for the maximum values of Δt. Since the onset of numerical instabilities in micromagnetic calculations occurs over small length scales, and this even for highly uniform magnetisation distributions, the use of simple, albeit effective, local stability analyses seems justified. These are due to von Neumann (see [72] and [77]).

In a direct analogy with the stability analysis of diffusion equations, the Laplacian operator representing exchange interactions is usually regarded as the most likely source of numerical instabilities. Considerer for simplicity the one-dimensional linearised LLG equation governed by exchange. In the limit of small perturbations from a uniformly magnetised distribution aligned along the z axis, first-order expressions may be written for $\mathbf{m}$ and $\mathbf{h}_{\text{exc}}$ as

$$\mathbf{m} = \begin{bmatrix} m_x \\ m_y \\ 1 \end{bmatrix} \quad \text{and} \quad \mathbf{h}_{\text{exc}} = \Lambda^2 \begin{bmatrix} \nabla^2 m_x \\ \nabla^2 m_y \\ 0 \end{bmatrix} \quad . \tag{A.28}$$

The linearised LLG equation then becomes

$$\left(1+\alpha^2\right) \frac{\partial \mathbf{m}}{\partial \tau} = \Lambda^2 \begin{bmatrix} \alpha \nabla^2 m_x + \nabla^2 m_y \\ -\nabla^2 m_x + \alpha \nabla^2 m_y \\ 0 \end{bmatrix} \quad . \tag{A.29}$$

Introducing the complex variable $u = m_x + \imath m_y$, conveniently allows to rewrite the equation above as

$$\left(1+\alpha^2\right) \frac{\partial u}{\partial \tau} = \Lambda^2 \left(\alpha - \imath\right) \nabla^2 u \quad , \tag{A.30}$$

which is just a diffusion equation with a constant (albeit complex) parameter.

Let u_j^n denote $u(x_j, t_n)$. The obvious, and most widely used, way of representing the time derivative in Eq. (A.30) is through the so-called forward Euler differencing equation

$$\left.\frac{\partial u}{\partial \tau}\right|_{j,n} = \frac{u_j^{n+1} - u_j^n}{\Delta t} \quad . \tag{A.31}$$

From the matrix equation (A.6) we obtain

$$\left.\frac{\partial^2 u}{\partial x^2}\right|_{j,n} = \frac{-u_{j-2}^n + 16u_{j-1}^n - 30u_j^n + 16u_{j+1}^n - u_{j+2}^n}{12a^2} \quad . \tag{A.32}$$

This finite-difference approximation to Eq. (A.30) is simply a fourth-order FTCS (Forward Time Centred Space) representation.

The von Neumann stability analysis assumes independent solutions of the difference equations above of the form

$$u_j^n = \xi^n(k) e^{\imath kja} \quad . \tag{A.33}$$

The amplification factor $\xi(k)$, can be found by simply substituting Eq. (A.33) back into Eq. (A.32). Dividing by ξ^n, yields

$$\xi(k) = 1 + \frac{\Lambda^2 (\alpha - \imath)\,\Delta\tau}{(1+\alpha^2)} \frac{32\cos(ka) - 2\cos(2ka) - 30}{12a^2} \quad . \tag{A.34}$$

Using the double-angle trigonometric identities, the equation above transforms into

$$\xi(k) = 1 - \frac{4\Lambda^2 (\alpha - \imath)\,\Delta\tau}{(1+\alpha^2)\,a^2} \sin^2(\frac{ka}{2}) \left[1 + \frac{1}{3}\sin^2(\frac{ka}{2})\right] \quad , \tag{A.35}$$

and the stability condition $|\xi(k)| \leq 1$ yields

$$\Delta\tau \leq \frac{3}{4}\frac{\alpha}{2}\left(\frac{a}{\Lambda}\right)^2 \quad . \tag{A.36}$$

The factor 3/4 is the immediate consequence of using Eq. (A.32) instead of a simpler second-order formula for the second-order spatial derivatives: A small price to pay for the added precision. Extending the above analysis for a two-dimensional space with the same discretisation step a is trivial, leading to

$$\Delta\tau \leq \frac{3}{8}\frac{\alpha}{2}\left(\frac{a}{\Lambda}\right)^2 \quad . \tag{A.37}$$

For the material parameters employed during this work, namely those of Permalloy, the largest time step Δt must conform to values smaller than ≈ 6.6 fs for $a = 4$ nm. A similar analysis for the Crank-Nicolson scheme would reveal it unconditionally stable for any Δt value.

A.2 α Monitoring

Self-Consistency, Quantitative Error Measurement, and Numerical Breakdown

The mathematical stability of numerical integration schemes, such as the one proposed above, should not be regarded as a statement of the physical meaningfulness of simulated

data. If the need for controlling the allowed time step values is well recognised in the literature, only empirical estimations could be made so far [75]. On the other hand, the development of self-consistency criteria has received considerable attention since the early days of micromagnetics [22]. Recently, we have introduced a first self-consistency criterion for the solution of the LLG equation [78, 79]. This criterion provides for quantitative error measurements even in situations where the mathematical stability of the integration scheme is not challenged.

Disregarding the damping contribution to the LLG equation, a constant applied field can only be responsible for a precessional motion of magnetisation which leaves the energy constant. Inversely, the energy rate of change is necessarily a function of the damping parameter α. Starting from the general expression of the system's free energy functional, the total energy rate of change can be written as (see Sect. 1.2.3)

$$\frac{dW}{d\tau} = -\alpha \int_{\Omega} \left(\frac{\partial \mathbf{m}}{\partial \tau} \right)^2 d\mathbf{r} \quad . \tag{A.38}$$

Although there is no local counterpart to this equation (except in the macrospin approximation), the LLG equation allows to write an expression connecting, at every grid point, the effective field to the rate of change of magnetisation (see Sect. 1.2.3, Eq. (1.55))

$$\mathbf{h}_{\text{eff}} \cdot \frac{\partial \mathbf{m}}{\partial \tau} = \alpha \left(\frac{\partial \mathbf{m}}{\partial \tau} \right)^2 \quad . \tag{A.39}$$

Both Eq. (A.38) and Eq. (A.39) allow for the recalculation of the damping parameter α during magnetisation motion. In particular, through an average of Eq. (A.39), the value of α can be recalculated without the need to evaluate the system's total energy. Given the arguments presented earlier this is the most error-free procedure available to us and it was the one implemented in the code.

The proposed numerical integration scheme was then validated through a set of transverse oscillation experiments, similar to those presented in Chap. 3. In these, a Permalloy platelet of dimensions $500 \times 250 \times 5$ nm^3 (in an initial S state) is subjected to a sole transverse (y-directed) field step, the intensity of which was chosen so as to generate a strong oscillatory motion without inducing switching. The average magnetisation curves are shown in Fig. A.5, along with two magnetisation distribution snapshots corresponding to the first oscillation extrema. The recalculated damping parameter α_{dyn} was continuously monitored as a function of time as shown in Fig. A.5**d** along with its macrospin

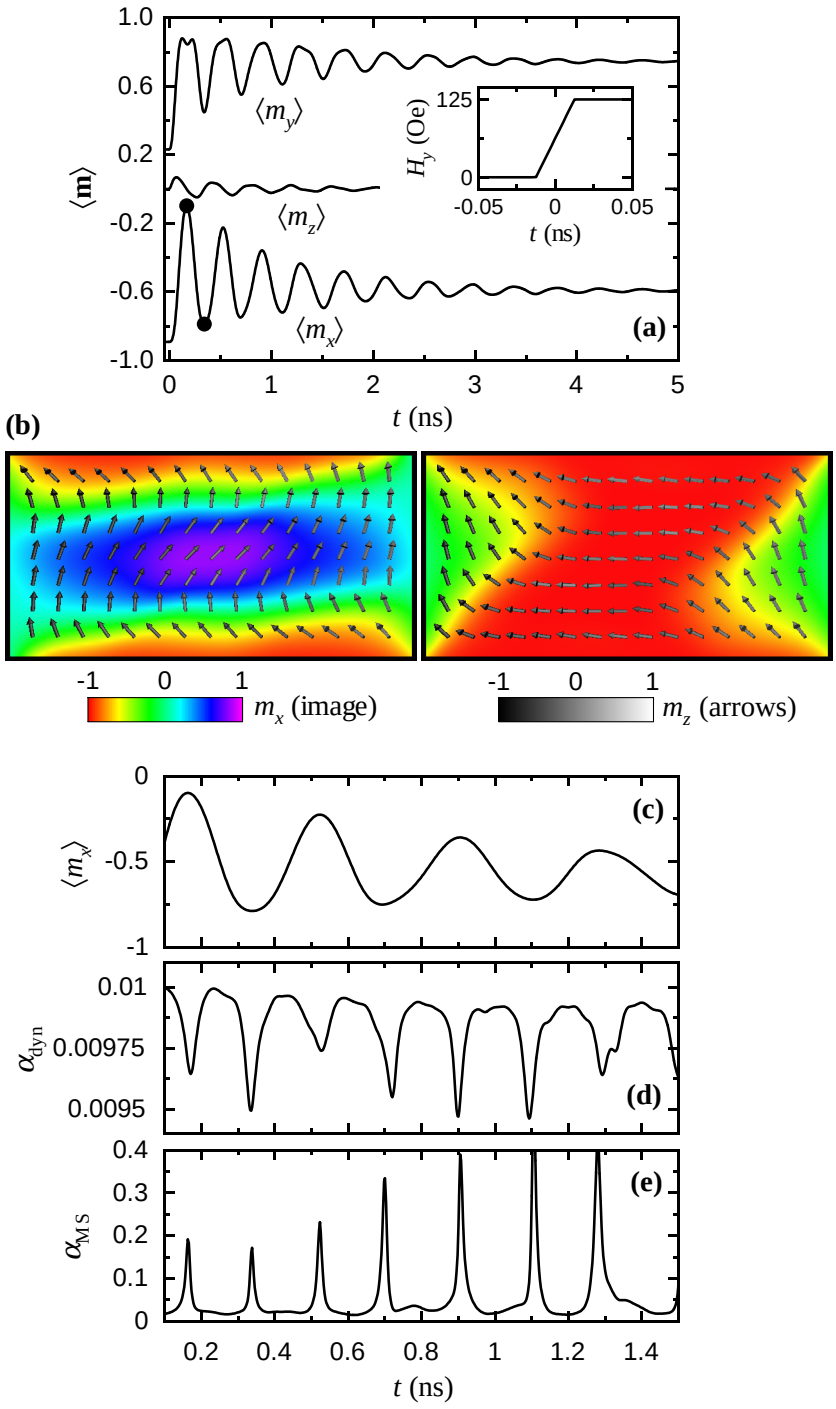

Figure A.5: (Colour) **(a)** Average magnetisation components evolution for a transverse oscillations test simulation. The dots displayed on top of the average x magnetisation component represent the extremum magnetisation distributions during oscillation and are represented in **(b)**. **(c)**–**(e)** Longitudinal average magnetisation component and recalculated α values as a function of time.

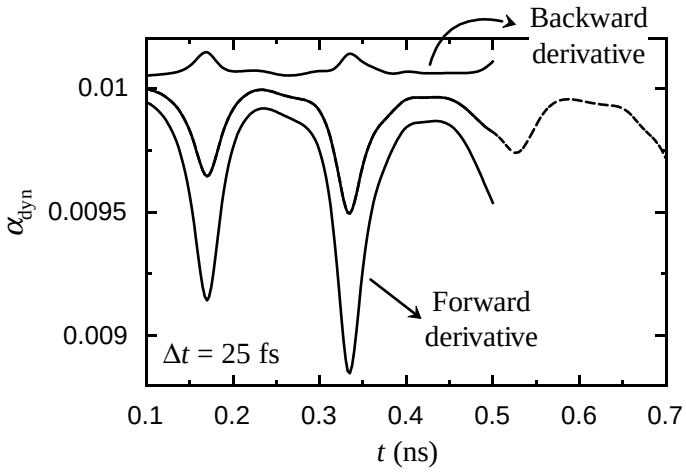

Figure A.6: First-order backward and forward $\alpha_{\rm dyn}$ values together with their average (dashed curve) and the second-order formula value (solid curve on top of the dashed one).

analogue $\alpha_{\rm MS}$ (Fig. A.5**e**) (these quantities were define in Sect. 3.2). Associated with the average in-plane oscillation of magnetisation we find corresponding oscillations in the value of $\alpha_{\rm dyn}$. These deviations from the imposed α value are strictly associated with the evaluation of time derivatives, maximum deviations occurring when the magnetisation movement (as a whole) slows down and reverses direction. Allowing for a maximum deviation of 5% constraints the allowed time step values to a few tens of femtoseconds. A value of $\Delta t = 25$ fs was used in all simulations presented in the main body of the text.

The recalculated damping parameter α_{dyn} provides for an extremely sensitive tool for quantitatively measuring time domain errors during magnetisation motion. Accordingly, great care must be taken when evaluating Eq. (A.39), since it combines quantities defined at specific time instants ($\mathbf{h}_{\rm eff}$) with time derivatives of the magnetisation. In the associated discretised expressions, to first-order in time, the quantity $\partial\mathbf{m}/\partial\tau$ can be approximated through the use of either a backward or a forward differencing formula. For the transverse oscillations experiment of Fig. A.5, the values arising from these two implementations are shown in Fig. A.6, for the first oscillation period of $\langle m_x \rangle$. The curves shown are markedly different from each other and from that given in Fig. A.5**d**. Higher-order formulae are evidently required in evaluating the time derivatives in Eq. (A.39). Both the average of the first-order forward and backward values and a true second-order expression for $\partial\mathbf{m}/\partial\tau$ produce the same data, as shown in Fig. A.6. For simplicity in bookkeeping operations, the average of first-order values was used in producing the data given in the main text.

Although a quantitative time domain error measure is now available through the recalculated damping parameter, spatial discretisation procedures must not be neglected. It is the authors' opinion, based on the experience gained over the past years, that in situations where micromagnetic structures are nucleated, the errors introduced due to insufficient spatial meshes greatly surpass those arising from carefully chosen time integration schemes. These, essentially, spatial domain errors can have a significant influence on the time domain magnetisation motion and the monitoring of α_{dyn} is of much help in pinpointing such potentially problematic time windows. A striking example of this statement can be found by looking at the results of the μMAG's Standard Problem No. 4 [51, 78] (see App. B).

It is noteworthy to point out that this quantitative error measure is independent of the numerical integration scheme used and could be effectively used as an adaptive time step control parameter through the specification of the maximum allowed error on α_{dyn}.

Additionally, this time domain error measure allows for the quantification of the accuracy impact of the different implicit contributions to the numerical integration scheme. As stated above, a simple analogy with the stability analysis of diffusion equations, leads us to the sole inclusion of exchange contributions in the implicit terms of the proposed Crank-Nicolson scheme. Equipped with the control tool of damping parameter recalculation, a detailed analysis of the stability features of different effective field terms may now be undertaken. Focusing on the first oscillation period in Fig. A.5, corresponding to the first drop in the value of α_{dyn}, a comparison is made in Fig. A.7**a** between different contributions to the implicit terms in the discretised LLG equation: the sole inclusion of exchange contributions, exchange contributions plus the out-of-plane demagnetising field component, and finally exchange plus all demagnetising contributions, still restricted to first-neighbours interactions. The data shown, clearly reveals that the sole inclusion of exchange contributions leads to the most effective stabilisation procedure. In order to achieve the same error level in the α_{dyn} parameter, when considering all demagnetising contributions, time step values must be reduced by more than an order of magnitude, thereby increasing by the same amount the total computational time. In addition, error sign changes dramatically with the inclusion of implicit demagnetising terms, going from negative from positive values. Focusing on the same time window, the opportunity is seized to clearly demonstrate that the time dependence of recalculated damping parame-

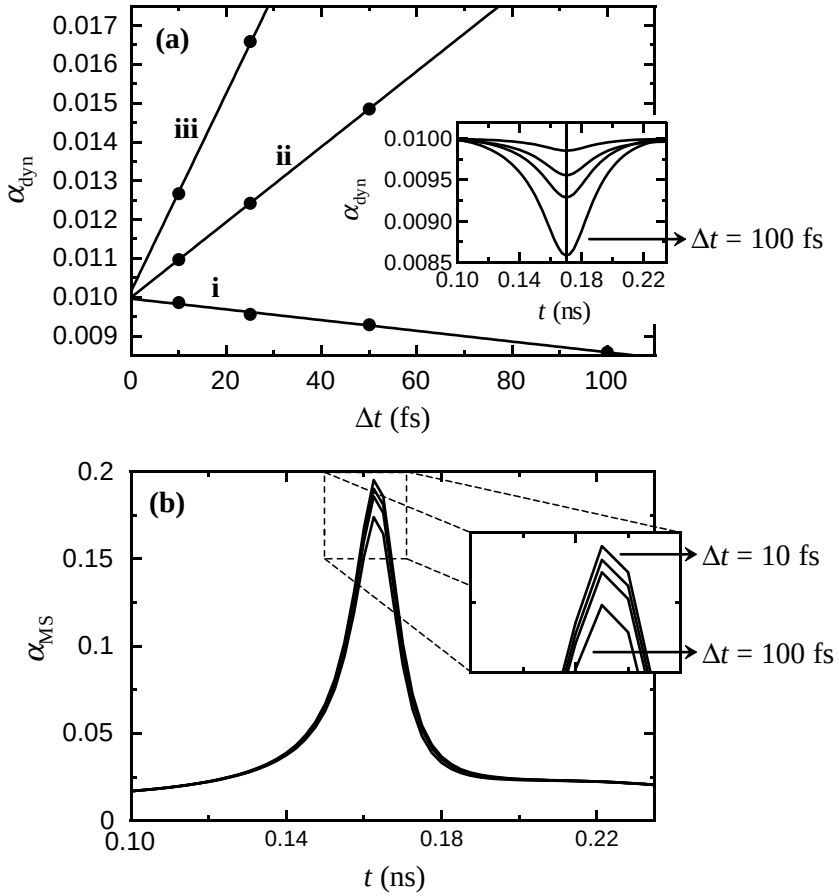

Figure A.7: **(a)** α_{dyn} values as a function of time step for different contributions to the implicit terms in the numerical integration scheme: **i** Exchange contributions only, **ii** exchange plus the out-of-plane demagnetising component, and **iii** exchange plus all demagnetising contributions. **(b)** α_{MS} curves as a function of time for the first peak in α_{dyn} using exchange contributions only. The different curves corresponding to different time step values clearly demonstrate that the time variations of the macrospin equivalent of α_{dyn} are not the result of numerical artifacts.

ter α_{MS}, which can be interpreted as a measure of the degree of macrospin like behaviour in non-uniform magnetisation distributions, is *not* the result of poor numerical procedures (Fig. A.7**b**).

A straightforward comparison with a fully explicit scheme allows to further explore the meaning of this error measure. α_{dyn} values for three simulations done using an explicit integration scheme are compared with the previous curve (Fig. A.8). Two comments should be made when looking at the data. First, as long as explicit simulations do not breakdown, the magnitude of error in α_{dyn} remains comparable to those obtained using the *optimised*

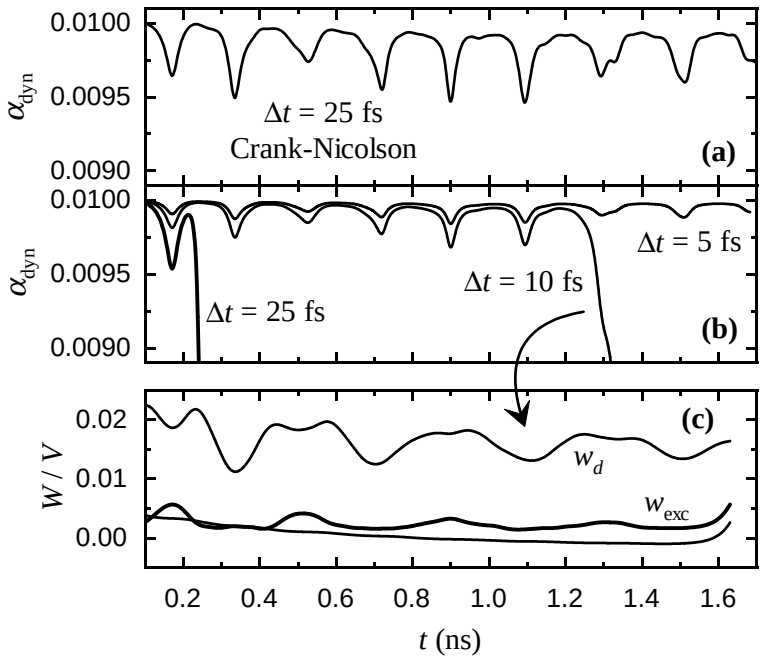

Figure A.8: Comparison between $\alpha_{\rm dyn}$ values for the Crank-Nicolson integration scheme **(a)** and those using the simpler explicit scheme **(b)**. **(c)** Different energy values corresponding to an explicit calculation using a time step of 10 fs.

semi-implicit Crank-Nicolson scheme. Second, a comparison between the time evolution of $\alpha_{\rm dyn}$ and of the different energy components clearly highlights the usefulness of the former as a numerical control parameter. Catastrophic numerical breakdown is usually associated with a divergent increase in the system's total energy. Indeed, magnetisation distributions arising from a unstable calculation present the characteristic feature of large amplitude anti-correlated fluctuations between adjacent grid locations, which lead to an immediate rise of the exchange energy. According to Eq. (A.38), however, under time-independent external energy contributions, energy may only increase if and only if the parameter α becomes negative. Continuous monitoring of $\alpha_{\rm dyn}$ allows for the detection of the onset of instabilities, in this particular case, more than 0.2 ns in advance of the increase in the system's total energy value.

A.3 Torque Monitoring (Topology)

As stated in Sect. A.1.1, the maximum value of the reduced torque's norm provides for the most reliable (and physically justifiable) convergence parameter in static micromagnetic

simulations. Such parameter allows to obtain, when studying magnetisation dynamics, an additional information regarding the particular interplay between the spatial and time components of dynamical simulations. Consider, for instance, the easy axis switching experiment described in Sect. 4.1. For the applied field parameters used, switching occurred through a mechanism where vortex nucleation might well have taken place. Here, we shall repeat this experiment, now slightly changing the pulse time profile (see Fig. A.9). If the average magnetisation dynamics is basically not altered, vortices are now clearly nucleated (see Fig. A.9**b**). Besides, the maximum (and minimum) out-of-plane magnetisation components vary sharply at specific time instants (Fig. A.9**b**), corresponding to pronounced peaks in the maximum value of torque in the system (Fig. A.9**c**). Innocuous as these variations may seem, if referring to their influence on average magnetisation curves, this calculation violates one of the basic postulates of micromagnetic theory, namely *continuity*.

The indicated peak in the maximum value of the reduced torque represents a small time window within which the out-of-plane direction of the vortices change, as depicted in the inserted diagram, corresponding to the sudden appearance of a negative out-of-plane magnetisation value. Magnetisation distribution snapshots taken during this time interval (Fig. A.10) clearly demonstrate the magnetisation processes responsible for this sharp variations. Due to a strong "gyrotropic" motion, vortex cores may get compressed to lateral scales smaller than the smallest mesh dimension. When this occurs, the vortex may literally *fall* inside the mesh and flip its centre region. Such transitions within the magnetic body violate micromagnetic topological principles and correspond to a purely numerical artifact [80, 81]. In reality, a three-dimensional spins configuration in a two-dimensional space displays no topological barrier [80]. Otherwise stated, from a strictly mathematical viewpoint, every spin distribution may be transformed into any other. The transition from an *up* to a *down* vortex can be therefore achieved through two distinct processes, as evidenced in Fig. A.11. Either through the opening of the vortex core region (left path) or through the rotation of the vortex as a whole towards its final magnetisation configuration (right path).

Nevertheless, without breaking the continuity imposed by micromagnetic theory, the sole possible transition allowing a change in the vortex rotational vector requires the rotation as a whole of the magnetisation distribution, in opposition to the severe energy constraints of the system. In this sense, vortex core flipping can be termed as a quasi-topological impossibility [81]. Another possibility is to displace the vortex towards the

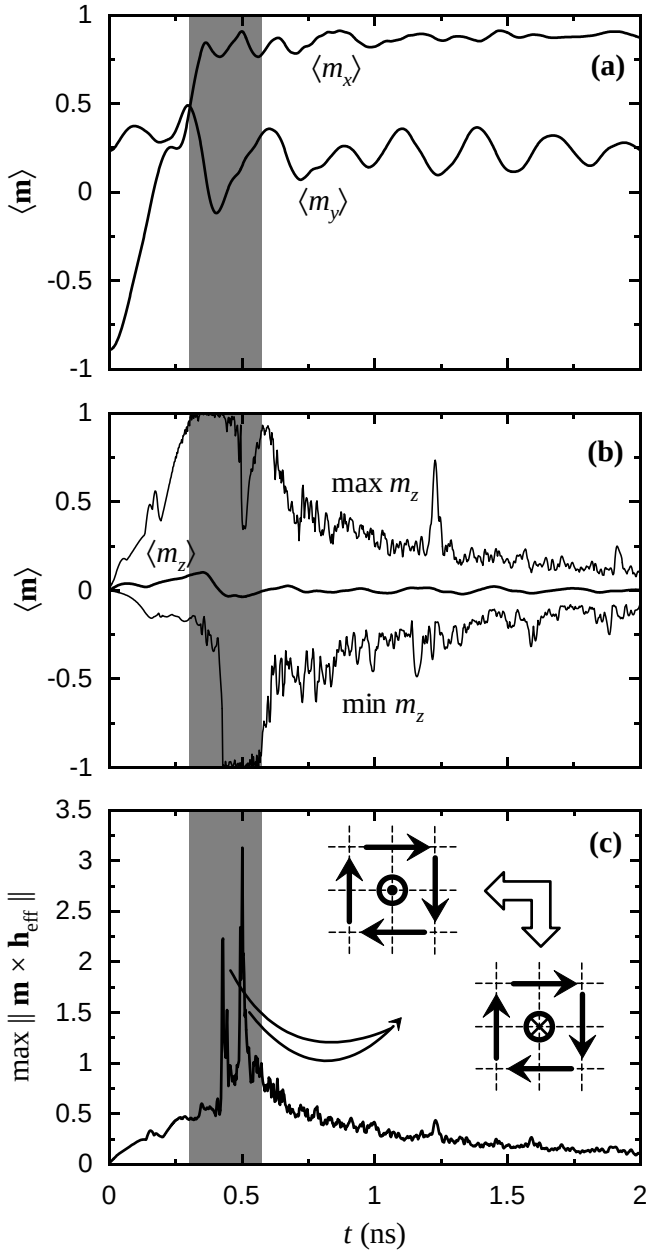

Figure A.9: Easy axis driven magnetisation switching. **(a)** In-plane average magnetisation components. **(b)** Maximum, average, and minimum out-of-plane magnetisation values. **(c)** Reduced torque versus time. The signalled sharp peaks correspond to the short time windows where vortex core flipping occurs (inserted diagram). Shaded areas indicate the period of time where vortices exist.

edge of the magnetic body and out of the sample and reintroduce it with a reversed core direction. This however may be forbidden due to "gyrotropic" effects.

We should stress the fact that when performing dynamical micromagnetic simulations

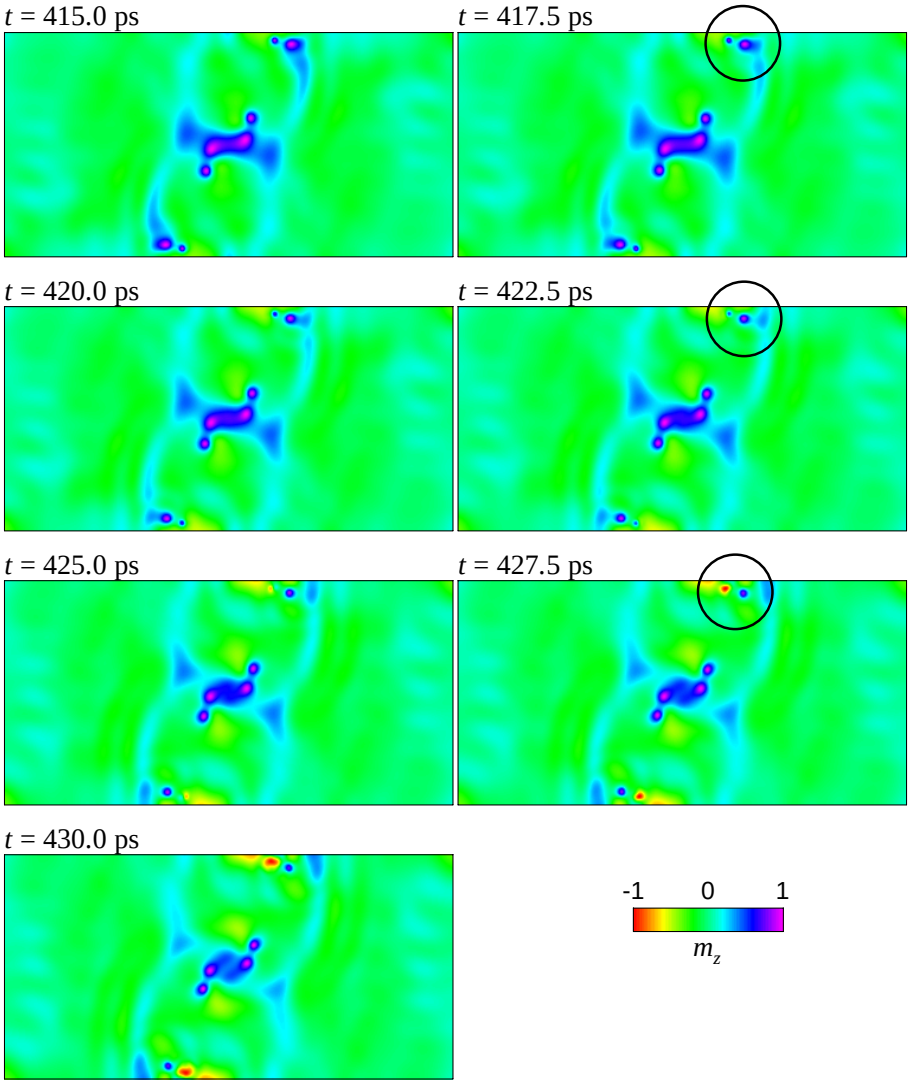

Figure A.10: (Colour) Out-of-plane magnetisation distribution snapshots corresponding to the first sharp peak in Fig A.9**c**. The encircled regions pinpoint the vortex core flipping arising from an insufficient spatial discretisation associated with strong "gyrotropic" effects.

the "gyrotropic" effects, such as those evidenced above, even if not leading to catastrophic situations, may considerably stiffen the motion of strongly localised micromagnetic structures such as vortices. In this manner, purely numerical, spurious magnetisation movements may be present in the system, resulting in unpredictable, but assuredly, non-physical characteristics, raising the error level in α_{dyn} accordingly, as demonstrated in App. B in another context.

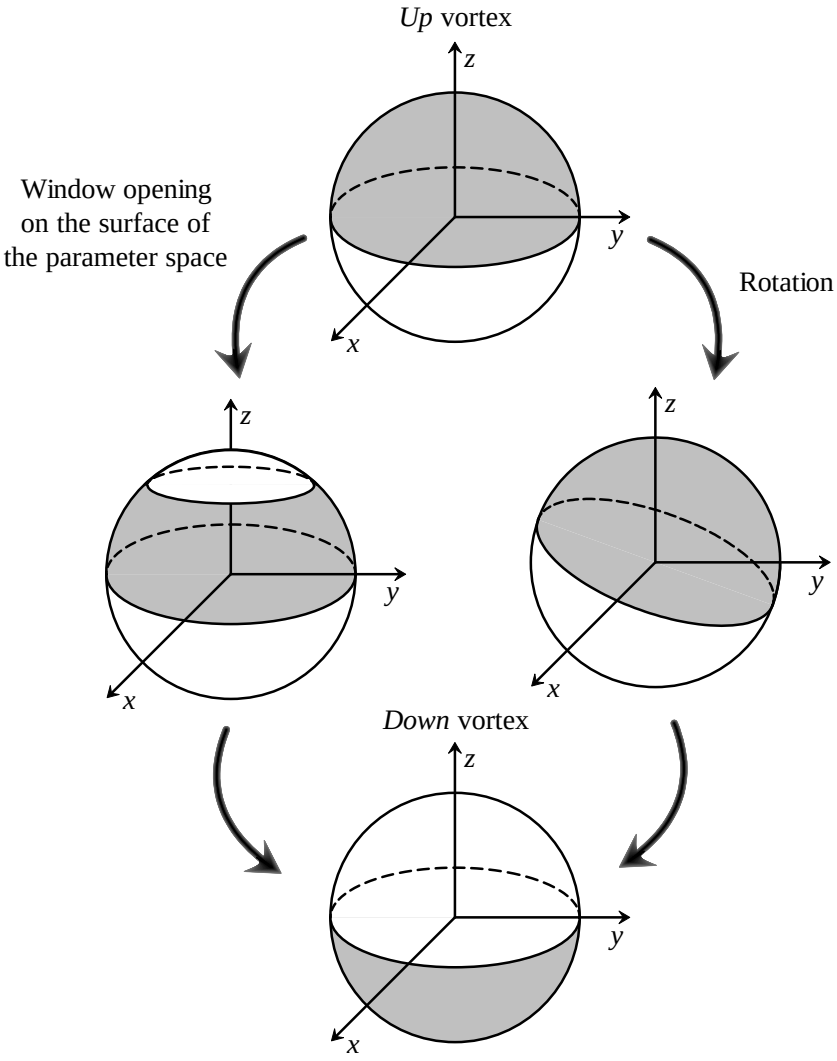

Figure A.11: Schematic representation of the possible mechanism of vortex core flipping through an unit sphere projection of **m**. Left: Vortex core opening towards the equatorial plane. Right: Rotation as a whole.

A.4 Structural Disorder

By their very nature, finite-difference methods are commonly regarded an being incapable of handling structural disorder in contrast with finite elements methods. Up to some extent, however, realistic structural disorder can be modelled within the framework of a full finite difference micromagnetic code, and this without hindering in any way whatsoever the efficiency resulting from the use of FFT acceleration techniques.

Generally speaking, one must be able to independently address the magnetic properties of individual grains in a textured magnetic layer. This has been simply achieved by the

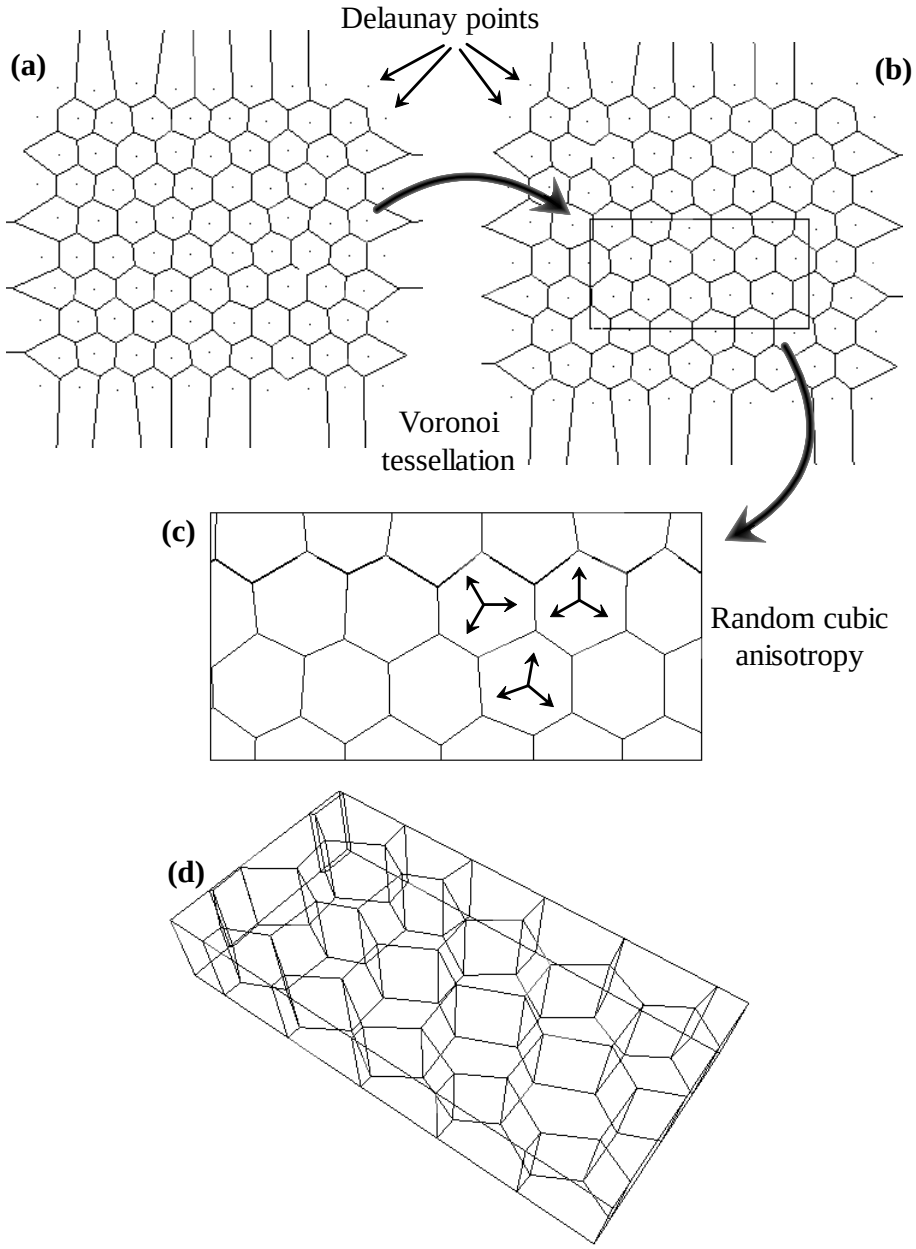

Figure A.12: Two- and three-dimensional grain generation methodology. **(a)** Unbounded Voronoi diagram associated with a given distribution of Delaunay points in a plane. **(b)** Superposition of the boundaries of the simulated magnetic platelet. **(c)** Trimming of the Voronoi diagram to the boundaries of the platelet. **(d)** Straightforward thickness projection maintaining the same grain cross-section.

superposition of a Voronoi diagram, representing an ensemble of ferromagnetic grains, on top of the magnetisation grid used. Each grid point may then be uniquely associated with a single grain, inheriting, therefore, its magnetic properties. Here, we have only

considered magnetic anisotropy. Exchange variations, besides being poorly documented in the literature, raise the additional question of inter-grain interactions.

Since the Voronoi diagram preferably represents a physical grain structure, its generation was strictly controlled. By definition, a Voronoi diagram (also sometimes called a Dirichlet tessellation) is the partitioning of a plane with n points into n convex polygons, such that each polygon contains exactly one point and every point in a given polygon is closer to its central point than to any other (Fig. A.12). A regular distribution of points, i.e. all points are belonging to the vertices of a perfectly regular two-dimensional triangular mesh (all triangles being equal and equilateral), results in a Voronoi diagram composed of perfect hexagons. Introducing slight misarrangements of these Delaunay points effectively controls the degree of irregularity of the resulting tessellation, therefore producing a more realistic honeycomb pattern. To an ensemble of grains so defined was associated a distribution of cubic anisotropy axes. Three random independent angles are sufficient to define the director cosines. All the steps above have been performed using the freely available GEOMPACK computational geometry package [82].

Standard computational geometry procedures allow for the handling of such two-dimensional polygon diagrams and their immediate transformation into a real three-dimensional grain distribution (Fig. A.12**d**). This step essentially requires a reordering of the (now) three-dimensional points in order to define planes corresponding to grain boundaries [83, 84]. As before, the GEOMPACK package can be used for the three-dimensional subdivision of grains if needed.

Appendix B

μMAG Standard Problem No. 4

In the first quarter of year 2000, the μMAG team at the National Institute of Standards and Technology (NIST) [38] released the 4th micromagnetic standard problem [51]. Its aim was to extend the scope of the previously released proposals by focusing on the dynamical aspects of micromagnetic calculations. As usual, and explicitly stated in the specifications, submitted reports should be shown to be independent of the spatial discretisation values used. In addition, since this is a fully dynamical problem, time step invariability should also be demonstrated. Here we shall make full use of the recalculated damping parameter as an innovative way of controlling the simulation results and to validate the set of numerical parameters employed.

Two separate problems were actually proposed. Both regarded the dynamical response of a thin film platelet with dimensions $500 \times 125 \times 3$ nm^3. The material parameters used are $A = 1.3 \times 10^{-11}$ J/m (1.3×10^{-6} erg/cm), $M_s = 8 \times 10^5$ A/m (800 emu/cc), $K_u = 0$, and $\alpha = 0.02$ [51][(a)]. The response of this element, in an initial S state pointing in the $+x$ direction, is to be determined when subjected to the action of two uniform field steps. The magnitude and orientation of the first field does not induce magnetisation switching and the system as a whole simply oscillates around its new equilibrium position before coming to a complete halt. This behaviour adds nothing to the transverse oscillations experiments considered in Chap. 3 and App. A, and shall not be further discussed here. The second field configuration, however, induces a quite different dynamical behaviour, strongly resembling the easy axis switching experiments of Sect. 4.1. The average y magnetisation curves for

[(a)] Graphical representations will also make use of the SI system of units in order to facilitate possible comparisons with the μMAG submission pages.

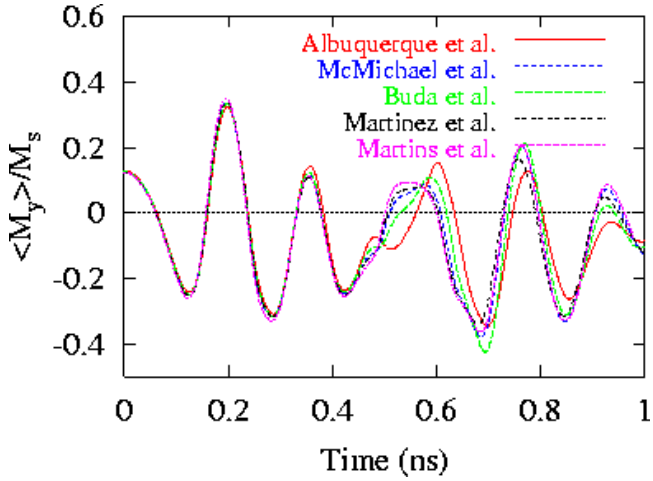

Figure B.1: (Colour) *Reprinted from μMAG's web site (June 2002).* Transverse average magnetisation curves for the second field configuration and for the different submitted reports as a function of time.

all the submitted reports to this second set of field parameters are displayed in Fig. B.1 for the smallest mesh size exploited by the respective authors. Differences between the given average curves can be clearly discerned. The following two sections aim at a brief discussion of these results.

B.1 Static Energy Convergence

The remanent S state magnetisation distribution for the three different demagnetising field calculations proposed by the OOMMF package are directly compared with our own code (here represented by the acronym IDMMC, standing for Implicit Dynamical MicroMagnetic Code) in Fig. B.2. As seen above, different ways of evaluating the demagnetising interactions can provide quite different results. If the differences in the rate of energy convergence can be deemed minor, all should converge to the same energy value as the spatial discretisation tends towards zero. Such is evidently not the case for the "ConstMag" scheme if compared with the two other schemes available in the OOMMF package and our own method. For this "ConstMag" scheme, averaging procedures do seem to produce inaccurate results in contrast with the conclusions drawn out from the Standard Problem No. 2 where the magnetisation distribution was taken in a fully aligned direction [85]. Despite the strong differences displayed in Fig. B.2, further comparisons between OOMMF data and our own simulations will, for the sake of consistency (and to allow a direct com-

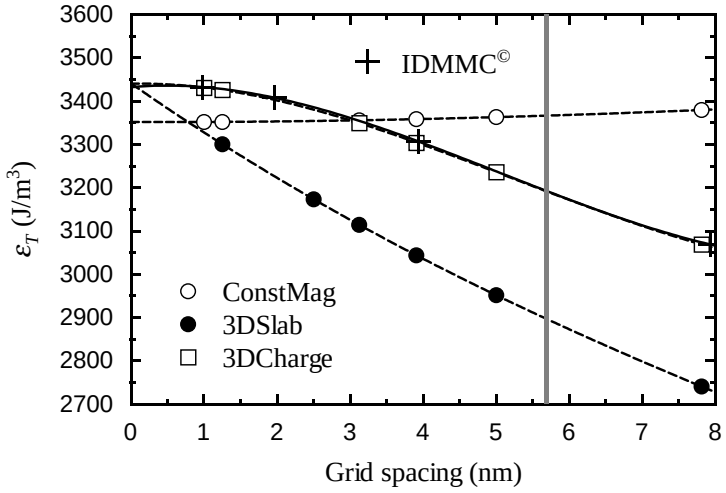

Figure B.2: Static energy convergence for an S state using the parameters of the Standard Problem No. 4. The different demagnetising evaluation schemes available in the OOMMF 2D package are here compared with our own code (IDMMC).

parison with the data given in [51]), suppose the use of the "ConstMag" demagnetising field evaluation procedure.

B.2 Dynamic Analysis

We shall start with the discussion of our own set of results [78]. Figure B.3**a** presents the in-plane average magnetisation components as a function of time for two mesh spacing values: 2 and 4 nm (thick and thin lines, respectively). Although both values are well below the exchange length for the material parameters considered, visible differences appear after approximately 0.5 ns. As seen in Fig. B.3**b**, these differences appear as soon as vortices are nucleated in the interior of the element. Additionally, this time window corresponds to an increase in the value of the recalculated damping parameter (Fig. B.3**d**).

A detailed view of the magnetisation processes occurring is next considered for the smallest mesh spacing used (2 nm) and for different values of the integration time step (Fig. B.4). Following the field pulse application, an anticlockwise rotation of the inner core region of the platelet produces two 360° walls (0.10 to 0.20 ns snapshots) that violently unwind at the cost of generating localised magnetisation structures such as vortices (0.50 ns snapshot). The time window corresponding to the creation, displacement, and eventual expulsion of these micromagnetic structures also corresponds to the interval where differences between the proposed solutions creep in. Although the average magnetisation curves

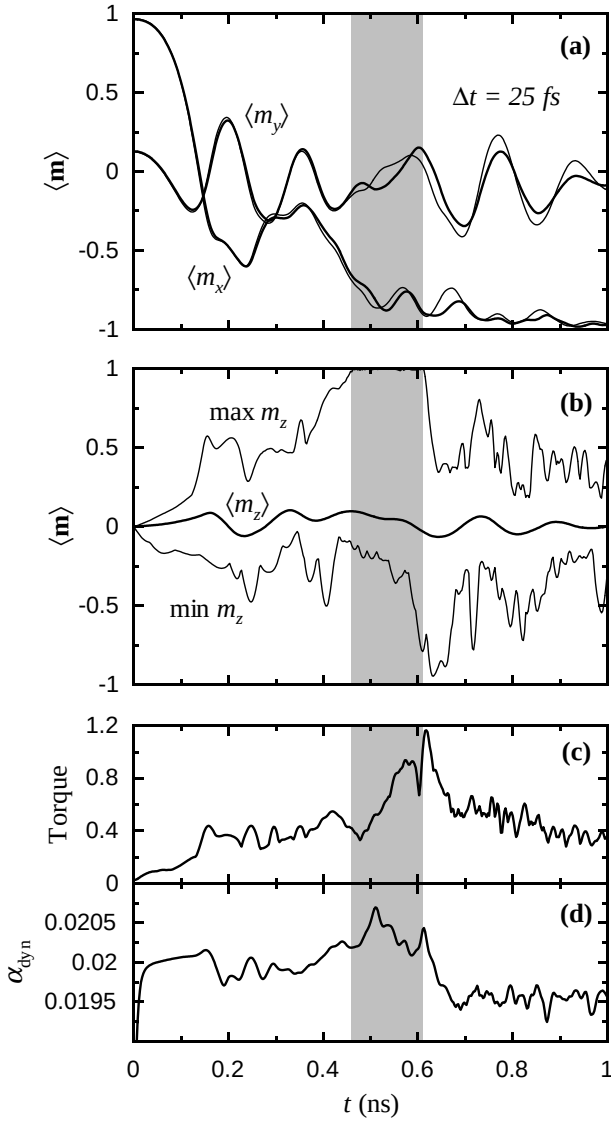

Figure B.3: **(a)** Average in-plane magnetisation curves for two mesh spacing values: 2 and 4 nm (thick and thin lines, respectively). **(b)** Average, maximum, and minimum out-of-plane magnetisation curves (2 nm). **(c)** Maximum torque's norm and **(d)** recalculated damping parameter, respectively (2 nm). The shaded areas indicate the presence of vortices.

in Fig. B.4**a** are indiscernible, the recalculated damping parameter is highly sensitive to variations in the time step values used. It should be noted that the largest errors in α_{dyn} occur at approximately 0.5 nanoseconds.

Comparing the average magnetisation curves in Figs. B.3 and B.4 indicates that spatial discretisation values play a preponderant role in determining the magnetisation behaviour of the Standard Problem No. 4. A detailed comparison was made between our results achieved with a mesh spacing of 2 nm and those obtained through the use of the publicly

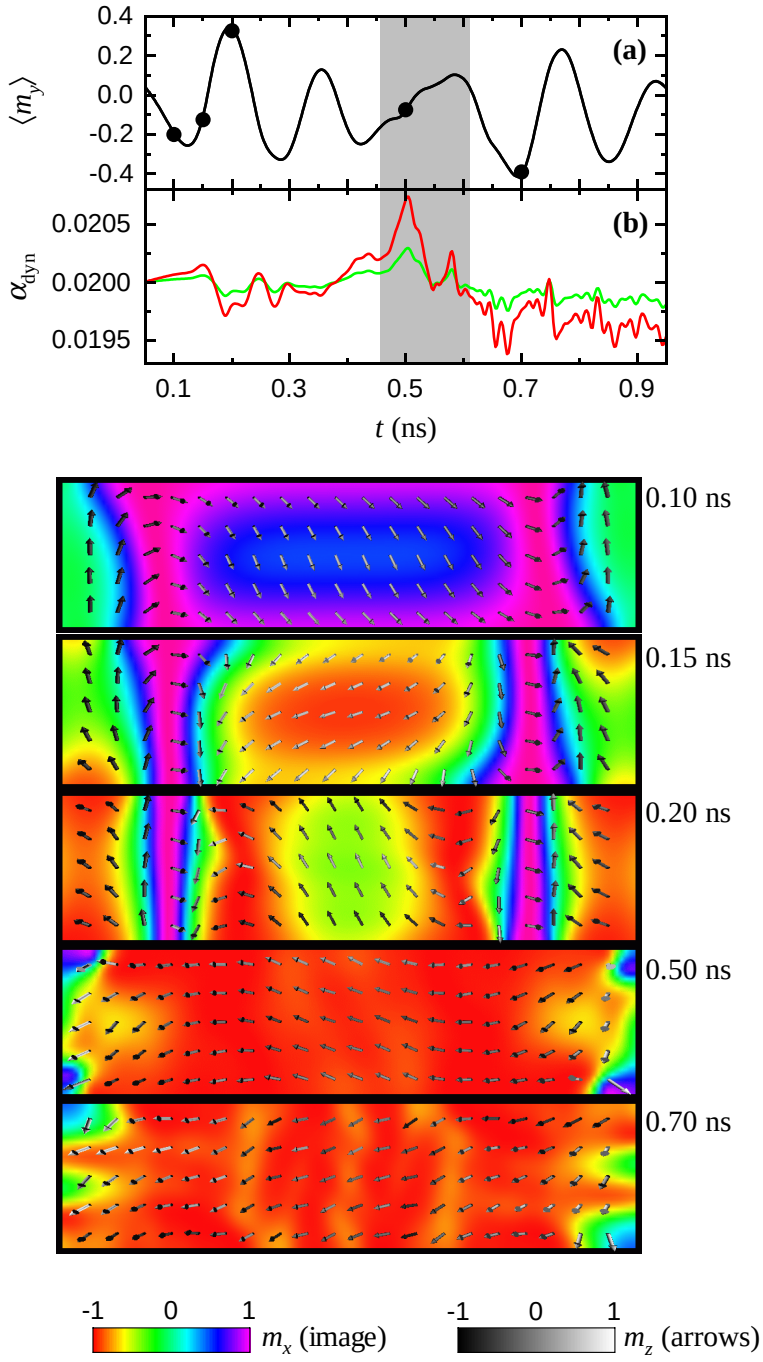

Figure B.4: (Colour) **(a)** Average transverse magnetisation curves for a mesh spacing value of 2 nm and for two integration time steps: 25 and 10 fs. The points shown correspond to the times on the different magnetisation snapshots displayed below. **(b)** Corresponding recalculated α values (red: 25 fs; green: 10 fs).

available OOMMF package. In order to perform a relevant comparison with the submission results from the NIST team (McMichael et al.), OOMMF simulations were made using

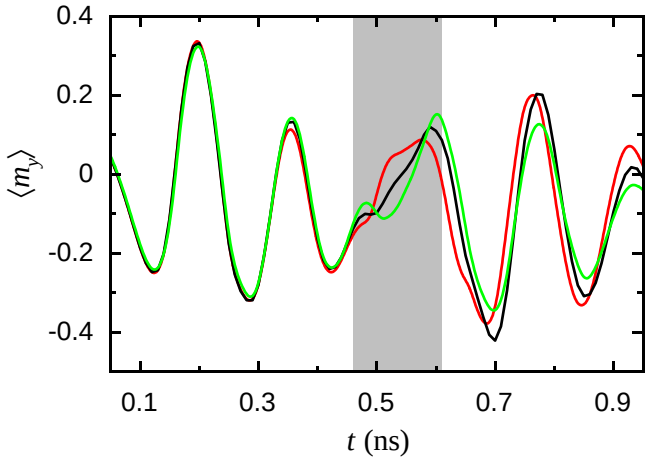

Figure B.5: (Colour) Comparison between the average magnetisation curves for two mesh spacing values in the OOMMF simulations (red: 3.125 nm; black: 1.25 nm). Our data is shown in green for a mesh spacing value of 2 nm.

the same demagnetising field evaluation procedures ("ConstMag"). Results are shown in Fig. B.5: Our submission (green), that originally posted by the NIST team (red: 3.125 nm spacing), and a simulation using the same parameters with the exception of the mesh spacing, now decreased to 1.25 nm (black). Clearly, as the mesh spacing value is decreased, OOMMF results approach our own [86]. In particular, the fine details missing in all other contributions (as seen in Fig. B.1), start to appear. These exactly coincide with the time window were vortices are present in the platelet. A more correct spatial description of such structures has, as one can see, dramatic consequences regarding the average dynamical magnetisation curves, highlighting the strong interdependence between spatial and time domain micromagnetic simulation parameters. In conclusion, strong "gyrotropic" effects do require a significant decrease of the allowed mesh spacing values in order for mesh independency to be attained and in this regard the efficiency of numerical procedures can play a significant role in achieving the smallest possible computational time.

Bibliography

[1] C. Cohen-Tannoudji, B. Diu, and F. Laloë, *Quantum Mechanics* (John Wiley & Sons, New York, 1977).

[2] L. D. Landau and E. Lifshitz, "On the theory of the dispersion of magnetic permeability in ferromagnetic bodies," Phys. Z. Sowjetunion **8,** 153–169 (1935).

[3] T. L. Gilbert, "A Lagrangian formulation of the gyromagnetic equation of the magnetization field," Phys. Rev. **100,** 1243 (1955), abstract only.

[4] J. Miltat, G. Albuquerque, and A. Thiaville, "An Introduction to Micromagnetics in the Dynamical Regime," in *Spin Dynamics in Confined Magnetic Structures*, B. Hillebrands and K. Ounadjela, eds., (Springer, Heidelberg, 2001).

[5] R. Kikuchi, "On the minimum of magnetization reversal time," J. Appl. Phys. **27,** 1352–1357 (1956).

[6] A. P. Malozemoff and J. C. Slonczewski, *Magnetic Domain Walls in Bubble Materials* (Academic Press, New York, 1979).

[7] H. C. Siegmann, E. L. Garwin, C. Y. Prescott, J. Heidmann, D. Mauri, D. Weller, R. Allenspach, and W. Weber, "Magnetism with picosecond field pulses," J. Magn. Magn. Mat. **151,** L8–L12 (1985).

[8] C. H. Back, D. Weller, J. Heidmann, D. Mauri, D. Guarisco, E. L. Garwin, and H. C. Siegmann, "Magnetization reversal in ultrashort magnetic field pulses," Phys. Rev. Lett. **81,** 3251–3254 (1998).

[9] C. H. Back, R. Allenspach, W. Weber, S. S. P. Parkin, D. Weller, E. L. Garwin, and H. C. Siegmann, "Minimum field strength in precessional magnetization reversal," Science **285,** 864–867 (1999).

[10] W. Brown, Jr., *Micromagnetics* (Robert E. Krieger, Huntington, 1978).

[11] G. A. Prinz, "Magnetoelectronics," Science **282,** 1660–1663 (1998).

[12] H. Ohno, "Toward functional spintronics," Science **291,** 840–841 (2001).

[13] S. A. Wolf, D. D. Awschalom, R. A. Buhrman, J. M. Daughton, S. von Molnár, M. L. Roukes, A. Y. Chtchelkanova, and D. M. Treger, "Spintronics: A spin-based electronics vision for the future," Science **294,** 1488–1495 (2001).

[14] R. H. Koch, J. G. Deak, D. W. Abraham, P. L. Trouilloud, R. A. Altman, Y. Lu, W. J. Gallagher, R. E. Scheuerlein, K. P. Roche, and S. S. P. Parkin, "Magnetization reversal in micron-sized magnetic thin films," Phys. Rev. Lett. **81,** 4512–4515 (1998).

[15] T. J. Silva, C. S. Lee, T. M. Crawford, and C. T. Rogers, "Inductive measurement of ultrafast magnetization dynamics in thin-film Permalloy," J. Appl. Phys. **85,** 7849–7862 (1999).

[16] M. R. Freeman and B. C. Choi, "Advances in Magnetic Microscopy," Science **294,** 1484–1488 (2001).

[17] S. Kaka and S. E. Russek, "Precessional switching of submicrometer spin valves," Appl. Phys. Lett. **80,** 2958–2960 (2002).

[18] H. W. Schumacher, C. Chappert, P. Crozat, R. C. Sousa, P. P. Freitas, J. Miltat, and J. Ferré, "Precessional magnetization reversal in microscopic spin valve cells," IEEE Trans. Magn. (2002), to be published.

[19] C. T. Chen, Y. U. Idzerda, H. J. Lin, N. V. Smith, G. Meigs, E. Chaban, G. H. Ho, E. Pellegrin, and F. Sette, "Experimental confirmation of the X-ray magnetic circular dichroism sum rules for iron and cobalt," Phys. Rev. Lett. **75,** 152–155 (1995).

[20] H. Goldstein, *Classical Mechanics* (Addison-Wesley, Reading, 1980).

[21] C. Lanczos, *The Variational Principles of Mechanics* (University of Toronto Press, Toronto, 1970).

[22] A. Aharoni, *Introduction to the Theory of Ferromagnetism* (Clarendon Press, Oxford, 1996).

[23] W. Döring, "Über die Trägheit der Wände zwischen Weißschen Bezirken (On the inertia of walls between Weiss domains)," Z. Naturforsch. **3a,** 373–379 (1948).

[24] A. Hubert and R. Schäfer, *Magnetic Domains* (Springer-Verlag, Berlin, 1998).

[25] M. Labrune, J. C. S. Kools, and A. Thiaville, "Magnetization rotation in spin-valve multilayers," J. Magn. Magn. Mat. **171,** 1–15 (1997).

[26] E. Bonet, W. Wernsdorfer, B. Barbara, A. Benoit, D. Mailly, and A. Thiaville, "Three-dimensional magnetization reversal measurements in nanoparticles," Phys. Rev. Lett. **83,** 4188–4191 (1999).

[27] E. C. Stoner and E. P. Wohlfarth, "A mechanism of magnetic hysteresis in heterogeneous alloys," Phil. Trans. Roy. Soc. **A240,** 599–642 (1948).

[28] J. C. Slonczewski, "Theory of magnetic hysteresis in films and its application to computers," Research Memorandum RM 003.111.224, IBM (1956) .

[29] A. Anguelouch, B. D. Schrag, G. Xiao, Y. Lu, P. L. Trouilloud, R. A. Wanner, W. J. Gallagher, and S. S. P. Parkin, "Two-dimensional magnetic switching of micron-size films in magnetic tunnel junctions," Appl. Phys. Lett. **76,** 622–624 (2000).

[30] A. Thiaville, "Extensions of the geometric solution of the two dimensional coherent magnetization rotation model," J. Magn. Magn. Mat. **182,** 5–18 (1998).

[31] A. Thiaville, "Coherent rotation of magnetization in three dimensions: A geometrical approach," Phys. Rev. B **61,** 12221–12232 (2000).

[32] J. Miltat, G. Albuquerque, and A. Thiaville, "Micromagnetics: Dynamical Aspects," in *Magnetism and Synchroton Radiation*, E. Beaurepaire, F. Scheurer, G. Krill, and J. P. Kappler, eds., (Springer, Berlin, 2001).

[33] L. He, W. D. Doyle, and H. Fujiwara, "High speed coherent switching below the Stoner-Wohlfarth limit," IEEE Trans. Magn. **30,** 4086–4088 (1994).

[34] C.-R. Chang and J.-S. Yang, "Oscillatory switching under a rapidly varying magnetic field," Phys. Rev. B **54,** 11957–11960 (1996).

[35] M. Bauer, J. Fassbender, B. Hillebrands, and R. L. Stamps, "Switching behavior of a Stoner particle beyond the relaxation time limit," Phys. Rev. B **61,** 3410–3416 (2000).

[36] M. Bauer, R. Lopusnik, J. Fassbender, and B. Hillebrands, "Suppression of magnetic-field pulse-induced magnetization precession by pulse tailoring," Appl. Phys. Lett. **76,** 2758–2760 (2000).

[37] A. Thiaville and J. Miltat, "Small is beautiful," Science **284,** 1939–1940 (1999).

[38] http://www.ctcms.nist.gov/ rdm/toc.html.

[39] W. Rave and A. Hubert, "Magnetic ground state of a thin-film element," IEEE Trans. Magn. **36,** 3886–3899 (2001).

[40] G. M. Sandler, H. N. Bertram, T. J. Silva, and T. M. Crawford, "Determination of the magnetic damping constant in NiFe films," J. Appl. Phys. **85,** 5080–5082 (1999).

[41] T. Gerrits, J. Hohlfeld, O. Gielkens, K. J. Veenstra, K. Bal, T. Rasing, and H. A. M. van den Berg, "Magnetization dynamics in NiFe thin films induced by short in-plane magnetic field pulses," J. Appl. Phys. **89,** 7648–7650 (2001).

[42] T. M. Crawford, T. J. Silva, C. W. Teplin, and C. T. Rogers, "Subnanosecond magnetization dynamics measured by the second-harmonic magneto-optic Kerr effect," Appl. Phys. Lett. **74,** 3386–3388 (1999).

[43] W. J. Gallagher, J. H. Kaufman, S. S. P. Parkin, and R. E. Scheuerlein, "Magnetic memory array using magnetic tunnel junction devices in the memory cells,", 1997, United States Patent No. 5640343.

[44] J. N. Chapman, P. R. Aitchinson, K. J. Kirk, S. McVitie, J. C. S. Kools, and M. F. Gilies, "Direct observation of magnetization reversal processes in micron-sized elements of spin-valve material," J. Appl. Phys. **83,** 5321–5325 (1998).

[45] J. Miltat, G. Albuquerque, and D. Tomáš, "Magnetization state switching in submicron size soft elements: A numerical study in the nanosecond regime,", MRS 1999 Spring Meeting Abstracts Book, 1999, Communication J7.1.

[46] J. Miltat, G. Albuquerque, and A. Thiaville, "Quasi-coherent rotation switching mode in meso-scale patterned sructures," In *Frontiers in Magnetism Proceedings*, K. V. Rao, A. M. Grishin, and T. H. Johansen, eds., (The Royal Institute of Sweden, Stockholm, Sweden, 1999), ISBN 91-7170-438-8.

[47] R. Sousa and P. P. Freitas, "Dynamic switching of tunnel junction MRAM cell with nanosecond field pulses," IEEE Trans. Magn. **36,** 2770–2772 (2000).

[48] J. Shi and S. Tehrani, "Edge-pinned states in patterned submicron NiFeCo structures," J. Appl. Phys. **77,** 1692–1694 (2000).

[49] Y. Acremann, C. H. Back, M. Buess, O. Portmann, A. Vaterlaus, D. Pescia, and H. Melchior, "Imaging precessional motion of the magnetisation vector," Science **290,** 492–495 (2000).

[50] http://math.nist.gov/oommf.

[51] http://www.ctcms.nist.gov/ rdm/std4/spec4.html.

[52] J. Miltat and A. Thiaville (unpublished).

[53] D. E. Heim and S. S. P. Parkin, "Magnetoresistive spin valve sensor with improved pinned ferromagnetic layer and magnetic recording system using the sensor,", 1995, United States Patent No. 5465185.

[54] S. S. P. Parkin, N. More, and K. P. Roche, "Oscillations in exchange coupling and magnetoresistance in metallic superlattice structures: Co/Ru, Co/Cr, and Fe/Cr," Phys. Rev. Lett. **64,** 2304–2307 (1990).

[55] S. S. P. Parkin and D. Mauri, "Spin engineering: Direct determination of the Ruderman-Kittel-Kasuya-Yosida far-field range function in ruthenium," Phys. Rev. B **44,** 7131–7134 (1991).

[56] A. Thiaville, D. Tomáš, and J. Miltat, "On corner singularities in micromagnetics," Phys. Status Solidi A **170,** 125–135 (1998).

[57] W. Bailey, P. Kabos, F. Mancoff, and S. Russek, "Control of magnetization dynamics in $Ni_{81}Fe_{19}$ thin films through the use of rare-earth dopants," IEEE Trans. Magn. **37,** 1749–1754 (2001).

[58] L. Berger, "Emission of spin waves by a magnetic multilayer traversed by a current," Phys. Rev. B **54,** 9353–9358 (1996).

[59] J. C. Slonczewski, "Current-driven excitation of magnetic multilayers," J. Magn. Magn. Mat. **159,** L1–L7 (1996).

[60] F. J. Albert, J. A. Katine, R. A. Buhrman, and D. C. Ralph, "Spin-polarized current switching of a Co thin film nanomagnet," Appl. Phys. Lett. **77,** 3809–3811 (2000).

[61] J. A. Katine, F. J. Albert, R. A. Buhrman, E. B. Myers, and D. C. Ralph, "Current-driven magnetization reversal and spin-wave excitations in Co/Cu/Co pillars," Phys. Rev. Lett. **84,** 3149–3152 (2000).

[62] J. Grollier, V. Cros, A. Hamzic, J. M. George, H. Jaffrès, A. Fert, G. Faini, J. B. Youssef, and H. Legall, "Spin-polarized current induced switching in Co/Cu/Co pillars," Appl. Phys. Lett. **78,** 3663–3665 (2001).

[63] J. Z. Sun, "Spin-current interaction with a monodomain magnetic body: A model study," Phys. Rev. B **62,** 570–578 (2000).

[64] J. Miltat, G. Albuquerque, A. Thiaville, and C. Vouille, "Spin transfer into an inhomogeneous magnetization distribution," J. Appl. Phys. **89,** 6982–6984 (2001).

[65] W. Rave, K. Ramstöck, and A. Hubert, "Corners and nucleation in micromagnetics," J. Magn. Magn. Mat. **183,** 329–333 (1998).

[66] P. Trouilloud and J. Miltat, "Néel lines in ferrimagnetic garnet epilayers with orthorhombic anisotropy and canted magnetization," J. Magn. Magn. Mat. **66,** 99–117 (1987).

[67] M. Labrune and J. Miltat, "Wall structures in ferro/antiferromagnetic exchanged-coupled bilayers: a numerical micromagnetic approach," J. Magn. Magn. Mat. **151,** 231–245 (1995).

[68] J. Eastwood, R. Hockney, and D. Lawrence, Comput. Phys. Commum. **19,** 215 (1980).

[69] R. Hockney and J. Eastwood, *Computer Simulation using Particles* (McGraw-Hill, New York, 1981).

[70] S. W. Yuan and H. N. Bertram, "Fast adaptive algorithms for micromagnetics," IEEE Trans. Magn. **28,** 2031–2035 (1992).

[71] D. V. Berkov, K. Ramstöck, and A. Hubert, "Solving micromagnetic problems: Towards an optimal numerical method," Phys. Status Solidi A **137,** 207 (1993).

[72] W. H. Press, S. A. Teukolsky, W. T. Vetterling, and B. P. Flannery, *Numerical Recipes in FORTRAN: The Art of Scientific Computing* (Cambridge University Press, New York, 1994).

[73] A. E. LaBonte, "Two-dimensional Bloch-type domain walls in ferromagnetic films," J. Appl. Phys. **40,** 2450–2458 (1969).

[74] N. L. Schryer and L. R. Walker, "The motion of 180° domain walls in uniform dc magnetic fields," J. Appl. Phys. **45,** 5406–5421 (1974).

[75] C. C. Shir, "Computations of the micromagnetic dynamics in domain walls," J. Appl. Phys. **49,** 3413–3421 (1978).

[76] Y. Nakatani, Y. Uesaka, and N. Hayashi, "Direct solution of the Landau-Lifshitz-Gilbert equation for micromagnetics," Jpn. J. Appl. Phys. **28,** 2485–2507 (1989).

[77] B. Kevorkian, Ph.D. dissertation, Université Joseph Fourier, 1998.

[78] G. Albuquerque, J. Miltat, and A. Thiaville, "Self-consistency based control scheme for magnetization dynamics," J. Appl. Phys. **89,** 6719–6721 (2001).

[79] G. Albuquerque, J. Miltat, and A. Thiaville, "Coherent spin structures dynamics: Numerics and Application to High Density Magnetic Random Access Memories (MRAM's)," In *16th IMACS World Congress*, M. Deville and R. Owens, eds., (IMACS, New York, 2000), ISBN 3-9522075-1-9.

[80] N. D. Mermin, "The topological theory of defects in ordered media," R. Mod. Phys. **51,** 591–648 (1979).

[81] M. Labrune and J. Miltat, "Strong stripes as a paradigm of quasi-topological hysteresis," J. Appl. Phys. **75,** 2156–2168 (1994).

[82] B. Joe, "GEOMPACK,", http://members.attcanada.ca/ bjoe/index.htm.

[83] G. F. Carey, *Computational Grids: Generation, Adaptation, and Solution Strategies* (Taylor & Francis, Washington, 1997).

[84] S. Pissanetzky, *Sparse Matrix Technology* (Academic Press, New York, 1984).

[85] M. J. Donahue, D. G. Porter, R. D. McMichael, and J. Eicke, "Behavior of μMAG standard problem No. 2 in the small particle limit," J. Appl. Phys. **87,** 5520–5522 (2000).

[86] M. J. Donahue and R. D. McMichael, private communication.